



4

DTIC FILE COPY

DNA-TR-87-27

AD-A190 045

EFFECTS OF IONIZATION-INDUCED SMOG ON AIR CHEMISTRY

V. A. J. van Lint
Mission Research Corporation
5434 Ruffin Road
San Diego, CA 92123-1313

30 January 1987

Technical Report

CONTRACT No. DNA 001-81-C-0151

Approved for public release;
distribution is unlimited.

THIS WORK WAS SPONSORED BY THE DEFENSE NUCLEAR AGENCY
UNDER RDT&E RMSS CODE B326084466 X99QMXVC00004 H2590D.

Prepared for
Director
DEFENSE NUCLEAR AGENCY
Washington, DC 20305-1000

DTIC
ELECTE
FEB 29 1988
S D E

8 2 20 151

Destroy this report when it is no longer needed. Do not return to sender.

PLEASE NOTIFY THE DEFENSE NUCLEAR AGENCY
ATTN: TITL, WASHINGTON, DC 20305 1000, IF YOUR
ADDRESS IS INCORRECT, IF YOU WISH IT DELETED
FROM THE DISTRIBUTION LIST, OR IF THE ADDRESSEE
IS NO LONGER EMPLOYED BY YOUR ORGANIZATION.



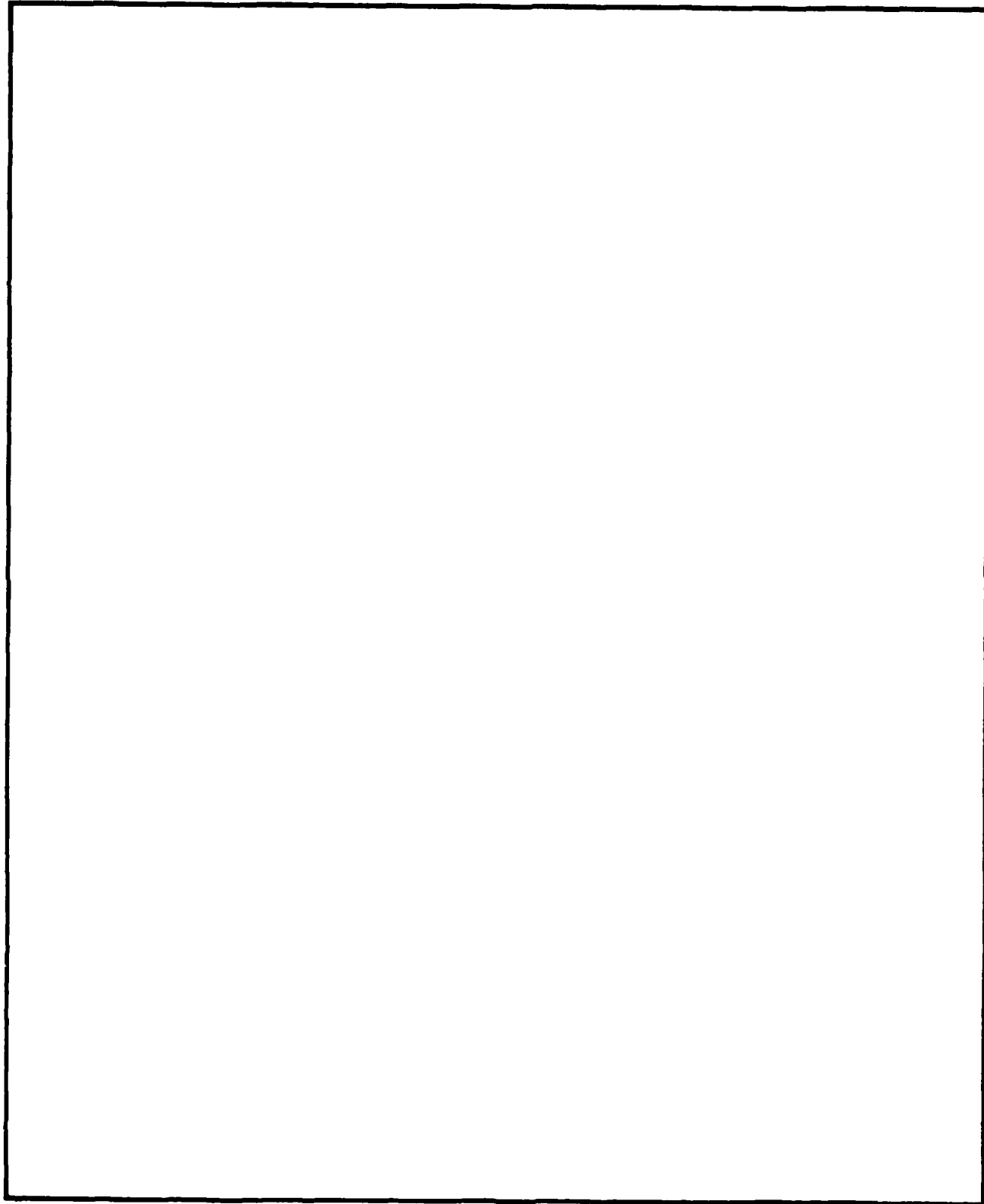
UNCLASSIFIED

SECURITY CLASSIFICATION OF THIS PAGE

REPORT DOCUMENTATION PAGE				
1a. REPORT SECURITY CLASSIFICATION UNCLASSIFIED		1b. RESTRICTIVE MARKINGS		
2a. SECURITY CLASSIFICATION AUTHORITY N/A since Unclassified		3. DISTRIBUTION/AVAILABILITY OF REPORT Approved for public release; distribution is unlimited.		
2b. DECLASSIFICATION/DOWNGRADING SCHEDULE N/A since Unclassified				
4. PERFORMING ORGANIZATION REPORT NUMBER(S) MRC/SD-R-183		5. MONITORING ORGANIZATION REPORT NUMBER(S) DNA-TR-87-27		
6a. NAME OF PERFORMING ORGANIZATION Mission Research Corporation	6b. OFFICE SYMBOL (if applicable)	7a. NAME OF MONITORING ORGANIZATION Director Defense Nuclear Agency		
6c. ADDRESS (City, State, and ZIP Code) 5434 Ruffin Road San Diego, CA 92123-1313		7b. ADDRESS (City, State, and ZIP Code) Washington, DC 20305-1000		
8a. NAME OF FUNDING/SPONSORING ORGANIZATION	8b. OFFICE SYMBOL (if applicable) RAEE/Farmer	9. PROCUREMENT INSTRUMENT IDENTIFICATION NUMBER DNA 001-81-C-0151		
8c. ADDRESS (City, State, and ZIP Code)		10. SOURCE OF FUNDING NUMBERS		
		PROGRAM ELEMENT NO. 62715H	PROJECT NO. X99QMXV	TASK NO. C
				WORK UNIT ACCESSION NO. DH005415
11. TITLE (Include Security Classification) EFFECTS OF IONIZATION-INDUCED SMOG ON AIR CHEMISTRY				
12. PERSONAL AUTHOR(S) van Lint, V. A. J. and Lawrence, J. E.				
13a. TYPE OF REPORT Technical	13b. TIME COVERED FROM 830801 TO 851130	14. DATE OF REPORT (Year, Month, Day) 870130	15. PAGE COUNT 112	
16. SUPPLEMENTARY NOTATION This work was sponsored by the Defense Nuclear Agency under RDT&E RMSS Code B326084466 X99QMXVC00004 H2590D.				
17. COSATI CODES			18. SUBJECT TERMS (Continue on reverse if necessary and identify by block number)	
FIELD	GROUP	SUB-GROUP	Ionization Air Chemistry IR Spectra, <i>Infrared</i> ←	
20	5			
	2			
19. ABSTRACT (Continue on reverse if necessary and identify by block number)				
<p>The effect of ionization doses up to 30 Mrad on air was measured by IR absorption and ionization induced transient conductivity. Short lived IR absorption bands were introduced, but none are directly associated with known stable species. No significant effect on the electron attachment rate was detected.</p> <p><i>(Keywords: -</i></p>				
20. DISTRIBUTION/AVAILABILITY OF ABSTRACT <input type="checkbox"/> UNCLASSIFIED/UNLIMITED <input checked="" type="checkbox"/> SAME AS RPT <input type="checkbox"/> DTIC USERS		21. ABSTRACT SECURITY CLASSIFICATION UNCLASSIFIED		
22a. NAME OF RESPONSIBLE INDIVIDUAL Sandra E. Young		22b. TELEPHONE (include Area Code) 22c. OFFICE SYMBOL (202) 325-7042 DNA/CSTI		

UNCLASSIFIED

SECURITY CLASSIFICATION OF THIS PAGE



SECURITY CLASSIFICATION OF THIS PAGE

UNCLASSIFIED

CONVERSION TABLE

CONVERSION TABLE FOR U.S. CUSTOMARY TO METRIC (SI) UNITS OF MEASUREMENT

MULTIPLY \longleftrightarrow BY \longleftrightarrow TO GET
 TO GET \longleftarrow BY \longleftarrow DIVIDE

angstrom atmosphere (normal) bar barn British thermal unit (thermochemical) calorie (thermochemical) cal (thermochemical)/cm ² curie degree (angle) degree Fahrenheit electron volt erg erg/second foot foot-pound-force gallon (U. S. liquid) inch jerk joule/kilogram (J/kg) (radiation dose absorbed) kilotons kip (1000 lbf) kip/inch ² (ksi) ktap micron mil mile (international) ounce pound-force (lbs avoirdupois) pound-force inch pound-force/inch pound-force/foot ² pound-force/inch ² (psi) pound-mass (lbm avoirdupois) pound-mass-foot ² (moment of inertia) pound-mass/foot ³ rad (radiation dose absorbed) roentgen shake slug torr (mm Hg, 0° C)	1. 000 000 X E -10 1. 013 25 X E +2 1. 000 000 X E +2 1. 000 000 X E -28 1. 054 350 X E +3 4. 184 000 4. 184 000 X E -2 3. 700 000 X E +1 1. 745 329 X E -2 t _x = (t° f + 459. 67)/1. 8 1. 602 19 X E -19 1. 000 000 X E -7 1. 000 000 X E -7 3. 048 000 X E -1 1. 355 818 3. 785 412 X E -3 2. 540 000 X E -2 1. 000 000 X E +9 1. 000 000 4. 183 4. 448 222 X E +3 6. 894 757 X E +3 1. 000 000 X E +2 1. 000 000 X E -6 2. 540 000 X E -5 1. 609 344 X E +3 2. 834 952 X E -2 4. 448 222 1. 129 848 X E -1 1. 751 268 X E +2 4. 788 026 X E -2 6. 894 757 4. 535 924 X E -1 4. 214 011 X E -2 1. 601 846 X E +1 1. 000 000 X E -2 2. 579 760 X E -4 1. 000 000 X E -8 1. 459 390 X E +1 1. 333 22 X E -1	meters (m) kilo pascal (kPa) kilo pascal (kPa) meter ² (m ²) joule (J) joule (J) mega joule/m ² (MJ/m ²) *giga becquerel (GBq) radian (rad) degree kelvin (K) joule (J) joule (J) watt (W) meter (m) joule (J) meter ³ (m ³) meter (m) joule (J) Gray (Gy) terajoules newton (N) kilo pascal (kPa) newton-second/m ² (N-s/m ²) meter (m) meter (m) meter (m) kilogram (kg) newton (N) newton-meter (N·m) newton/meter (N/m) kilo pascal (kPa) kilo pascal (kPa) kilogram (kg) kilogram-meter ² (kg·m ²) kilogram/meter ³ (kg/m ³) **Gray (Gy) coulomb/kilogram (C/kg) second (s) kilogram (kg) kilo pascal (kPa)
---	---	---

*The becquerel (Bq) is the SI unit of radioactivity; 1 Bq = 1 event/s.
 **The Gray (Gy) is the SI unit of absorbed radiation.

TABLE OF CONTENTS

Section		Page
	CONVERSION TABLE	iii
	LIST OF ILLUSTRATIONS	v
	LIST OF TABLES	vii
1	INTRODUCTION	1
2	EXPERIMENTAL SETUP	6
	2.1 OPTICAL DESIGN	6
	2.2 ELECTRICAL DESIGN	9
3	THEORY OF μ/α MEASUREMENTS	12
	3.1 BOUNDARY LAYERS	13
4	CORRECTIONS OF DETECTOR DATA	15
	4.1 SHORT TERM DRIFT CORRECTIONS	15
	4.2 LONG TERM DRIFT CORRECTIONS	20
5	DOSIMETRY	21
6	CALIBRATION SPECTRA	31
7	EFFECT OF RADIATION ON IR ABSORPTION SPECTRA	45
	7.1 DRY AIR SPECTRA	45
	7.2 WET AIR SPECTRA	53
8	μ/α DATA	69
9	CONCLUSIONS	90
10	LIST OF REFERENCES	91
APPENDIX		
	CORRECTIONS FOR SCATTERING AND ELECTRON BEAM DIVERGENCE	93

LIST OF ILLUSTRATIONS

Figure		Page
1	Optical setup.	7
2	Setup used to record optical data.	8
3	Calorimeter/Faraday cup circuits.	10
4	Electrical circuit used to measure μ/α .	11
5	Krytron high voltage pulse circuit.	11
6(a)	Bolometer/detector corrector factor for $\lambda = 4$ microns.	16
6(b)	Bolometer/detector corrector factor for $\lambda = 6$ microns.	17
6(c)	Bolometer/detector corrector factor for $\lambda = 8$ microns.	18
6(d)	Final correction factor as a function of wavelength.	19
7	Typical voltage curves of thick (lower) and thin (upper) calorimeters.	22
8	Monitor circuit.	24
9	Faraday cup equivalent circuit.	25
10	Calorimeter equivalent circuit.	25
11	Comparison of spectra of "vacuum" and dry air at one atmosphere pressure.	32
12	High resolution spectrum of water.	33
13	Comparison of spectra of dry and moist air.	34
14	Comparison of spectra of dry air and nitrogen dioxide with dry air added to one atmosphere.	37
15	High resolution spectrum of nitrogen dioxide.	38
16	Comparison of spectra of moist air to that of NO_2 and moist air.	39
17	Comparison of spectrum of moist air to that of HNO_3 and moist air.	40
18	Comparison of spectrum of H_2O to that of $\text{HNO}_3/\text{H}_2\text{O}$ at the same pressure.	41
19	High resolution spectra of nitric acid (HNO_3) lines in our range.	42
20	Comparison of spectra of clean and irradiated dry air.	47
21	"Dry" air spectra.	48
22	Transient absorption near $5.7 \mu\text{m}$.	49
23	Cumulative absorption at $5.7 \mu\text{m}$.	50
24	Recovery at $5.7 \mu\text{m}$.	52
25	Transient absorption near $6.2 \mu\text{m}$.	54
26	Transient fluorescence near $7.5 \mu\text{m}$.	55
27	Effect of irradiation on wet air.	56
28	Effect of rapid irradiation on wet air.	57
29	Recovery of absorption in wet air.	58
30	Effects of rapid irradiation on irradiated wet air.	60
31	Transient absorption near $6.2 \mu\text{m}$.	61
32	Recovery at $6.15 \mu\text{m}$.	62
33	Transient absorption near $5.7 \mu\text{m}$.	63

LIST OF ILLUSTRATIONS (Concluded)

Figure		Page
34	Relaxation at 6.05 μm .	64
35	Transient absorption and recovery near 6.2 μm .	65
36	Effect of 10 K Ω resistor on grid.	69
37	Grid voltage. Faraday cup voltage and ion chamber current for shot 210.	71
38	Grid voltage. Faraday cup voltage and ion chamber current for shot 214.	72
39	Grid voltage. Faraday cup voltage and ion chamber current for shot 199.	73
40	Grid voltage. Faraday cup voltage and ion chamber current for shot 207.	75
41	Grid voltage. Faraday cup voltage and ion chamber current for shot 215.	78
42	Grid voltage. Faraday cup voltage and ion chamber current for shot 219.	79
43	Grid voltage. Faraday cup voltage and ion chamber current for shot 221.	81
44	Grid voltage. Faraday cup voltage and ion chamber current for shot 222.	82
45	Grid voltage. Faraday cup voltage and ion chamber current for shot 223.	83
46	Grid voltage. Faraday cup voltage and ion chamber current for shot 225.	84
47	Grid voltage. Faraday cup voltage and ion chamber current for shot 227.	85
48	Grid voltage. Faraday cup voltage and ion chamber current for shot 228.	86
49	Grid voltage. Faraday cup voltage and ion chamber current for shot 229.	87
50	Grid voltage. Faraday cup voltage and ion chamber current for shot 230.	88
51	Grid voltage. Faraday cup voltage and ion chamber current for shot 232.	89
52	Effect of pressure (lower trace = Faraday cup).	94

LIST OF TABLES

Table		Page
1	Conductivity in unirradiated wet air ($\approx 2.2\% \text{H}_2\text{O}$).	74
2	μ/α in irradiated wet air ($\approx 2.2\% \text{H}_2\text{O}$).	74
3	μ/α in dry air.	77
4	Effect of contaminants on μ/α .	80

Accession For	
NTIS GRA&I	<input checked="" type="checkbox"/>
DTIC TAB	<input type="checkbox"/>
Unannounced	<input type="checkbox"/>
Justification	
By _____	
Distribution/	
Availability Codes	
Dist	Avail and/or Special
A-1	



SECTION 1 INTRODUCTION

The maximum electric field produced near a nuclear explosion in air is determined by the balance between outward moving Compton electrons and the return current through the conducting air. The air conductivity, in turn, is determined by the ionization rate, which is proportional to the Compton electron current density, and the mobility of the electrons divided by the rate at which they are immobilized, principally by attachment to neutral molecules. It has been suggested (Ref. 1) that at sufficiently high accumulated radiation dose the effective electron attachment rate may be increased over the value in unirradiated air by the contribution from new chemical species formed in the air by processes resulting from ionization, particularly nitric acid.

At first it was thought that nuclear lightning could be explained by such an effect. Subsequent experimental (Ref. 2) and analytical work established that the effect was too small to explain nuclear lightning, considering the radiation dose that was deposited at the distances where lightning strokes were observed. Subsequent theoretical work also established that an anomalously large electric field was not necessary to explain nuclear lightning, since considering the presence of a volume source of Compton current and a volume conductivity allowed a lightning-like channel to grow at much smaller ambient electric fields required for lightning in nonconducting air (Ref. 3,4).

Subsequently, there has been increasing interest in the Source Region Electromagnetic Pulse (SREMP) fields produced very close to a high-yield nuclear explosion. This concern results from the possibility of ultra-hard missile silos surviving very close to an explosion, and the recognition that the excitation of long conductors between an explosion and a nearby silo depends on the integral of the electric field between the fireball and the silo. Therefore, an experiment was proposed to measure the effect of doses up to 30 Mrad on the attachment rate of electrons in air. This initial design of the experiment was similar to the HERMES experiment (Ref. 2), except that the AURORA electron beam was to be used to produce the larger initial dose over a reasonable area. Subsequently, it was noted by M. Schiebe and F. Gilmore that the formation of nitric acid by a short pulse, as produced by AURORA, would be significantly less than by a typical weapon gamma pulse, in which significant doses are delivered for times up to 100 μ s. Therefore, other means of producing the required dose over a longer time scale were investigated.

A promising ionization source was the WIP gun, developed by Dr. G. Wakalopoulos. It appeared to be capable of producing the required dose rate and pulse length, although it had actually been tested only up to 5 μ s pulses. After lengthy negotiations it was decided that the risk of damaging the source and the costs were too large to pursue that approach further.

Finally, it was established that an experiment in which the dose was delivered not in a single 100 μ s pulse but in a number of shorter pulses spaced 30 s apart would be acceptable. The reason the AURORA pulse was not acceptable was that the eventual attaching species (e.g., HNO_3) were the product of sequential interactions with species formed by ionization. Therefore, there had to be sufficient time between ionization events for the intermediate species to be formed before the next step in the reaction sequence could occur. It was established that the candidate intermediate

species were chemically stable, so that they were expected to remain during the 30 s waiting period during exposures. Scheibe (Ref. 5) mentioned that his only concern was the possibility of these species reacting on the walls of the sample chamber during the waiting period, but it was decided that this risk was less serious than the alternatives, especially if infra-red diagnostics were included in the experiment to monitor the concentrations of these species between ionization pulses.

This historical development led to the experiment that was finally performed at the Maxwell Labs Excitron electron beam source. The specifications for this source included the capability to produce 10 μ s pulses of 300 keV electrons at 1 A/cm², with a pulse repetition rate of two pulses per minute. These performance parameters would enable us to deliver approximately 30 Mrad of total ionization dose in five minutes, by delivering 10 pulses each 10 μ s long and each with a dose of 3 Mrad.

HNO₃ is formed near an EMP source region from the association of NO₂ with OH, where the nitrogen atoms to form NO₂ and the OH radicals are produced by the ionization energy deposition. The attachment reaction is then:



It is believed that a concentration of HNO₃ of at least 2×10^{15} cm⁻³ is necessary for this reaction to compete with that of electron attachment to O₂ (Ref. 1).

The conductivity, σ , of a gas exposed to a radiation pulse is given by

$$\sigma = n e_0 \mu \tag{1}$$

where n is the secondary electron density, and the electron mobility, μ , is a function of the electric field.

At low dose rate, \dot{D} ,

$$n = \frac{K_g \dot{D}}{\alpha} \quad (2)$$

where K_g is the generation constant in air and α is the electron attachment rate. Thus,

$$\sigma = \frac{K_g \dot{D} e_0 \mu}{\alpha} \quad (3)$$

The saturation electric field, E_s , near a nuclear explosion is that field for which the outward moving Compton electron flow is balanced by an equal conduction current. Namely,

$$J_C = K_\sigma \dot{D} = \sigma E_s \quad (4)$$

where J_C is the Compton current density, K_σ is the ratio of Compton current density to dose rate. Combining,

$$E_s = \frac{K_\sigma}{e_0 K_g} \left(\frac{\alpha}{\mu} \right) \quad (5)$$

Thus, the saturation electric field is proportional to α . If α is increased by attaching electrons to NO_2 as well as to O_2 , the electric field increases proportionately.

This experiment is designed to (1) determine the concentration of important smog species (NO_2 , HNO_3) produced from exposure to a dose (D) in the range of $500 \text{ krad} < D < 30 \text{ Mrad}$ and (2) determine the effect of these species on the electron μ/α .

SECTION 2 EXPERIMENTAL SETUP

The experiment consisted of an optical portion which was constructed to determine the presence and concentration of a species by their infra-red absorption spectra, and an electrical portion designed to measure dose rate and electron μ/α .

2.1 OPTICAL DESIGN.

The basic setup for the optical component of the experiment is shown in Figure 1. The IR source (glow bar - Oriel Model 6363, 11 A @ 12 V) was fed by an ORIEL DC regulated power supply (Model 68735). The intensity of infrared light produced was measured by a thermopile detector (ORIEL Model 7102), hereafter referred to as the bolometer. Light from the source was directed into the chamber after passing through a reference chopper beam (HMS Light Beam Chopper 220). After being chopped, the beam entered the chamber and was reflected four full lengths of it - with a total optical path length of 400 cm. The light was then directed through the entrance slit at (A) of a monochromator (Jarrell-Ash Monospec 18 - Model 82477). A collimating mirror at (B) directed the beam to a diffraction grating at (C) (ruling = 1008/mm, dispersion = 54 nm/mm). Light was then directed to a refocusing mirror at (D) and was reflected to the exit slit at (E). The position of the grating - which determined the wavelength - was controlled by a stepper motor (ORIEL Model 18510). After leaving the monochromator, the beam was incident on the window of a HgCdTe Detector (Infrared Assoc., Inc.), hereafter referred to as the detector. Dry air was blown through a plastic bag sealed around the bolometer, source, monochromator and detector

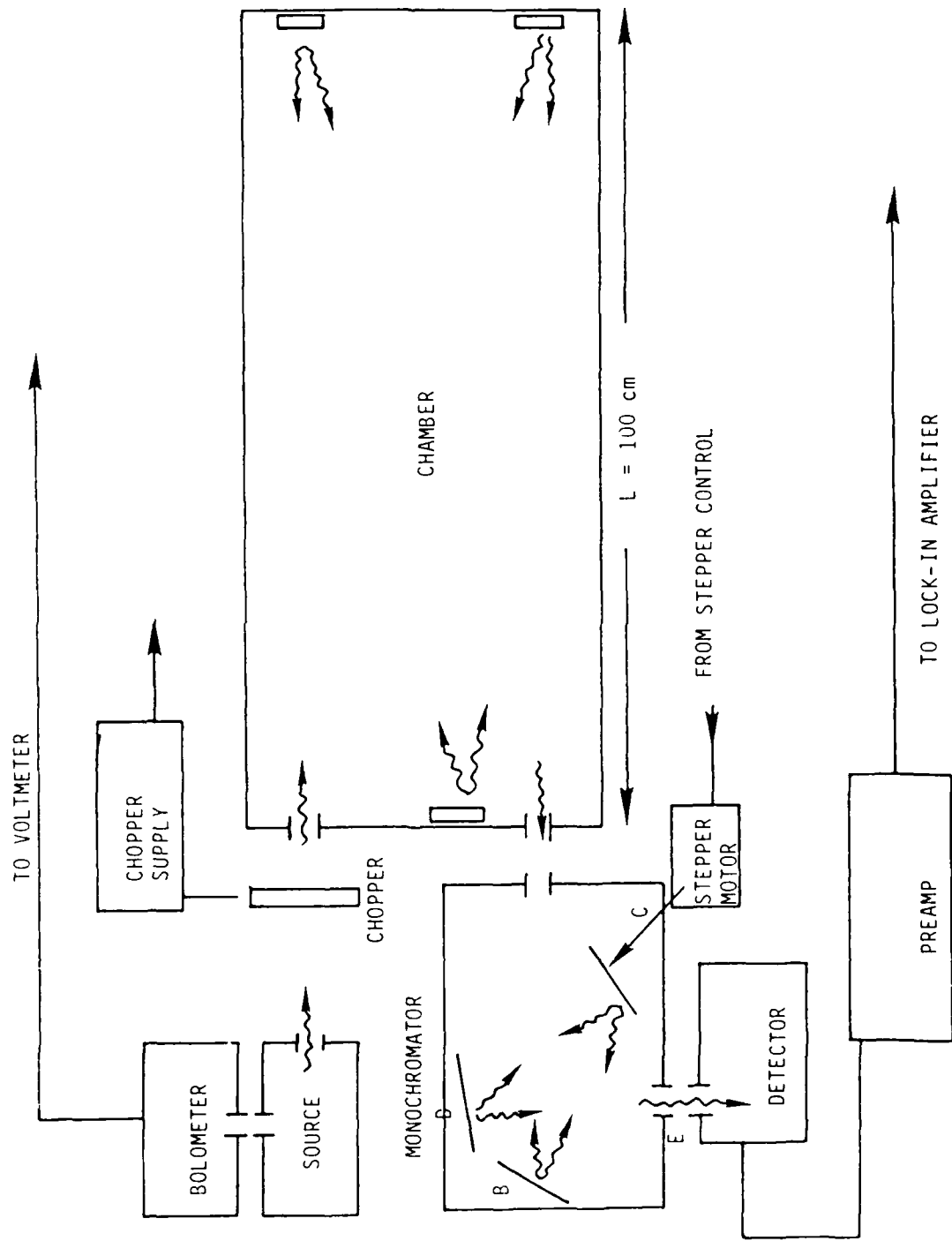


Figure 1. Optical setup.

to reduce absorption caused by moisture in the air external to the chamber. This had the desired effect in that the water absorption bands seen when the chamber was evacuated were greatly reduced in intensity.

The instruments used to record and process measurements from the bolometer and detector and to control the stepper motor were located outside of the exposure room so as to reduce noise signals caused by the Excitron pulses. The basic hookup of these instruments is as shown in Figure 2.

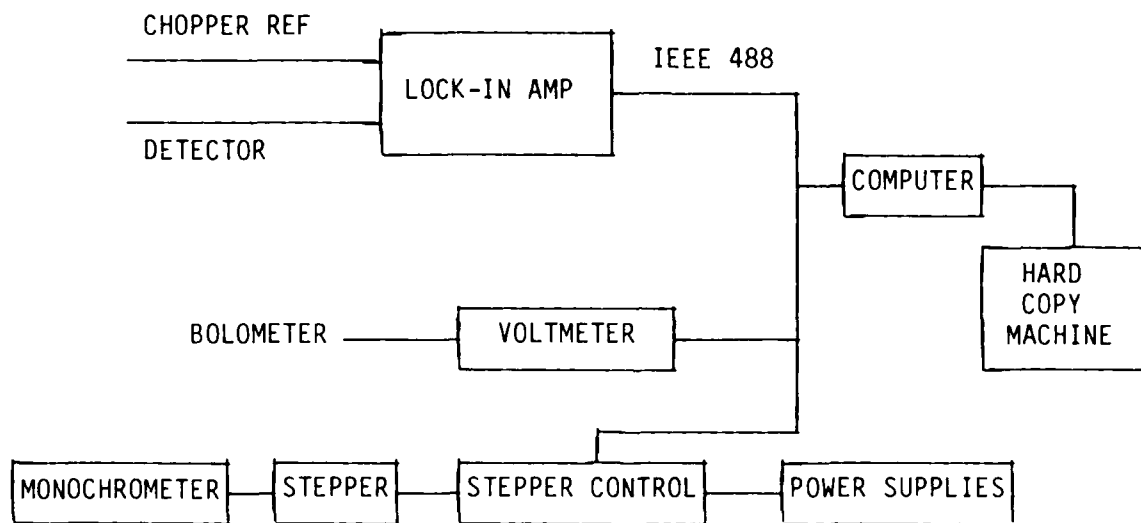


Figure 2. Setup used to record optical data.

The detector and the chopper reference were connected to the lock-in amplifier (EG&G Model 5316) which was hooked to the computer (Tektronix 4051). The bolometer was connected to the voltmeter (Hewlett Packard Model 3455A), which was also hooked up to the computer. The program for this experiment was designed to (1) control stepper position, (i.e., wavelength at which data was recorded), (2) process data received from bolometer and detector; (3) plot spectra resulting from scanning various wavelengths; (4) print data from separate readings at one or a few selected wavelengths. The hard copy machine (Tektronix Model 4631) gave a printed copy of these data.

2.2 ELECTRICAL DESIGN.

Four copper calorimeters were located inside the chamber and were used to measure the dose received from the Excitron. Two were 35 mil thick and two were 1 mil thick. The rear (thick) calorimeter had diameter of 0.6 cm ($A = 0.28 \text{ cm}^2$). The front calorimeter all had a diameter = 0.8 cm. Both thin calorimeters (and one of the thick) were located in front of the chamber. The remaining (thick) calorimeter was located in the rear of the chamber so that the incident electrons passed through the gas in the chamber before reaching it. The circuits for the calorimeters are as shown in Figure 3.

The calorimeters converted the temperature change - caused by the energy loss of the electrons in passing through them - to a voltage reading by means of Chromel alumel thermocouples (sensitivity $40 \mu\text{V}/^\circ\text{C}$). The Faraday cup readings were taken from a branch of the thick calorimeter circuits, as shown, and measured the current from the electron beam as a voltage across the effective resistance seen by that branch of the circuit. The Faraday cup measurements were recorded by oscilloscopes (Tektronix 7844) located in a screen box in the adjoining room. The calorimeter voltages were amplified by an OpAmp circuit and recorded on a chart recorder (Houston, Model B5217-5) also in the adjoining room.

The setup used to measure the electron (μ/α) was located inside the ion chamber and is shown in Figure 4.

The central cathode foil, C, was biased negatively by the Krytron high voltage pulse circuit shown in Figure 5. Ionized gas molecules were attracted to the cathode, while the low energy electrons were attracted to ground at P. Since the ion mobility is small compared to the electron mobility, the ion chamber current readings were proportional to the electron current, J_e . The grids (G) were positioned such that the boundary layer formed near the cathode, C, did not affect the region between the grid and

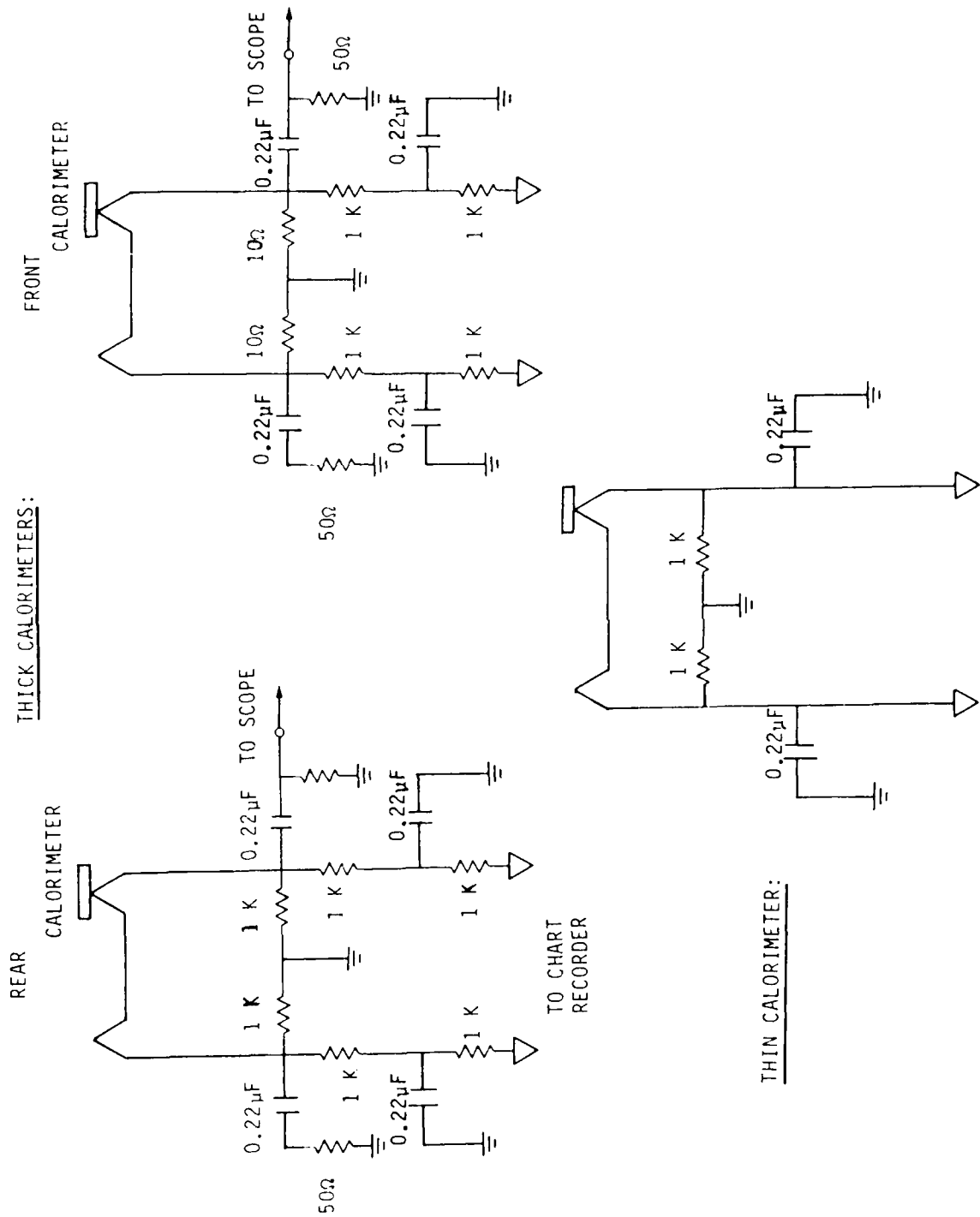


Figure 3. Calorimeter/Faraday Cup circuits.

anode, P. Thus, the grid voltage measured the uniform field, E, between grid and ground.

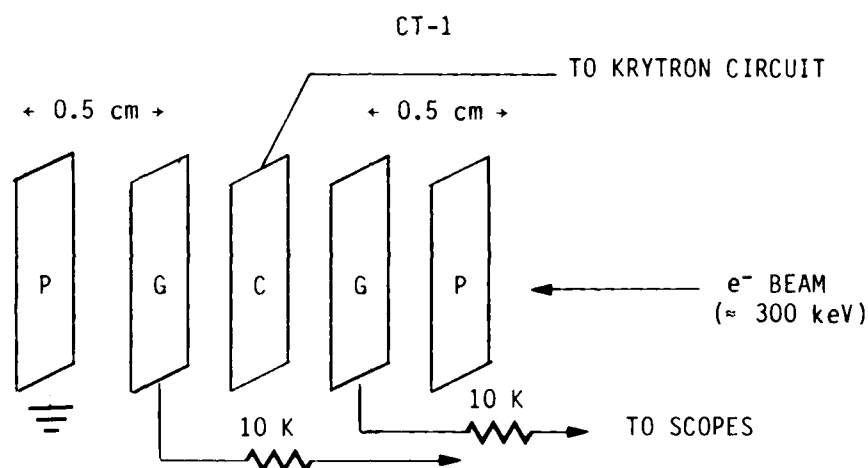


Figure 4. Electrical circuit used to measure μ/α .

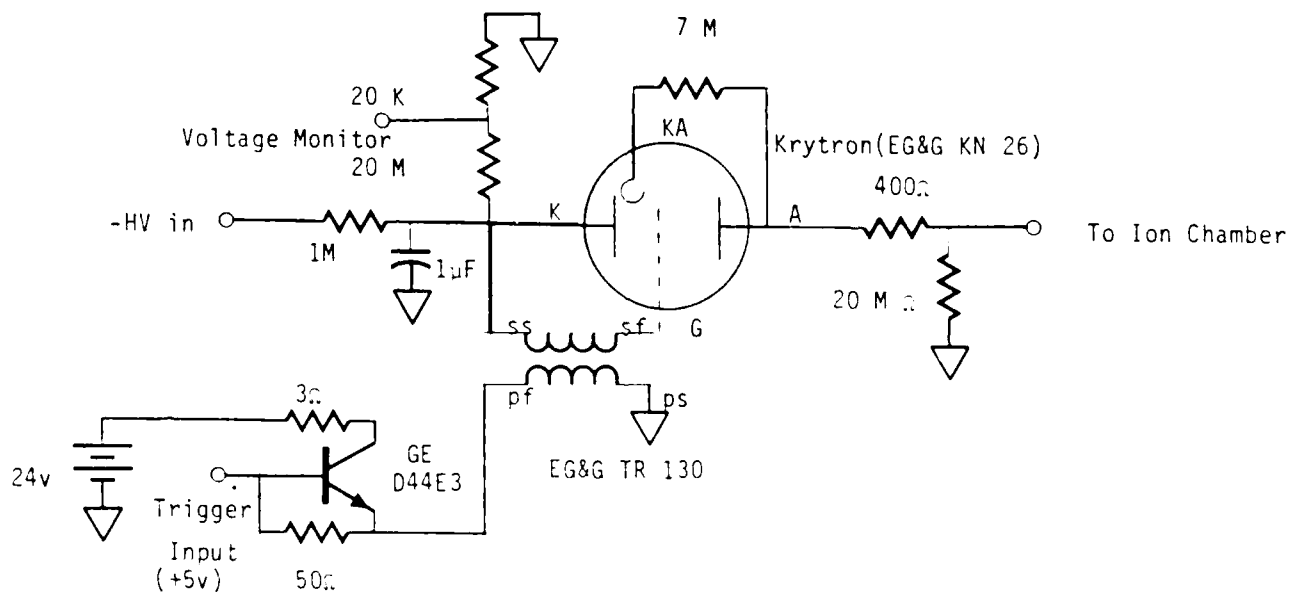


Figure 5. Krytron high voltage pulse circuit.

SECTION 3
THEORY OF μ/α MEASUREMENTS

The current density in the ion chamber, J_e , is given by

$$J_e = \sigma E \quad (6)$$

The conductivity, when the motion of the ions are neglected, is given by:

$$\sigma = ne_0\mu \quad (7)$$

where n is the free electron density and μ is the electron mobility. At low dose rate, \dot{D} , the density of free electrons is determined by the attachment rate, α . In steady state,

$$n = \frac{K_g \dot{D}}{\alpha} \quad (8)$$

where $K_g = 2.2 \times 10^9 \text{ cm}^{-3}/\text{rad}$ is the ionization constant in air and depends weakly on the gas composition. The ratio μ/α is then

$$\frac{\mu}{\alpha} = \frac{J_e}{e_0 K_g E_s \dot{D}} \quad (9)$$

where J_e is proportional to the ion chamber current
 E_s is proportional to the grid voltage
 \dot{D} is proportional to the rear Faraday cup current.

3.1 BOUNDARY LAYERS.

Boundary layers are formed near the cathode by electrons and negative ions moving toward the anode and near the anode by positive ions. The cathode boundary layer is so strong that an avalanche field is created to replenish the electrons. The voltage across the boundary layer is ignored by using the grid to measure the field between grid and grounded anode.

The excess potential drop at the anode due to the positive ion boundary layer is given by

$$\Delta V = \frac{1}{2} \frac{\rho}{\epsilon_0} w^2 \quad (10)$$

where ρ is the charge density in the boundary layer and w is the thickness of the layer. This thickness, w , depends on the mobility, μ , of the ions and the electron ion recombination rate, R_e , which determines the lifetime, τ , of the ions. Only the ions created within the boundary layer contribute to the excess voltage drop at the anode. The thickness is determined by

$$w = E \mu \tau \quad (11)$$

where E is the electric field applied to the plate

μ is the mobility of the ions

τ is the mean lifetime of the ions

In this experiment, the maximum applied electric field was <2000 V/cm. The positive ion mobility is typically $\mu = 3 \text{ cm}^2/\text{V}\cdot\text{s}$ (Ref. 6). The density, N_+ , of the ions depends on the dose rate, \dot{D} , the electron-ion recombination coefficient, β_e , and the generation constant K_g as

$$N_+ = \sqrt{\frac{K_g \dot{D}}{\beta_e}} \quad (12)$$

The maximum dose received by the gas in one shot was ≈ 3 Mrad. The value of β_e increases during a pulse, but reaches a plateau of $1 \times 10^{-6} \text{ cm}^3/\text{s}$ for moist air at high electric fields (Ref. 7). The effective lifetime of the ions is

$$\tau_i = \frac{N_+}{K_g \dot{D}} \left(K_g \dot{D} \beta_e \right)^{-1/2} = 70 \text{ ns} \quad (13)$$

at a maximum dose rate of $\dot{D} = 10^{11} \text{ rad/s}$. At this dose rate $N_+ = 1.4 \times 10^{13} \text{ ions/cm}^3$. The maximum thickness of the boundary layer is then

$$w = \mu_+ E \tau_i = 4 \times 10^{-4} \text{ cm} \quad (14)$$

Using the above values of N_+ and w yield an excess potential drop due to the anode boundary layer of

$$\begin{aligned} \Delta V &= \frac{1}{2} \frac{e_0 N_+}{\epsilon_0} w^2 \quad (15) \\ &= 3 \text{ V} \end{aligned}$$

This is negligible compared to the applied voltages, which were $> 500 \text{ V}$. Therefore, boundary layers were of no concern in the ion chamber measurements.

SECTION 4 CORRECTIONS OF DETECTOR DATA

4.1 SHORT TERM DRIFT CORRECTIONS.

If the detector readings, V , varied directly with bolometer readings, B , for changes in source intensity, then the bolometer readings could simply be divided out to obtain the true absorption data. Data was recorded at $\lambda = 4, 6, 8 \mu\text{m}$ to determine the manner in which the detector data varied with these changes in source intensity. It was found that for a given wavelength, this relationship between detector and source was not linear, i.e., the ratio (V/B) did not hold constant, at a given wavelength. As a first correction, $\ln(V/V_0)$ vs. $\ln(B/B_0)$ was plotted in order to determine a $\nu(\lambda)$ such that $V^* = V (B_0/B)^{\nu(\lambda)}$ (where V^* is the corrected detector reading). In this way, if $V(t)$ varied directly with $B(t)$ then $V = 1$ and V/B is constant. If $V(t)$ was not proportional to $B(t)$, then any power law type of dependence would be apparent from the slope of the graph of $\ln(V/V_0)$ vs. $\ln(B/B_0)$ for each wavelength. Figure 6 illustrates the results. The value of ν attained in this manner was not the same for the three wavelengths ($\lambda = 4, 6, 8$ microns). Graphing the value of ν vs. $1/\lambda$ for each wavelength yielded the dependence of this exponent on the wavelength. Best results were obtained by plotting ν vs. $1/\lambda$, since a straight line could easily be fitted to these data points. It was found that, to a good approximation,

$$\nu(\lambda) \propto \frac{1}{\lambda}, \quad \text{i.e., } \nu(\lambda) = \frac{1}{0.062\lambda + 0.38} \quad (16)$$

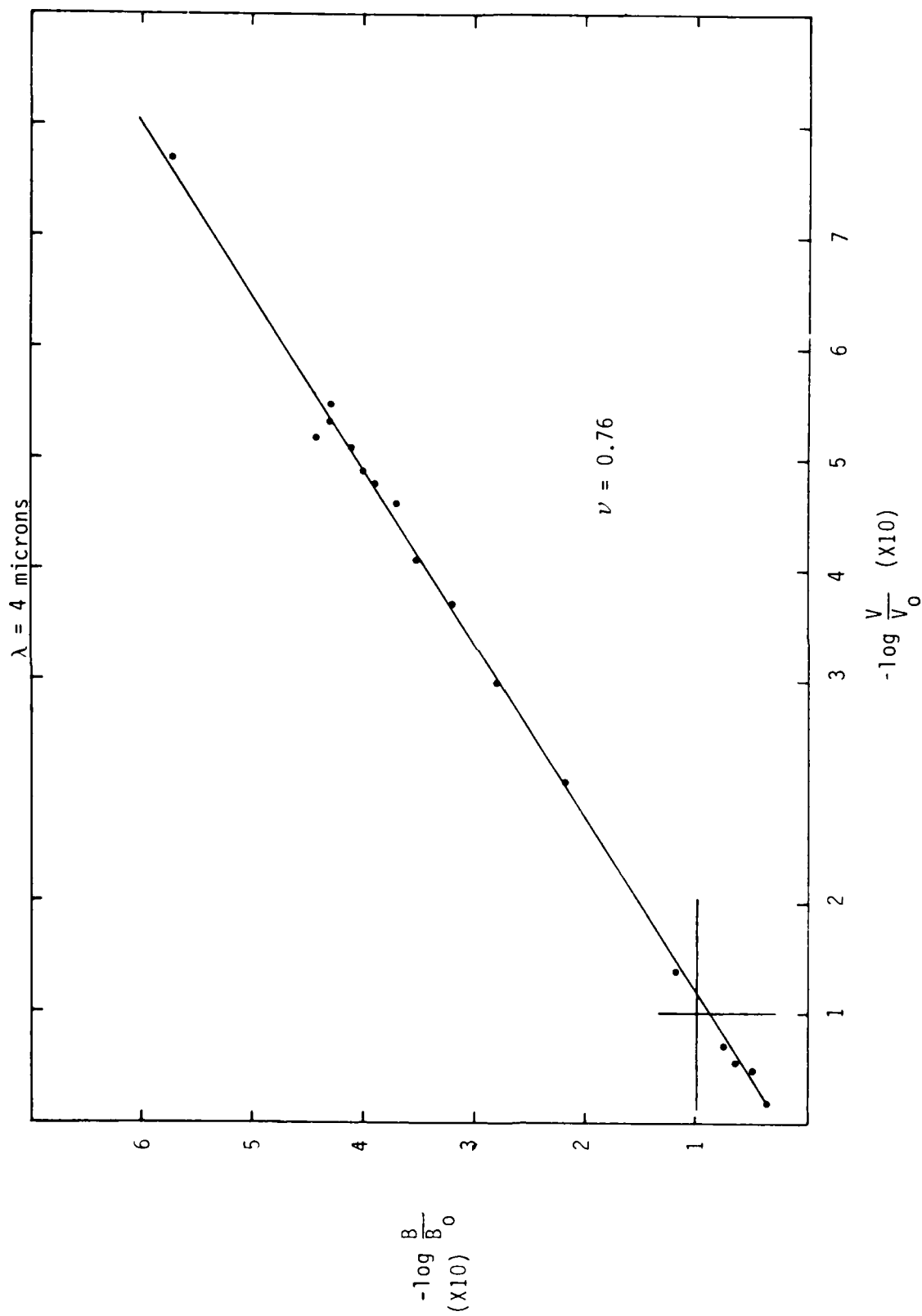


Figure 6(a). Bolometer/detector correction factor for $\lambda = 4$ microns.

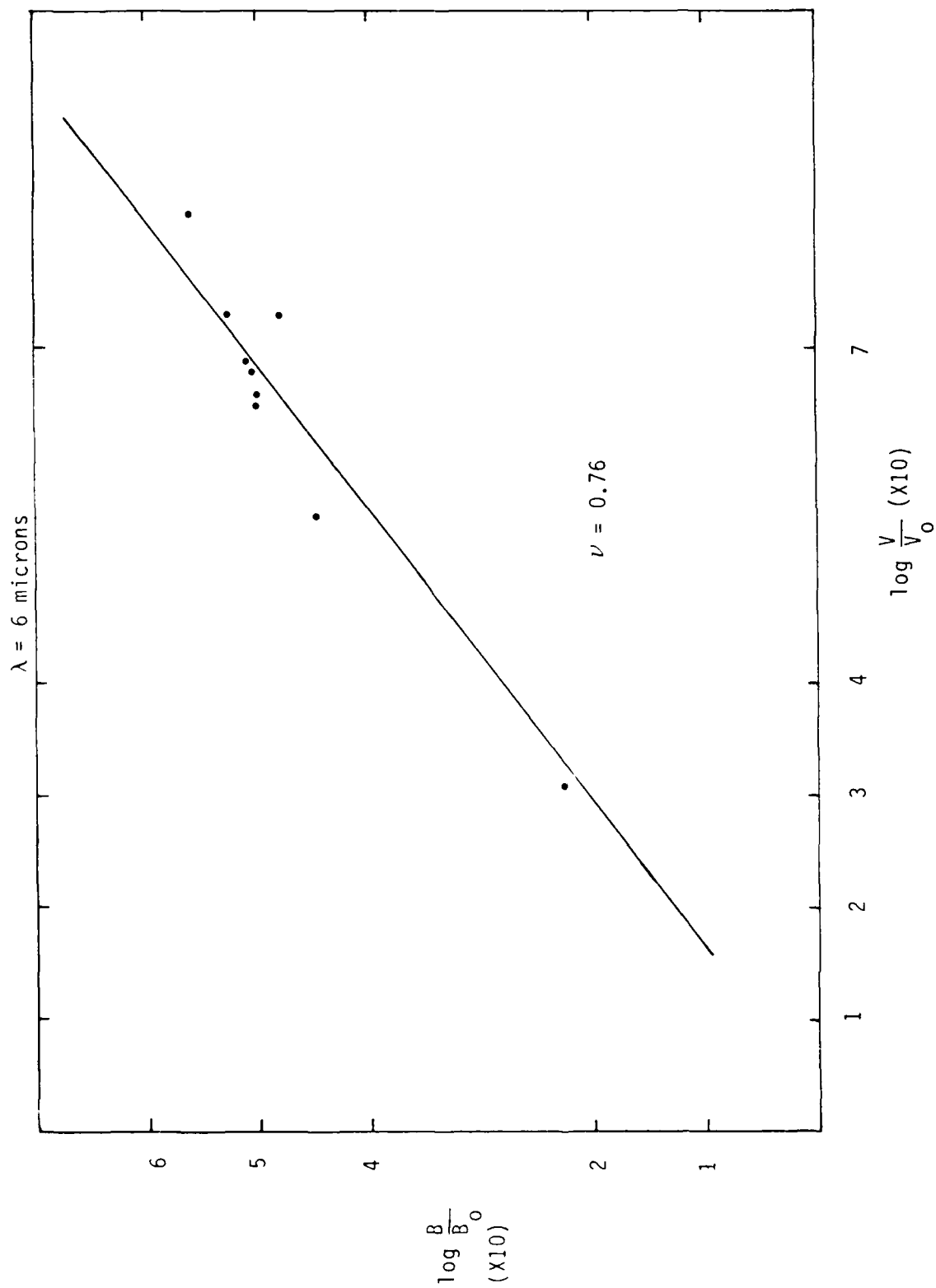


Figure 6(b). Bolometer/detector correction factor for $\lambda = 6 \text{ microns}$.

$\lambda = 8$ microns

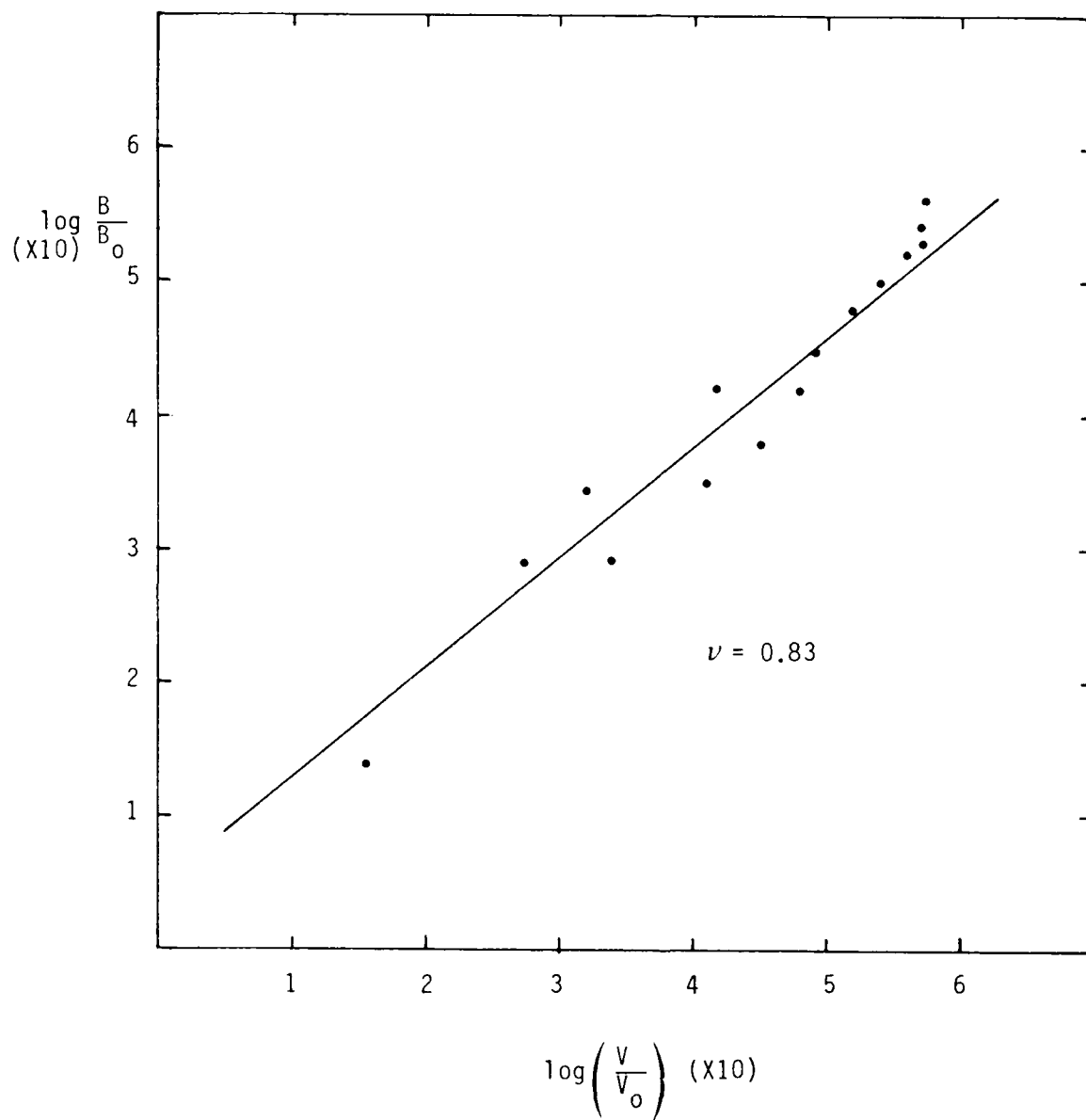


Figure 6(c). Bolometer/detector correction factor for $\lambda = 8$ microns.

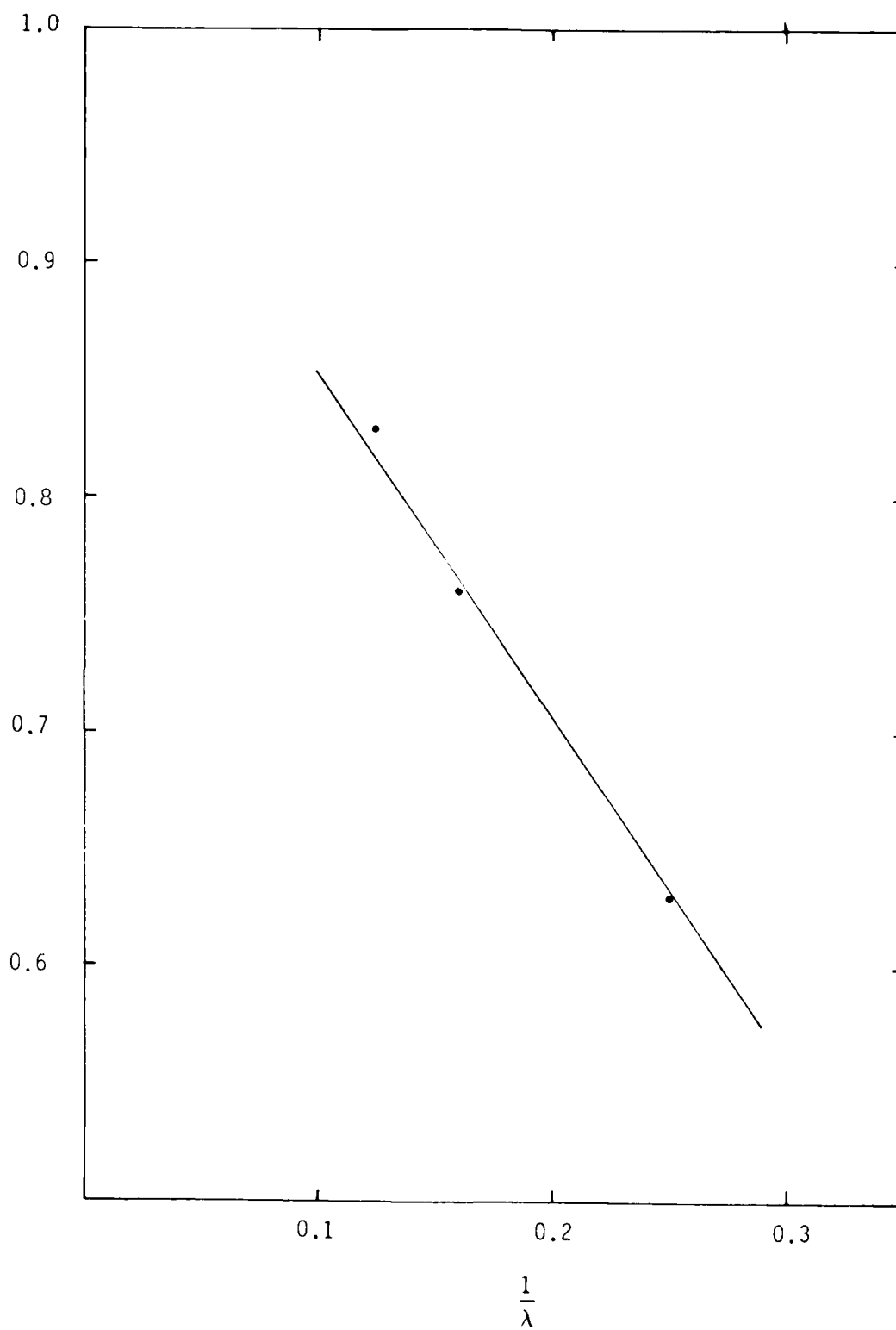


Figure 6(d). Final correction factor as a function of wavelength.

Further, the bolometer was sluggish compared to the detector response and, as a second correction factor, a θ was determined such that $V_C = V^* (1 - \nu(\lambda)\theta \dot{B}/B)$. If B did not vary with time, the corrected $V_C = V^*$ was obtained from the first correction factor. If B decreased suddenly with time over a given interval, $\dot{B} < 0$ and $V_C > V^*$, which is reasonable since the detector reading will drop faster than the bolometer. Similarly for $\dot{B} > 0$. The factor $\nu(\lambda)$ was included to account for any dependence of this correction on wavelength. Although the values of θ obtained were variable, $\theta \approx 2s$ seemed to work well, and this was used in the second correction factor.

4.2 LONG TERM DRIFT CORRECTIONS.

The short term drift corrections applied to data recorded during the course of a single spectrum. For long term drifts in source intensity it was necessary to normalize the data in order to appropriately compare two distinct spectra. This was done - after the short term drift corrections were applied to the individual spectra - by normalizing both spectra to the data recorded at a single wavelength in one of them. The wavelength chosen for normalization was one in which no absorption occurred in either spectrum.

SECTION 5 DOSIMETRY

Incident electrons (≈ 300 keV) transferred energy to the calorimeters by Coulomb collisions with copper atoms in the foil. Thermocouples located behind the foil then converted this temperature change to a voltage reading ($1^\circ\text{C}/40 \mu\text{V}$). The thick calorimeters stopped the electrons, measuring the total energy fluence in the beam. However, the energy had to diffuse across the finite (35 mil) thickness of the foil before reaching the thermocouples. In the meantime, the foil also began to cool off so that the energy distribution in the calorimeter was not uniform. This was apparent in the voltage curves of the thick calorimeters as shown in the lower trace of Figure 7. The true voltage readings were obtained by extrapolating the curves back to the time corresponding to the beginning of the shot, as shown in Figure 7. The upper trace in Figure 7 is the voltage reading of a thin calorimeter corresponding to the same shot. These were much thinner than the range of the electrons and the resulting voltage readings were sharp spikes, as shown. However, the low heat capacity of the thin calorimeter produced a rapid temperature decay. The prompt temperature rise in the thin calorimeters was used for a direct measure of the dose in copper.

The front Faraday cup measurements were taken from a branch of the thick-calorimeter circuit as previously described. These voltage readings measured the current from the electron beam across the effective resistance of the circuit. The average electron number flux density, θ_n , in the thick calorimeter is measured by the voltage reading of the Faraday cup (V_F), the pulse width (t) in μs , the effective resistance, R_{eff} , and the area of the calorimeter A , according to the following equation,

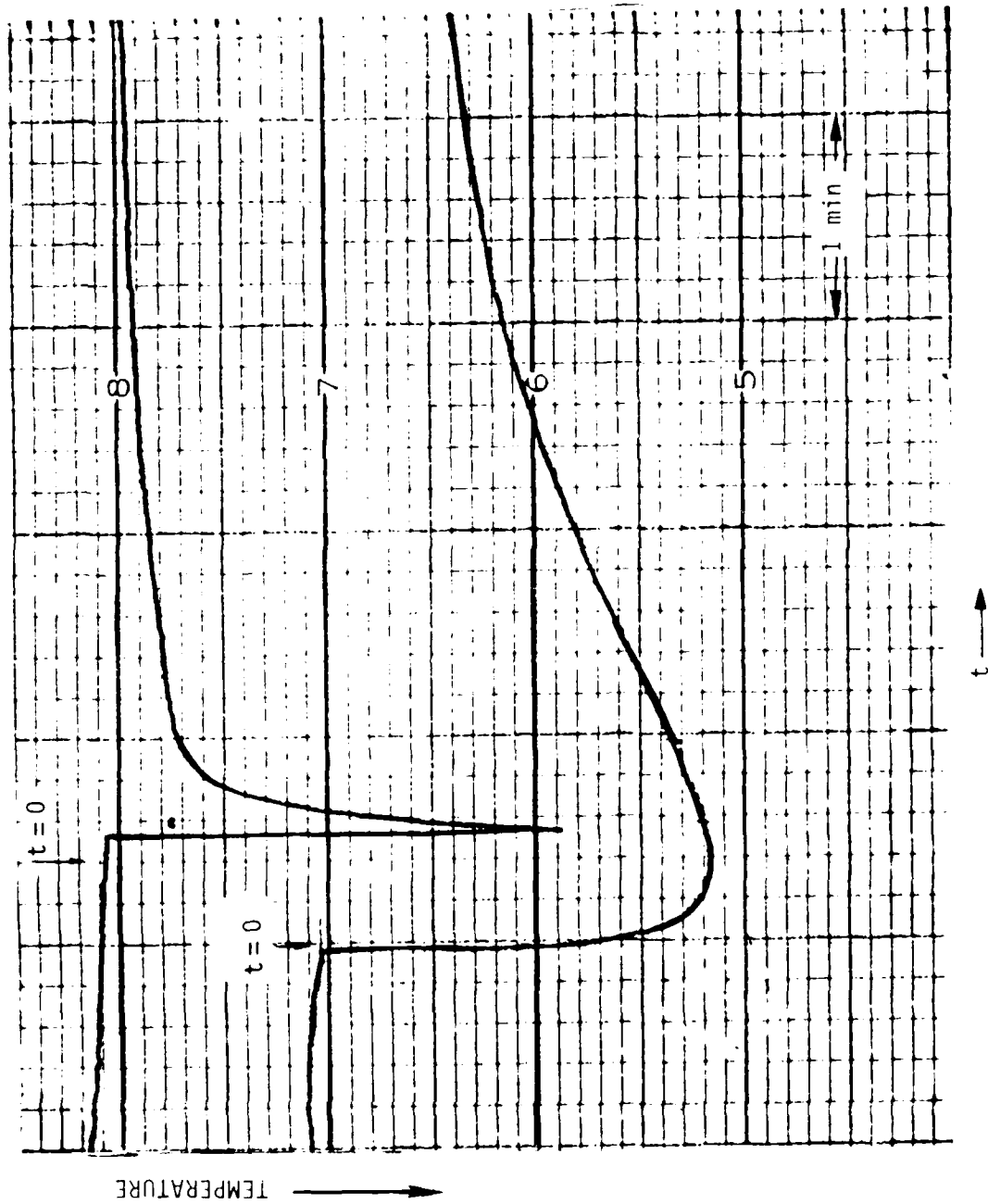


Figure 7. Typical voltage curves of thick (lower) and thin (upper) calorimeters.
 (trace enhanced)
 Thick calorimeter: $50 \mu\text{V}$ - vertical.
 Thin calorimeter: $500 \mu\text{V}$ - vertical.

$$\theta_n(\text{electrons/cm}^2) = \frac{V_F \times t}{R_{\text{eff}} \times A \times e_0} (1 + S) \quad (17)$$

where S is the secondary electron emission coefficient. For ≈ 250 keV electrons, $S \approx 0.2$.

The actual circuit, including measured resistances in the thermocouple wires, is shown in Figure 8. The equivalent circuit for the Faraday cup (fast) measurements is shown in Figure 9. The effective resistance, V_s/I_B , is 5.4 Ohm. The area of the copper stopping block was 0.50 cm². Thus

$$\theta_n(\text{electrons/cm}^2) = 2.8 \times 10^{12} V_F \times t \text{ (V}\cdot\mu\text{s)} \quad (18)$$

The dose delivered by the beam is estimated by using an effective energy loss rate of 28 MeV cm²/gm for 250 keV electrons. Thus

$$D(\text{rad}) = 1.2 \times 10^5 V_F \times t \text{ (V}\cdot\mu\text{s)} \quad (19)$$

The equivalent circuit for the calorimeter is shown in Figure 10. Since the input impedance of the calorimeter amplifier is large compared to 2 kOhm, only voltage division between the wire resistance and grounding resistance appears. The electron energy fluence is related to the output voltage by:

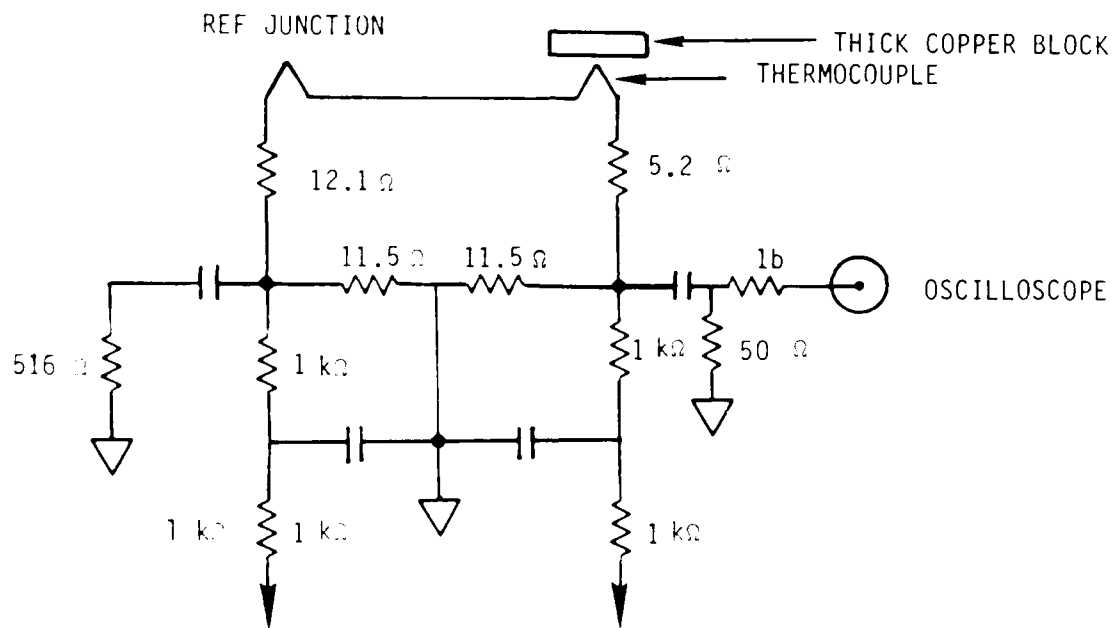


Figure 8. Monitor circuit.

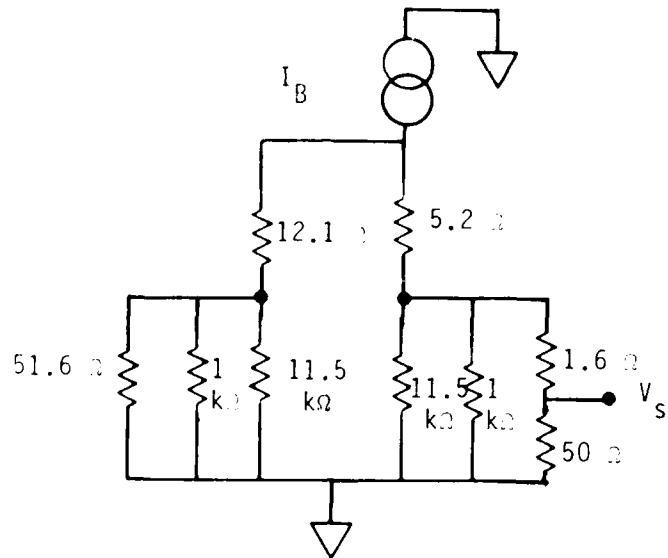


Figure 9. Faraday cup equivalent circuit.

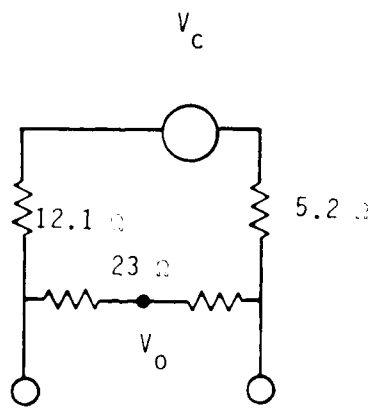


Figure 10. Calorimeter equivalent circuit.

$$\theta_E (\text{J/cm}^2) = \Delta V (\mu\text{V}) \times \left(\frac{40.3}{23} \right) \times \frac{1^\circ\text{C}}{40\mu\text{V}} \times 0.089\text{cm} \times \underbrace{8.9 \frac{\text{gm}}{\text{cm}^3} \times 0.035 \frac{\text{cal}}{\text{gm}^\circ\text{C}} \times 4.185 \frac{\text{J}}{\text{cal}}}_{\text{Specific Heat}}$$

Resistive
Divider
Thermocouple
Sensitivity
Calorimeter
Thickness

$$= 5.1 \times 10^{-3} \Delta V (\mu\text{V}) \quad (20)$$

If we assume an average energy for the electrons of 250 keV the electron number fluence is

$$\begin{aligned} \theta_n (\text{electrons/cm}^2) &= \theta_E / 2.5 \times 10^5 \text{ eV} \times 1.6 \times 10^{-19} \text{ C/electron} \\ &= 2.5 \times 10^{13} \theta_E (\text{J/cm}^2) \\ &= 1.3 \times 10^{11} \Delta V (\mu\text{V}) \end{aligned} \quad (21)$$

Assuming the energy loss for a 250 keV electron is 2.8 MeV cm²/gm, the dose in a thin sample is

$$D(\text{rad}) = 4.8 \times 10^3 \Delta V (\mu\text{V})$$

For the thin calorimeter, no such circuit was required, because they did not double as Faraday cups. These 1 mil copper calorimeters read the average dose deposited in a small fraction ($\approx 1/6$) of the electron range

$$D(\text{rad}) = \Delta V (\mu\text{V}) \times \frac{1^\circ\text{C}}{40 \mu\text{V}} \times \underbrace{\frac{0.035 \text{ cal}}{\text{gm}^\circ\text{C}} \times 4.185 \frac{\text{J}}{\text{cal}}}_{\text{Specific Heat}} \times \frac{10^5 \text{ rad}}{\text{J/gm}}$$

Thermocouple
Sensitivity
Specific
Heat
Unit
Conversion

$$= 3.7 \times 10^2 \Delta V (\mu\text{V}) \quad (22)$$

The foregoing calculations deduce the dose and dose rate at the rear wall of the sample chamber from measurements at that location. Additional corrections must be applied for the following effects:

1. The electron beam diverges from its entrance into the sample chamber to the rear wall, because it is scattered in the entrance foil (3 mil aluminum) and in the air inside the chamber.
2. The effective area of the electron beam increases inversely as the dose decreases from the entrance foil surface to the rear wall.
3. The gas sample includes volumes not exposed to the electron beam, into which the new gas species formed in the beam area will diffuse.
4. The ion chamber is located behind the back wall of the main sample chamber, resulting in a lower dose inside the ion chamber than that along the optical path in the main chamber.

The effective dose, area and path length depend on the specific measurement and the time scale.

1. Measurements of the electron conductivity were made on a relative basis, so that absolute calibration of the dose rate inside the ion chamber was not needed to deduce accurate ratios of conductivity to dose rate. However, an estimate of the dose produced during a single pulse is required to interpret the data on relative conductivity between the early and late part of an ionization pulse. During this measurement no significant diffusion of the gas species can take place.

Therefore, the dose is that in the core of the electron beam penetrating the ion chamber. The ratio between current densities in the Faraday cup on the back wall of the main sample chamber and the rear of the ion chamber was typically a factor of 18. This is mostly due to the divergence of the electron beam after it passes through the collimator in front of the ion chamber. A reasonable estimate for the active volume of the ion chamber, which is approximately half as far from the collimator as the Faraday cup behind the ion chamber, is a dose rate and dose smaller than at the rear of the main chamber by a factor of 4.

2. For the early time ($\ll 1$ min) optical measurements the effective dose is that along the center line of the main chamber (i.e. along the optical path) and the effective path length is four times (for the four passes of the optical path through the irradiated volume) the width of the electron beam at the center of the chamber. The beam width at the incident surface is determined by the Excitron source to be 100 cm. As shown in the Appendix, the electron beam is very heavily scattered in the anode foil and in the air inside the sample chamber. The dose at the center line, along which the optical beam is projected, is estimated to be approximately 1.7 times the dose at the back wall (see Appendix). The irradiated area is delimited by aluminum blocks that border the exposed gas.
3. For late time ($\gg 1$ min.) optical measurements and for the effect of ionization-formed species on the conductivity measured in the ion chamber on subsequent Excitron pulses, the effective dose must be averaged over the sample chamber, including the unirradiated gas volumes in the portion of the

optical path outside the beam and in the gas-handling system. A reasonable estimate is that the average dose is decreased from the mid-plane value by an additional factor of 1.5 for gas dilution, but that the effective optical path is increased by a factor of 1.15 to account for the diffusion of smog species into the regions of the optical path outside of the electron beam. For linear response estimates, this is equivalent to retaining the 4 m optical path but increasing the effective dose along that path by a factor of 1.15.

In summary, starting with the dose measured in the Faraday cup at the rear of the main chamber, the following factors are applied to estimate the effective dose:

1. For comparing the response of the ion chamber early and late in the same pulse: 0.25.
2. For optical absorption measurements at early times (<1 min) from a single ionization pulse: 1.7.
3. For ion chamber measurements of the effect of accumulated ionization from multiple pulses: 1.13.
4. For optical measurements at late times (< 1 min after one pulse, or cumulative effects of multiple pulses): 1.3.

It was our intention to cross check the Faraday cup measurements with thin and thick calorimeter data. The thick calorimeters measure the total electron energy fluence; the electron number fluence and dose can be deduced from knowledge of the electron particle energy and specific energy loss. For example, we can compare the results from Shot 183 as follows:

The Faraday cup signal averages to 0.7 V for a total pulse length of 5.4 μ s. This corresponds to a dose at the Faraday cup of 450 kRad. The thick calorimeter recorded a thermocouple deflection of 22 μ V, which produces a calculated dose of only 100 kRad. It is clear that the Faraday cup value is the reasonable one, and that there is a serious problem with the calorimeter reading. It is not clear what the problem is. During the experiment the entire chart recording system, including calorimeter amplifiers, was calibrated with a known voltage source placed at the calorimeter signal input point. The thin calorimeter readings were also in error; the doses inferred from their voltages were even smaller than those from the thick calorimeters. The only reasonable recourse was to ignore the calorimeter data and to note that there is a need to perform a future experiment to check the calorimeter technique, as applied to low energy electron beams, such as those produced by the Excitron source. A similar problem was encountered once before (Ref. 8).

Given the correction factors discussed above, a typical 5 μ s Excitron pulse delivered approximately 800 kRad along the center line of the sample chamber, which was decreased to an average dose of 530 kRad averaged over the entire gas volume, and 610 kRad normalized to the standard 4 m optical absorption path.

SECTION 6 CALIBRATION SPECTRA

As a calibration, spectra were run with various gas samples present in the chamber in known amounts. Figure 11 is a comparison of the spectra of vacuum (pressure = 0.001 Torr) to that of dry air at 1 atm pressure. The two are indistinguishable, both showing slight absorption lines centered at $5.85 \pm 0.05 \mu\text{m}$ and $6.40 \pm 0.05 \mu\text{m}$, presumably due to absorption in water vapor in the short optical paths outside the sample chamber. The only water bands in our range ($3 < \lambda < 10 \mu\text{m}$) of sufficient intensity (Ref. 9) are centered in bands at $6.644 \pm 0.05 \mu\text{m}$ and $5.87 \pm 0.05 \mu\text{m}$ (see Fig. 12). Further, all spectra were calibrated to the water window at $\lambda = 6.2 \mu\text{m}$. In Figure 11, the peak is located at $\lambda = 6.2 \pm 0.05 \mu\text{m}$. For these reasons, it is reasonable to assume that the weak bands seen in the spectra of Figure 11 are due to absorption caused by moisture present between the chamber and the IR source and detectors. In Figure 13, the spectrum of dry air at 1 atmosphere is compared to that of wet air (i.e., H_2O at 17 torr and air added to a total pressure of 1 atm). The only difference between the two is increased absorption at 5.85 and 6.4 μm in the wet air spectrum, which indicates that the above assumption is valid. Using the water peak to establish the absolute wavelength scale results in an estimated wavelength calibration accuracy of $\pm 0.05 \mu\text{m}$.

The absorption equation is

$$\frac{I}{I_0} = \exp[-\mu NL] \quad (23)$$

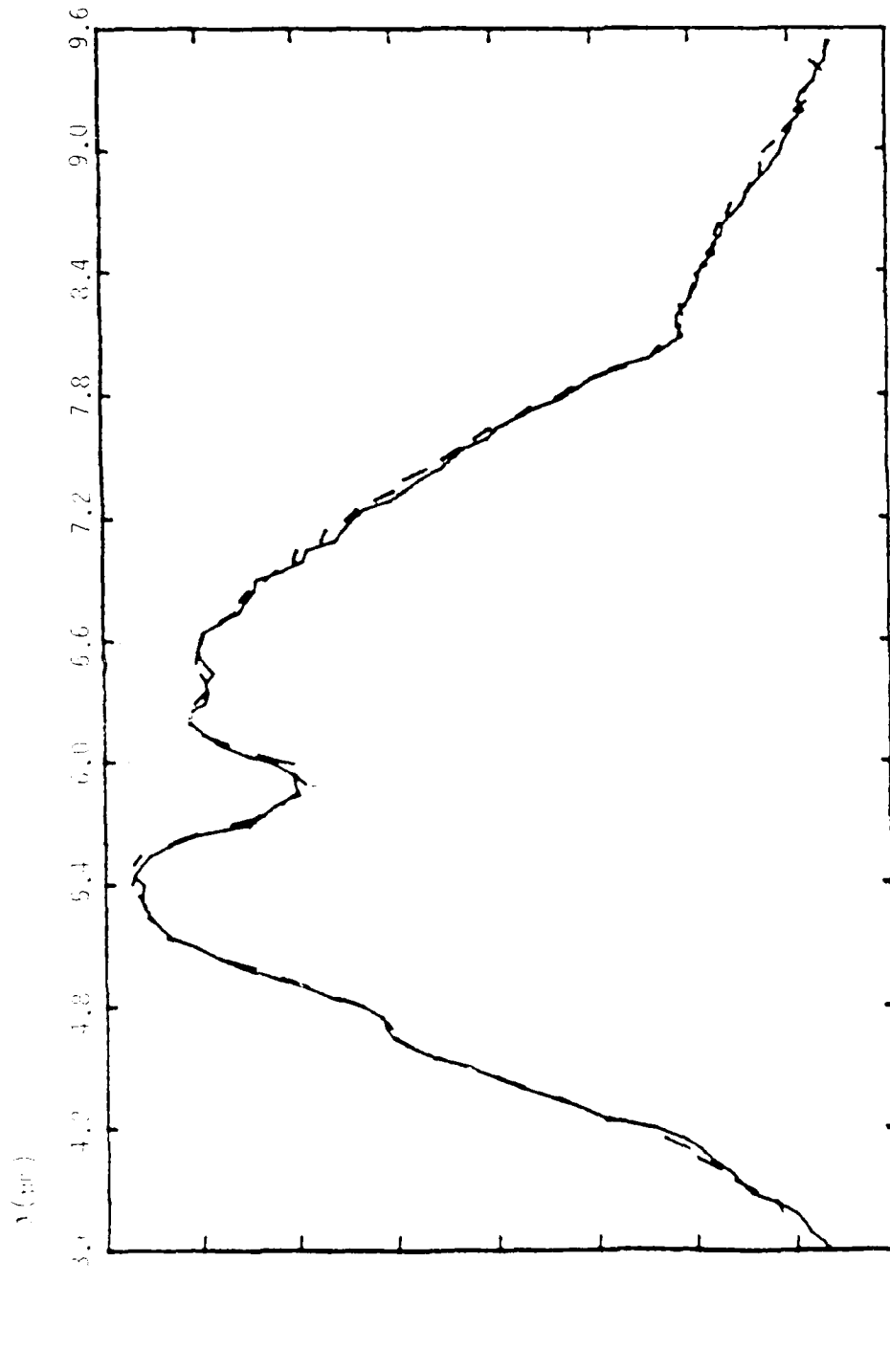


Figure 11. Comparison of spectra of "vacuum" and dry air at one atmosphere pressure.

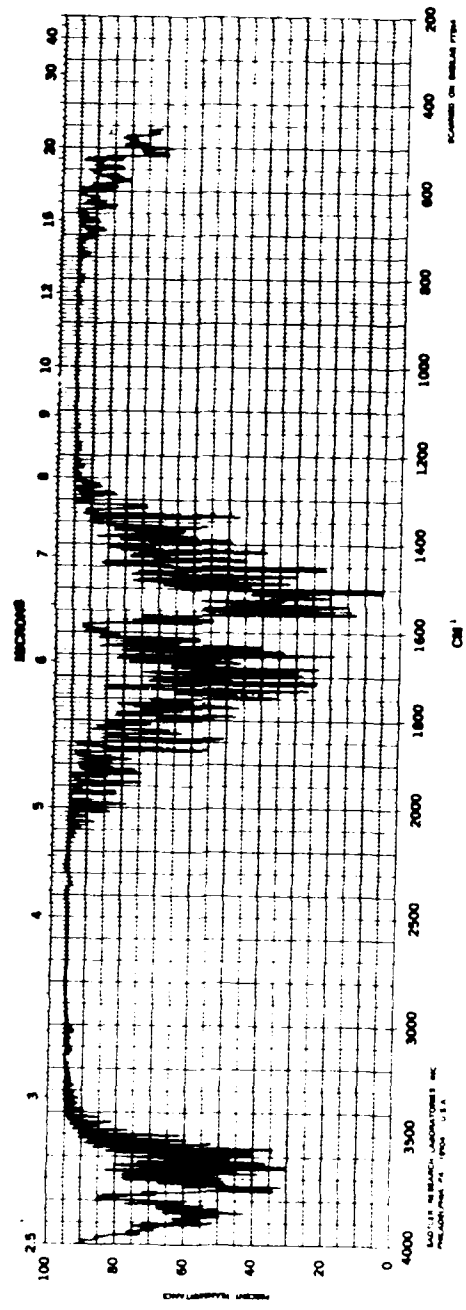


Figure 12. High resolution spectrum of water (Ref. 9).

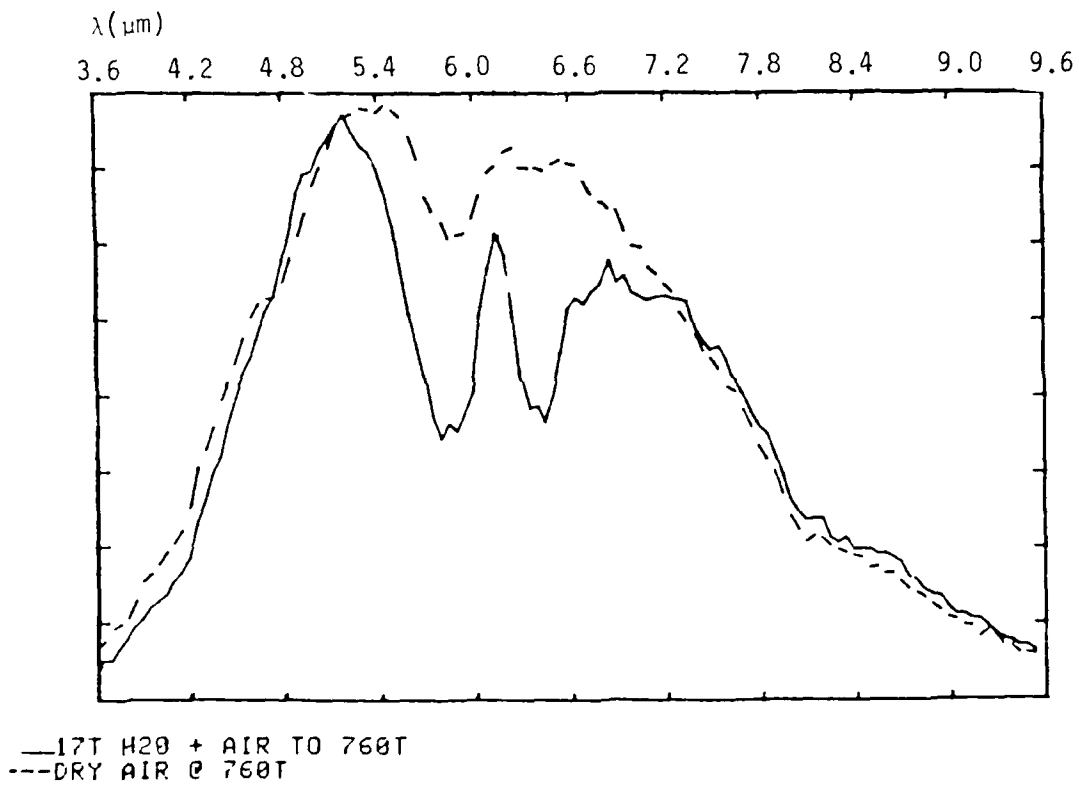


Figure 13. Comparison of spectra of dry and moist air.

where μ is the absorption coefficient (in $\text{cm}^2/\text{molecule}$)
 N is the concentration of the species (in $\text{molecules}/\text{cm}^3$)
 L is the total optical path length
 and I/I_0 corresponds to the relative change in intensity of the spectrum due to absorption

The decrease in intensity in the wet air spectrum of Figure 13 at $\lambda = 5.85 \mu\text{m}$ is approximately $I/I_0 = 0.57$ (where I is the voltage reading at the lowest point in the $5.8 \mu\text{m}$ absorption line of the wet air spectrum and I_0 is the voltage reading at the same point in the dry air spectrum). The concentration of a species at a pressure P is given by

$$N = \frac{P}{RT} \quad (24)$$

where P is the pressure in atmospheres
 R is a constant ($1.37 \times 10^{-22} \text{ cm}^3 \cdot \text{atm}/\text{molecule} \cdot \text{K}^\circ$)
 and T is the temperature of the sample (in Kelvin $^\circ$)

The concentration of water molecules at a pressure of 17 T (0.02 atmospheres) and temperature $T = 293^\circ\text{K}$ is $[\text{H}_2\text{O}] \approx 5.0 \times 10^{17} \text{ molecules}/\text{cm}^3$. The total optical path length of the chamber for full spectra is $L = 440 \text{ cm}$.

The absorption coefficient per molecule of water, ϵ , was estimated from Reference 10. We calculated the sum of line strengths over the wavelength range 5.80 to $5.90 \mu\text{m}$ to be $8.38 \times 10^{-20} \text{ cm}/\text{molecule}$. Dividing by the range in wave number, yields a line strength per unit wave number of $2.9 \times 10^{-21} \text{ cm}^2/\text{molecule}$. The column density of water molecules is $2.2 \times 10^{20} \text{ molecules}/\text{cm}^2$. The predicted transmission is $\exp -(2.9 \times 10^{-21} \times 2.2 \times 10^{20}) = 0.53$, in excellent agreement with the measured transmission of 0.57.

Figure 14 is a comparison of the spectrum of dry air at 1 atmosphere to that of NO_2 at a pressure of 0.3 Torr with air added to a total of one atmosphere. It should be noted here that after NO_2 was first added to the chamber the pressure reading dropped, requiring the addition of more NO_2 gas. This was probably due to adsorption of the NO_2 molecules onto the walls of the chamber. The spectrum has a strong absorption line centered at a wavelength of $6.0 \mu\text{m}$, with a relative change in intensity of $I/I_0 \approx 0.8$. The product of the absorption and wavenumber integrated over this line is measured to be 15 cm^{-1} . The absorption coefficient for a band from $6.03 \mu\text{m}$ to $6.45 \mu\text{m}$ is reported to be $6.11 \times 10^{-17} \text{ cm/molecule}$ (Ref. 11). The NO_2 spectrum in this range is shown in Figure 15 (Ref. 12). For the 440 cm optical path this corresponds to a density of NO_2 molecules of $5.6 \times 10^{14} \text{ cm}^{-3}$. The concentration initially injected into the sample chamber was considerably larger: $1 \times 10^{16} \text{ cm}^{-3}$. Moreover, the center of the NO_2 band in our spectrum is offset by $\approx 0.2 \mu\text{m}$. This is just outside our uncertainty range.

Figure 16 compares the spectrum of a moist NO_2 sample (i.e., 0.3 Torr NO_2 , 17 Torr H_2O and air added to a pressure of 1 atm) to that of moist air without NO_2 . The NO_2 line seen previously in the dry sample at $\lambda = 6.0 \mu\text{m}$ is absent. Only the H_2O absorption is seen.

When the spectrum of a Nitric Acid solution and moist air sample is compared to simply moist air (as in Fig. 17) no HNO_3 lines are apparent. Again, only the water absorption is apparent. Even when a sample of water at only 11 Torr is compared to a sample of HNO_3 solution at about the same pressure, (see Fig. 18) only the water lines at $5.85 \mu\text{m}$ and $6.4 \mu\text{m}$ are apparent. Nevertheless, the published absorption spectrum of HNO_3 (Ref. 12) contains strong lines that should be observable outside the water absorption bands (Fig. 19).

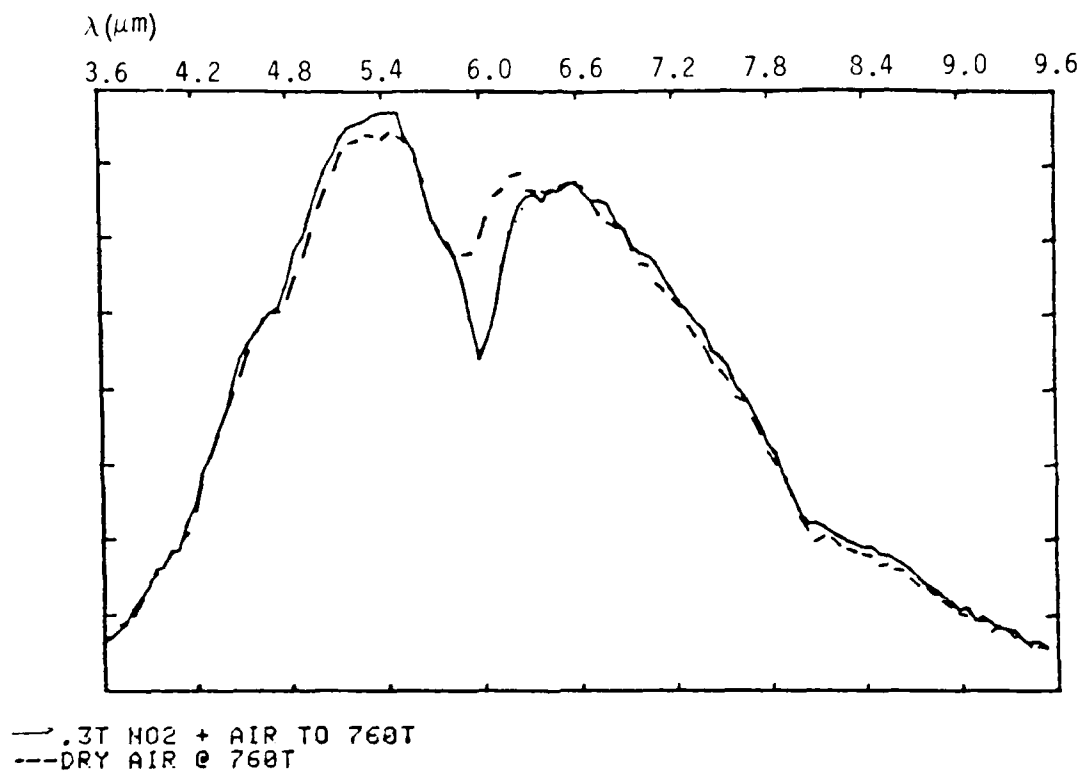


Figure 14. Comparison of spectra of dry air and nitrogen dioxide with dry air added to one atmosphere.

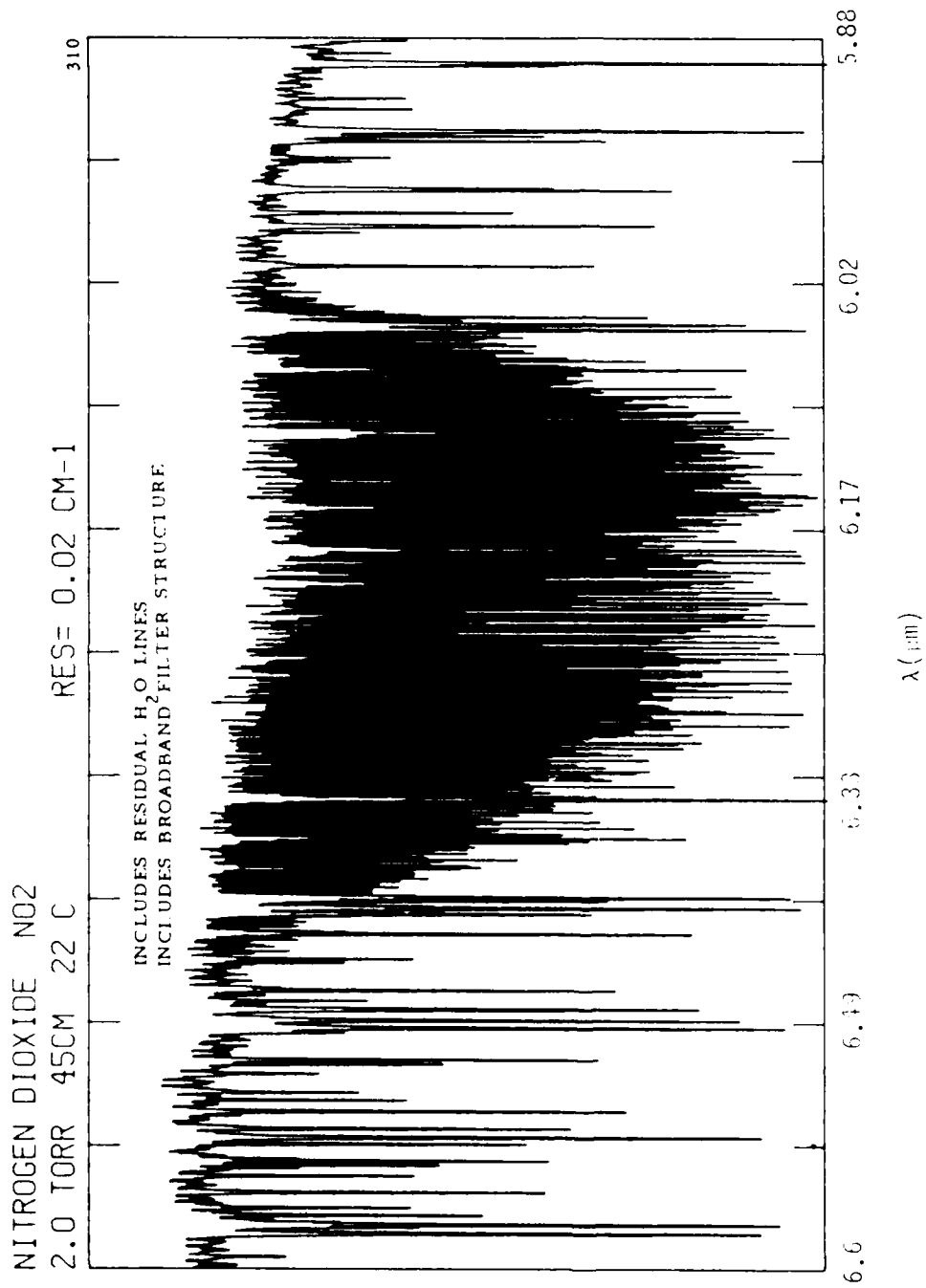
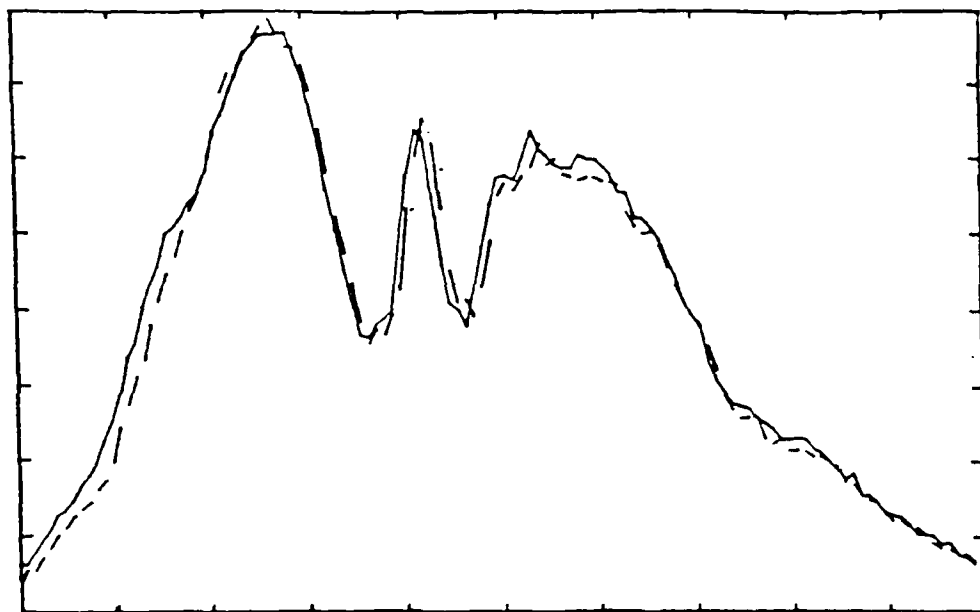


Figure 15. High resolution spectrum of nitrogen dioxide.

λ (microns)
3.6 4.2 4.8 5.4 6.0 6.6 7.2 7.8 8.4 9.0 9.6



— .3T NO₂ + 17T H₂O + AIR
--- 17T H₂O + AIR TO 760T

Figure 16. Comparison of spectra of moist air to that of NO₂ and moist air.

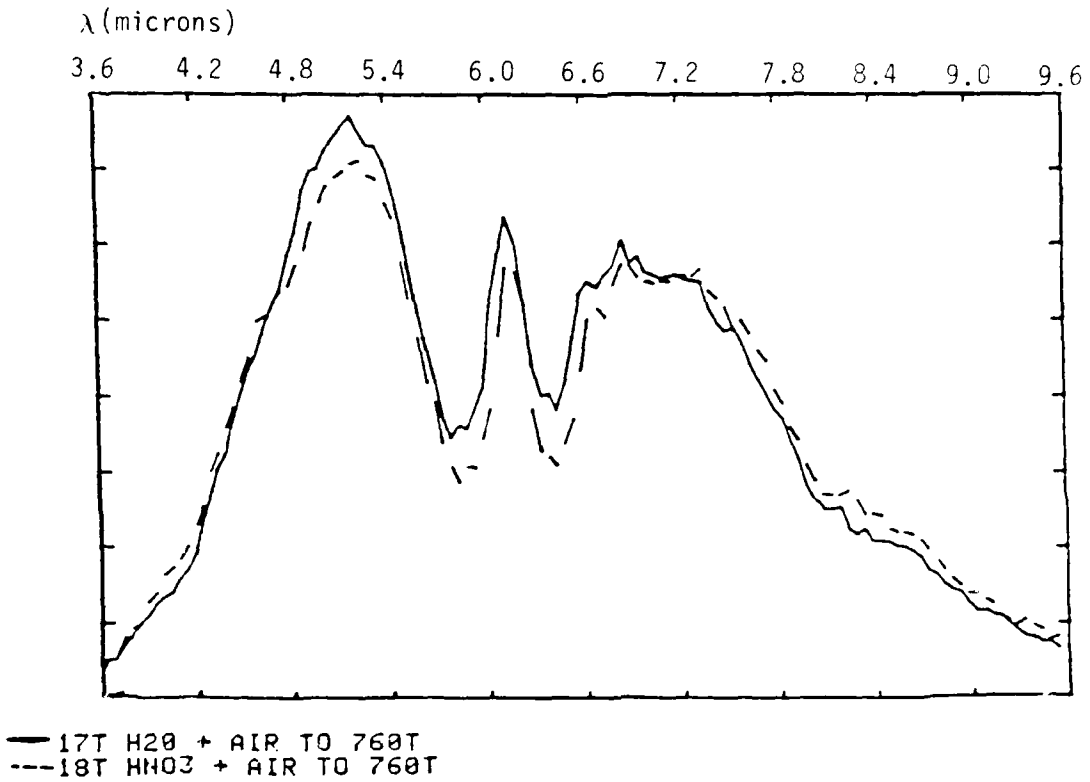


Figure 17. Comparison of spectrum of moist air to that of HNO₃ and moist air.

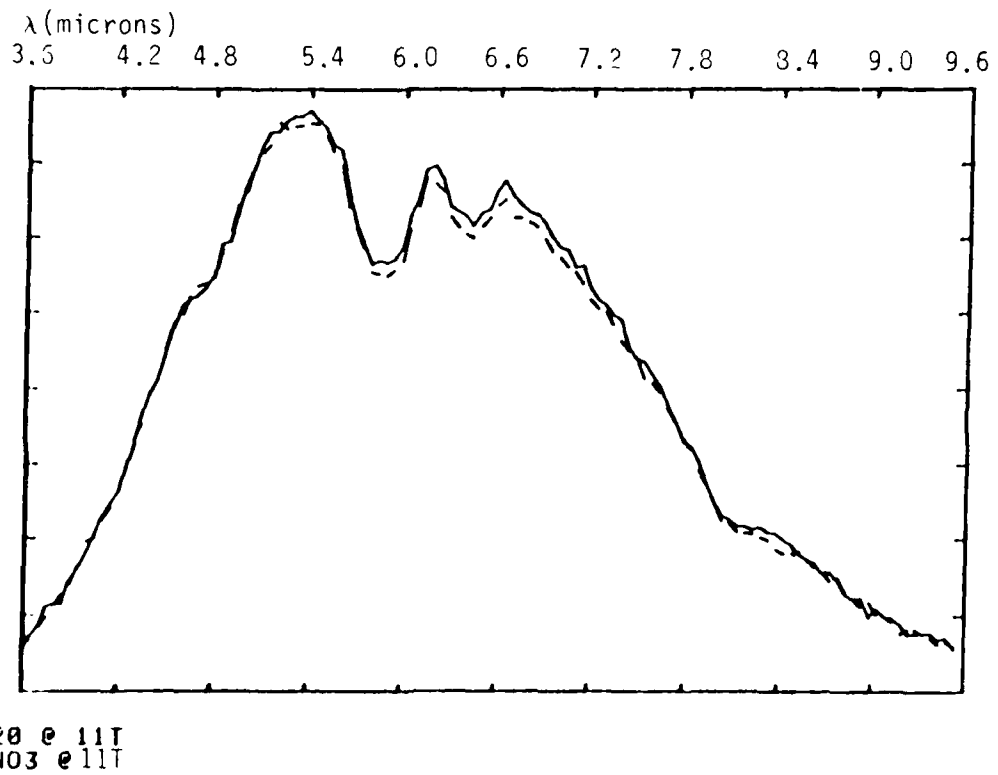


Figure 18. Comparison of spectrum of H₂O to that of HNO₃/H₂O at the same pressure.

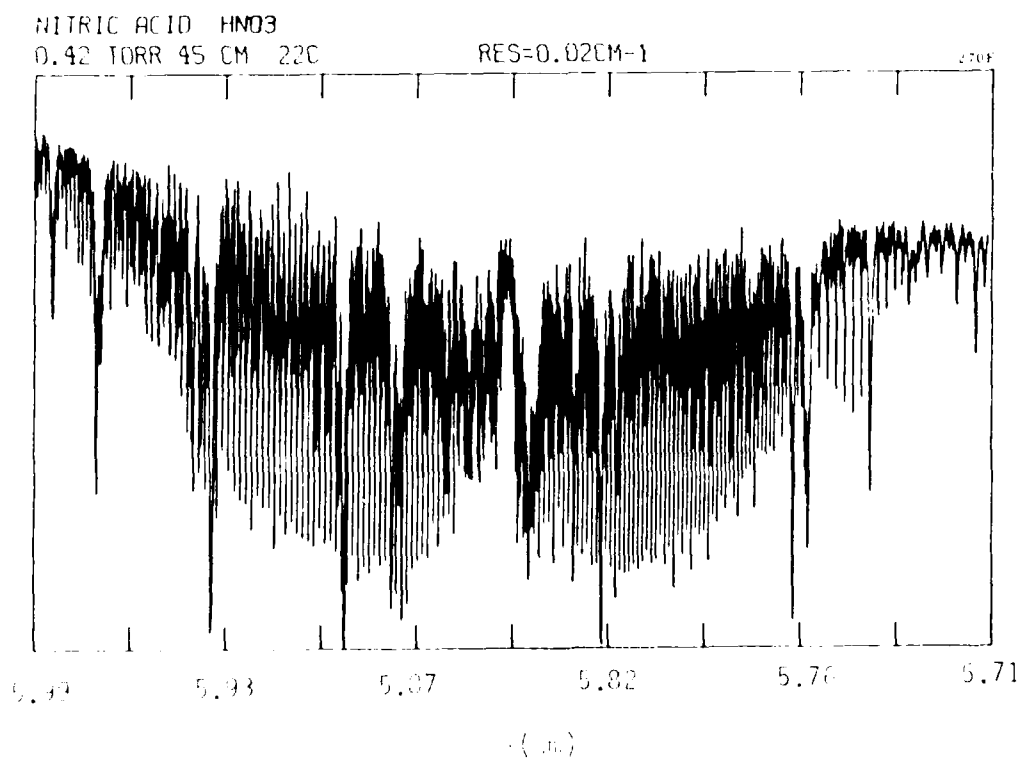
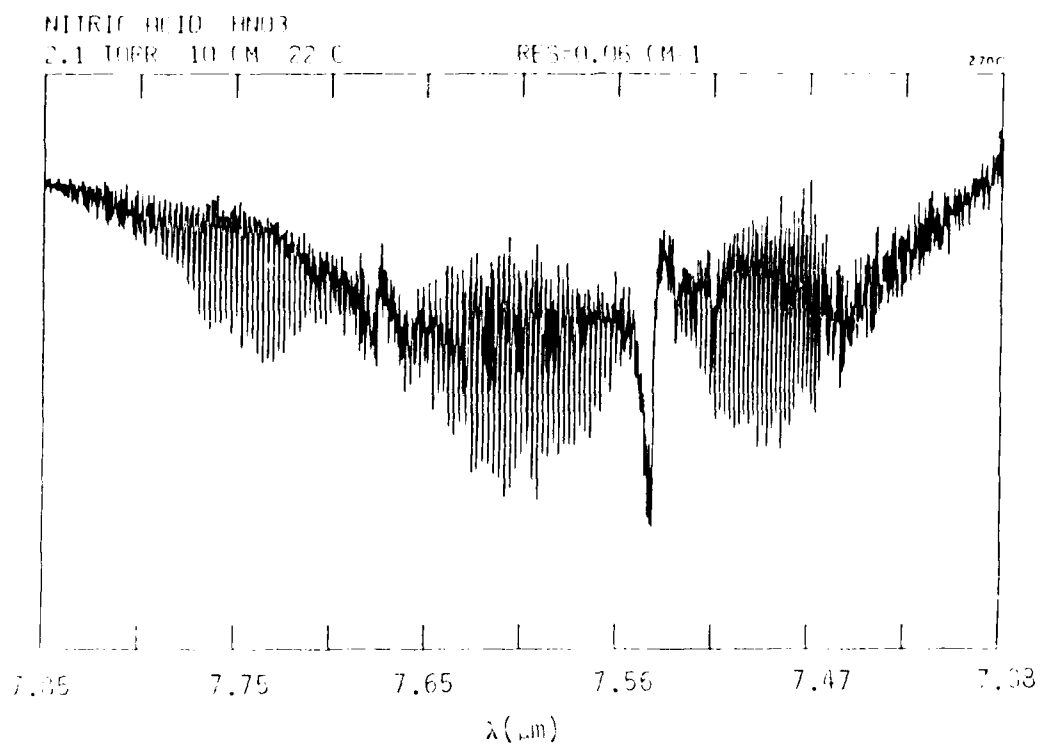


Figure 19. High resolution spectra of nitric acid (HNO₃) lines in our range.

Fog was formed initially when moist air was introduced into the chamber. If spectra were run too soon after introduction of the moist samples, i.e., before the fog disappeared, this showed up as a slight bias in intensity, i.e., lower intensity at the shorter wavelengths, which were measured at the beginning of the scan. The offset due to fog is apparent in the beginning of the spectra of Figures 16 and 17.

The fact that the NO_2 and HNO_3 lines are absent when H_2O is present in the chamber may be due to one of the following reasons:

1. The intensity of the H_2O lines may be large enough to mask the relatively weak intensities of the NO_2 and HNO_3 lines in this range.
2. Attachment of H_2O molecules to molecules of either NO_2 or HNO_3 may change the resonant frequency of these molecules to such an extent that the absorption lines are displaced or otherwise affected.
3. The presence of H_2O molecules somehow induce the diffusion of the species to (and reaction with) the walls of the chamber so that these gases are virtually absent by the time the spectra were run.

The first explanation is possible. As discussed previously, the water lines at 18.5 Torr are already black. The broadness of the bands at this pressure could easily obscure the presence of the lines of other species. However, the absorption due to NO_2 should be observable in the window in the water spectrum at $6.2 \mu\text{m}$.

The displacement of the NO_2 band in the calibration spectra of Figure 14 seems to be in support of 2 above. The water peak at $6.18 \mu\text{m}$ is not displaced, and the center of the NO_2 band is outside of our error range.

Finally, the third explanation is supported by the fact that some of the NO_2 disappeared initially upon being injected into the chamber and larger amounts were required to reach an equilibrium pressure reading.

SECTION 7
EFFECT OF IRRADIATION ON IR ABSORPTION SPECTRA

Three types of IR absorption measurements were made:

1. An IR absorption spectrum was measured before and after exposure to one or more irradiation pulses.
2. The effect of one or more irradiation pulses on the IR absorption at a chosen wavelength was measured.
- 3) The IR absorption at a few selected wavelengths was measured cyclically before and after one or more irradiation pulses.

Since ≈ 8 minutes was required to measure a complete spectrum, the first measurement could only detect long lived absorbing species. The second measurement was capable of few second resolution, but required many pulses to scan many wavelengths. The third method gave intermediate results.

7.1 DRY AIR SPECTRA.

The following results are for gas samples in which only dry air was added to a previously evacuated chamber. Since the chamber was not baked, and previous fillings left absorbed species on the wall, the samples were not absolutely dry. Pressure drifts when the chamber was sealed were slow enough so that the impurity content of the dry air samples is less than 0.1%.

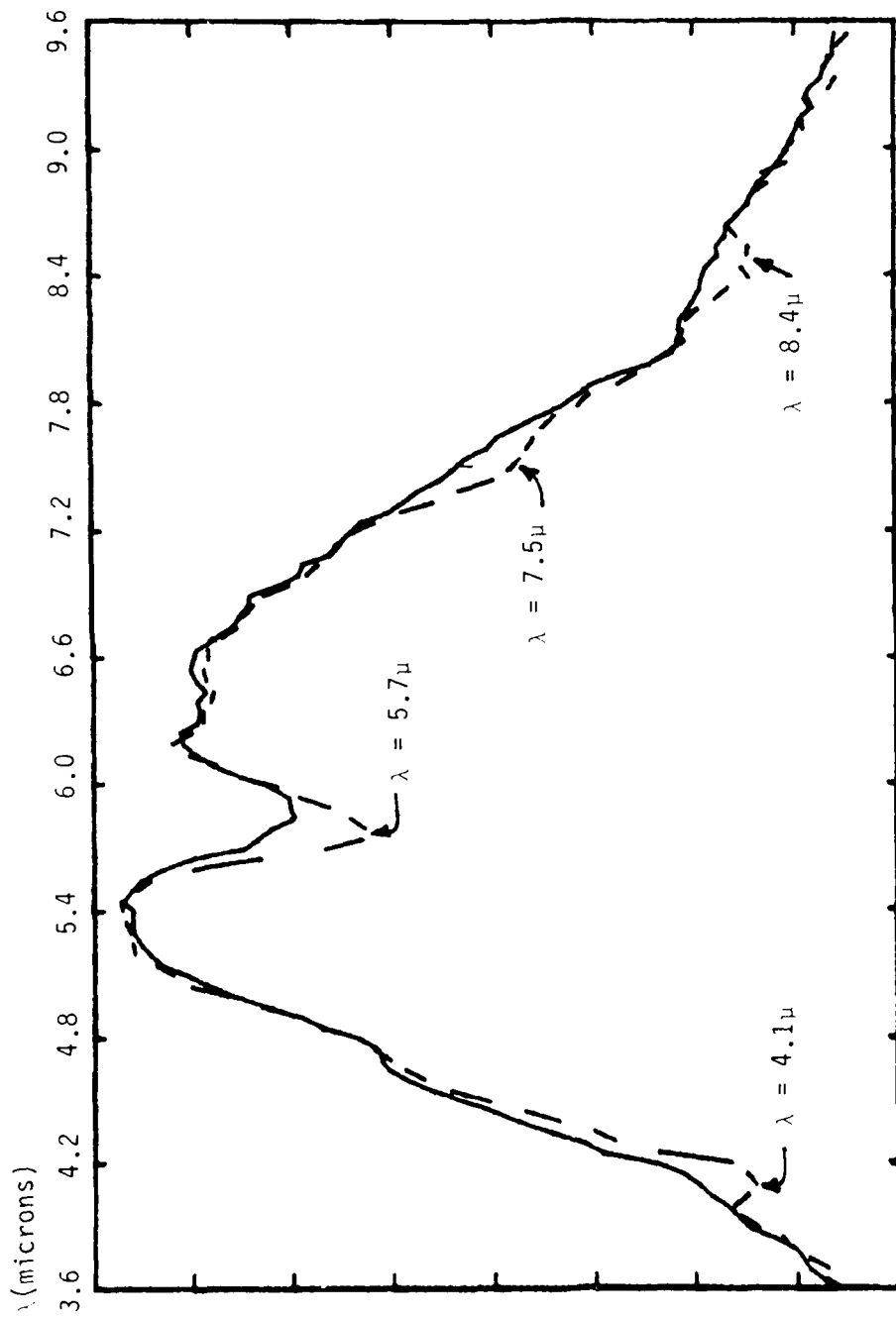
Figure 20 compares the spectrum of "dry" air with the spectrum of a sample of "dry" air exposed to 26 Excitron pulses (an estimated dose of 11 Mrad) during approximately 150 minutes. There are new absorption lines at 4.1, 5.6, 7.5 and 8.4 μm .

A similar comparison for a sample irradiated rapidly (in 2.1 minutes) with only five pulses (≈ 18 Mrad) is shown in Figure 21. Comparing the IR1157 (pre-exposure) and IR1159 spectra shows clearly the extra absorption at 5.7 μm , but not the other ones. This spectrum passed the 5.7 μm point at 2.8 minutes after the last Excitron pulse. Another spectrum taken 10 minutes later (IR1160) illustrates the decay of this absorption band.

The second method (observe absorption at a chosen wavelength before and after a pulse) was used to detect short-lived species with IR absorption bands in the range of 5 to 8 μm .

The absorption near 5.7 μm is illustrated in Figure 22 in the form of strip-chart segments. Each pulse delivered a dose of approximately 0.51 to 0.76 Mrad. A long-lived absorption is observed between 5.5 and 5.8 μm , with a maximum near 5.68 μm . The effective width of this absorption is $\approx \pm 0.2$ μm , which is only slightly greater than instrument resolution. In the low wavelength end (5.6 μm) the absorption appears promptly, but in the high wavelength end (5.8 μm) there is a component that increases in ≈ 0.2 minutes. At intermediate wavelengths (5.68 and 5.7 μm) both components are seen.

An experiment was performed to measure the growth and decay of the absorption at 5.7 μm during and after a sequence of five rapid ≈ 0.5 Mrad Excitron pulses. Figure 23 shows the result, as recorded by the strip chart recorder. The small growth in absorption is evident after each pulse. The change in intensity for each 0.5 Mrad pulse is approximately $\Delta I/I_0 \approx -6\%$.



— DRY AIR @ 760T
--- IRRAD DRY AIR

Figure 20. Comparison of spectra of clean and irradiated dry air (Dose = 30 Mrad).

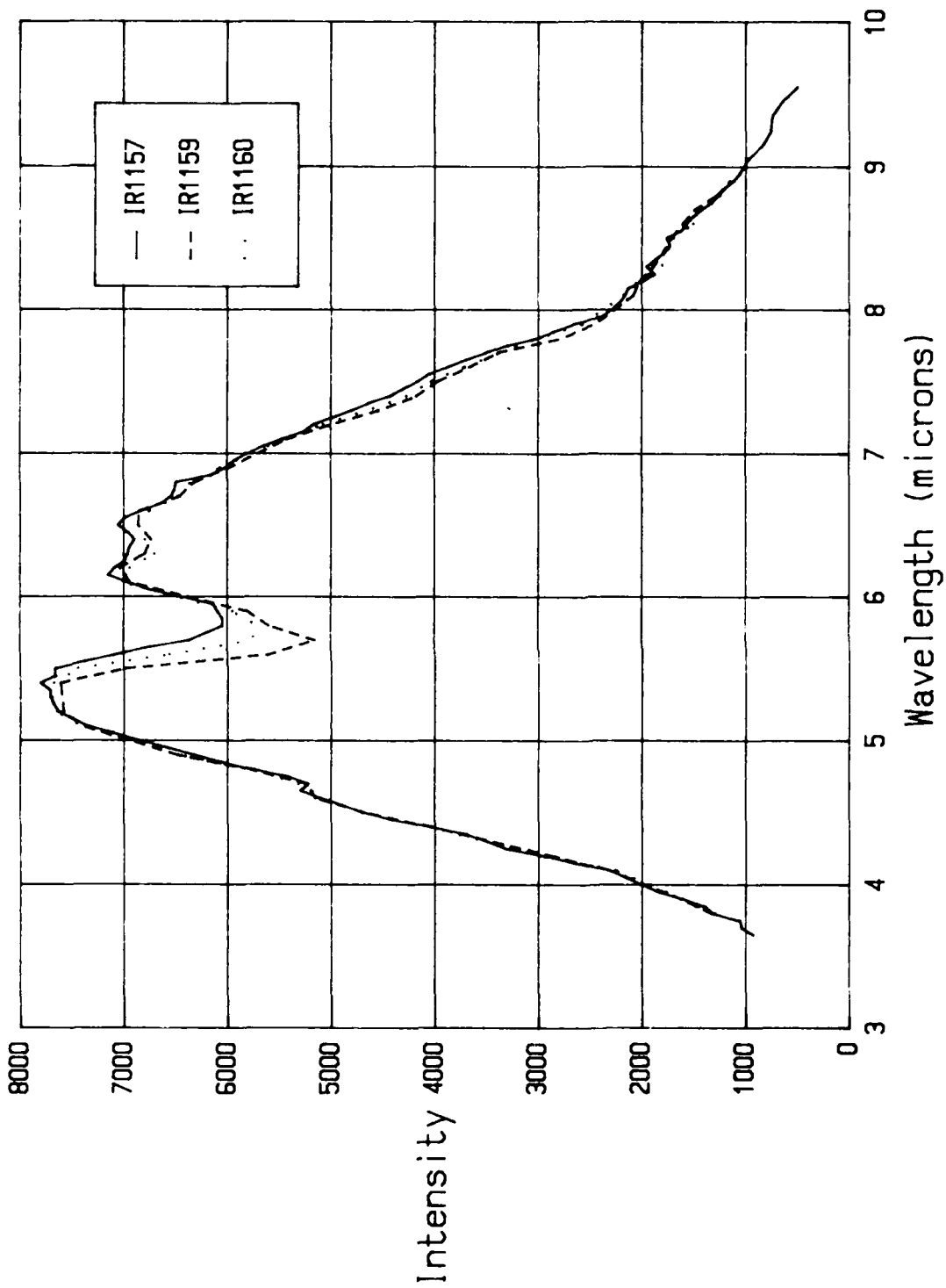


Figure 21. "Dry" air spectra.

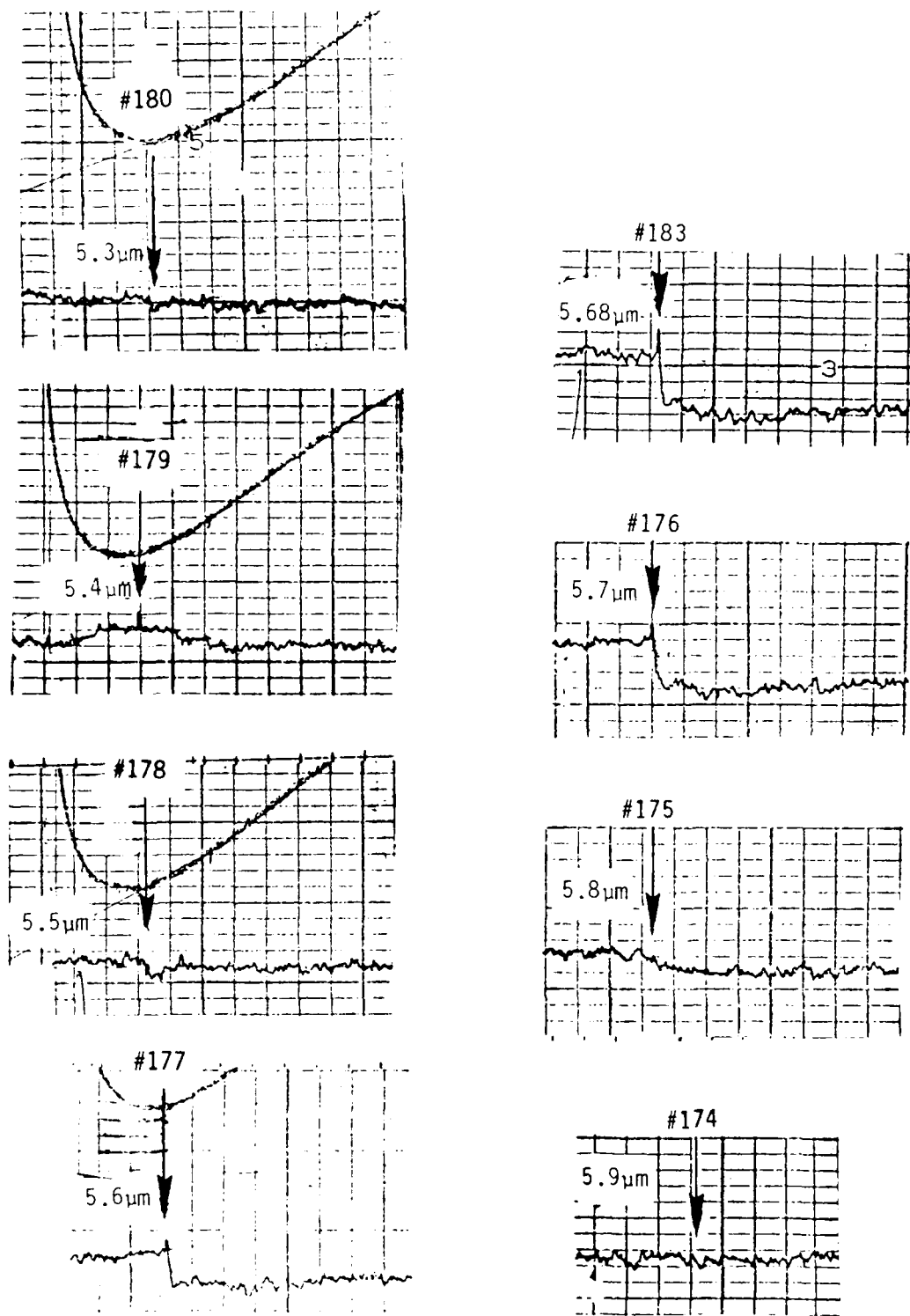


Figure 22. Transient absorption near 5.7 μm .

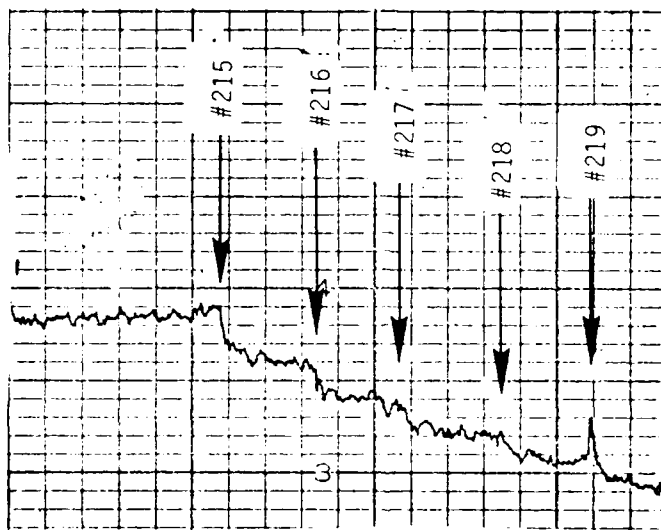


Figure 23. Cumulative absorption at 5.7 μm .

If we assume that F molecules of absorbing species are formed for each ion produced, we can estimate the absorption line strength required to produce the observed attenuation. The density of molecules formed per pulse is 1×10^{15} F molecules/cm³. The effective path length is 4 m, yielding a columnar density of 4×10^{17} F molecules/cm². The 6% absorption has an effective $\Delta(1/\lambda)$ of 62 cm⁻¹. Thus the absorption line strength per molecule is:

$$S = \frac{0.06 \times 62}{4 \times 10^{17} F} = 1 \times 10^{-17} / F \quad (25)$$

This value is comparable to the larger line strengths in NO_2 and HNO_3 , but considerably larger than those in H_2O .

A plot of the $\Delta I/I_0$ vs time after the last pulse is shown in Figure 24, yielding an effective recovery time of 12 minutes.

Although the 5.7 μm absorption band is characteristic of water vapor, it is clear that the radiation-induced absorption is not due to H_2O because:

1. The IR absorption grows too rapidly after e-beam pulsing to be due to water absorbed from the chamber walls, since the IR path is in the center of the chamber and not along the walls.
2. The 5.7 μm H_2O absorption is always accompanied by a 6.5 μm absorption band, which is not observed in either the transient or long-term absorption measurements.
3. The known line strengths in H_2O are too small to account for the observed absorption.

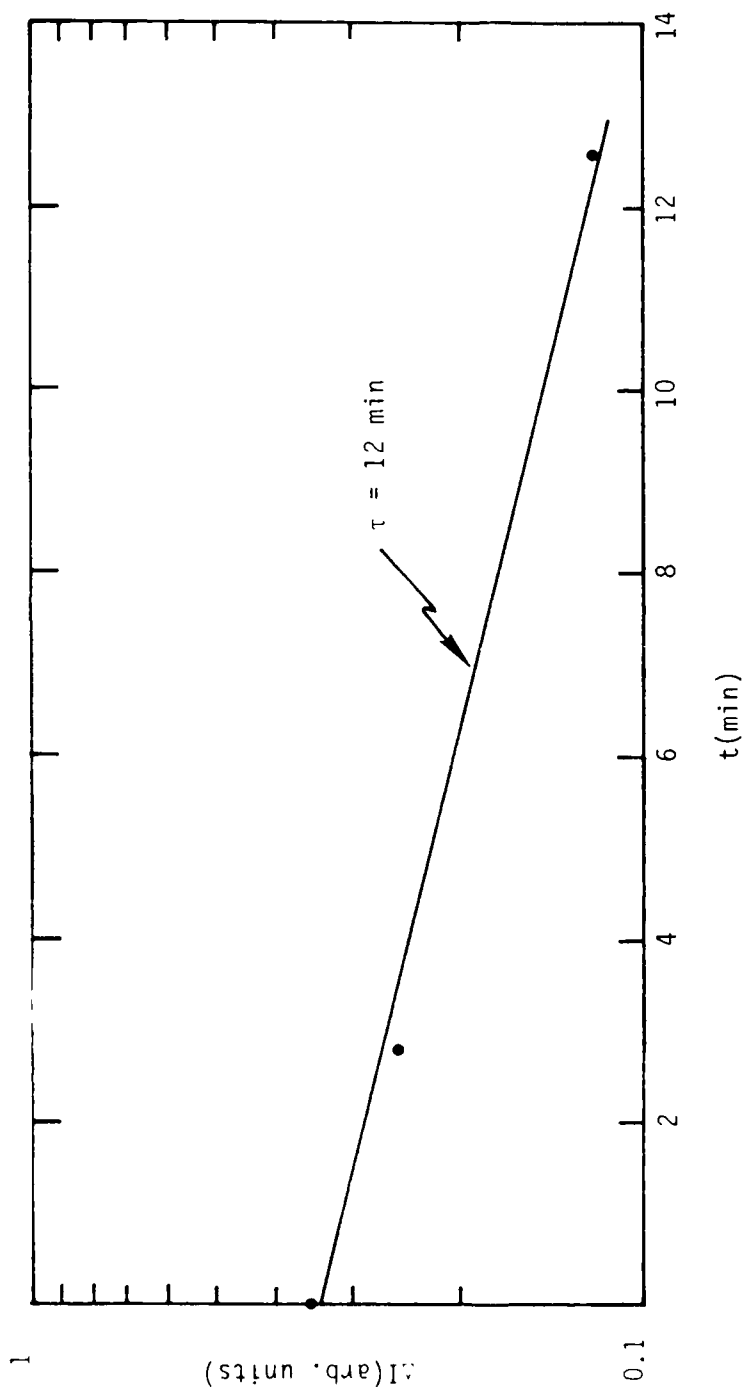


Figure 24. Recovery at $5.7\mu\text{m}$.

Two other transient responses were observed. Figure 25 presents strip-chart segments for the region from 6.1 to 6.3 μm . A very short-lived (≈ 0.1 minute) absorption is observed centered near 6.15 μm with an amplitude $\Delta I/I_0 \approx -6\%$.

A more mysterious response is shown in Figure 26, which presents strip-chart segments for the region 7.3 to 7.7 μm . There is a clear long-lived (> 1 minute) $\approx 5\%$ increase in the detector signal centered at 7.5 μm . This is most likely a fluorescence line since a transient decrease in absorption seems unlikely. Note that 7.6 μm is the location of one of the absorption bands in the heavily irradiated "dry" air sample (Fig. 20). Since the gas sample was exposed to the entire glow-bar spectrum, (i.e., the monochromator was on the detector side) fluorescence excited by shorter wavelength photons could create the observed increase in 7.5 μm photons. The effective relaxation time of the de-excitation process would have to be short compared to 1 ms for the detected signal to appear in phase with the ≈ 900 Hz chopper, which was located at the light source.

7.2 WET AIR SPECTRA.

Figure 27 presents a comparison of the IR absorption spectra for a 2.6% H_2O sample prior and after exposure to ≈ 5 Mrad in ≈ 20 minutes. A small amount of extra absorption is observed in the region 6.6 to 7.4 μm .

The effects of a higher dose, ≈ 28 Mrad, delivered rapidly (in 60 minutes) in 43 Excitron pulses are shown in Figure 28, showing the pre (IR1053) and immediately post (IR1054) irradiation spectra. There is a strong increased absorption at the water window, 6.2 μm , an apparent decrease in absorption in the water peaks, especially at 6.4 μm and a possible slight absorption in the range 7.3 to 7.9 μm . The subsequent recovery is illustrated in Figure 29. The immediately post-irradiation spectrum (IR1054) is compared with a spectrum taken 11 minutes later (IR1054) and

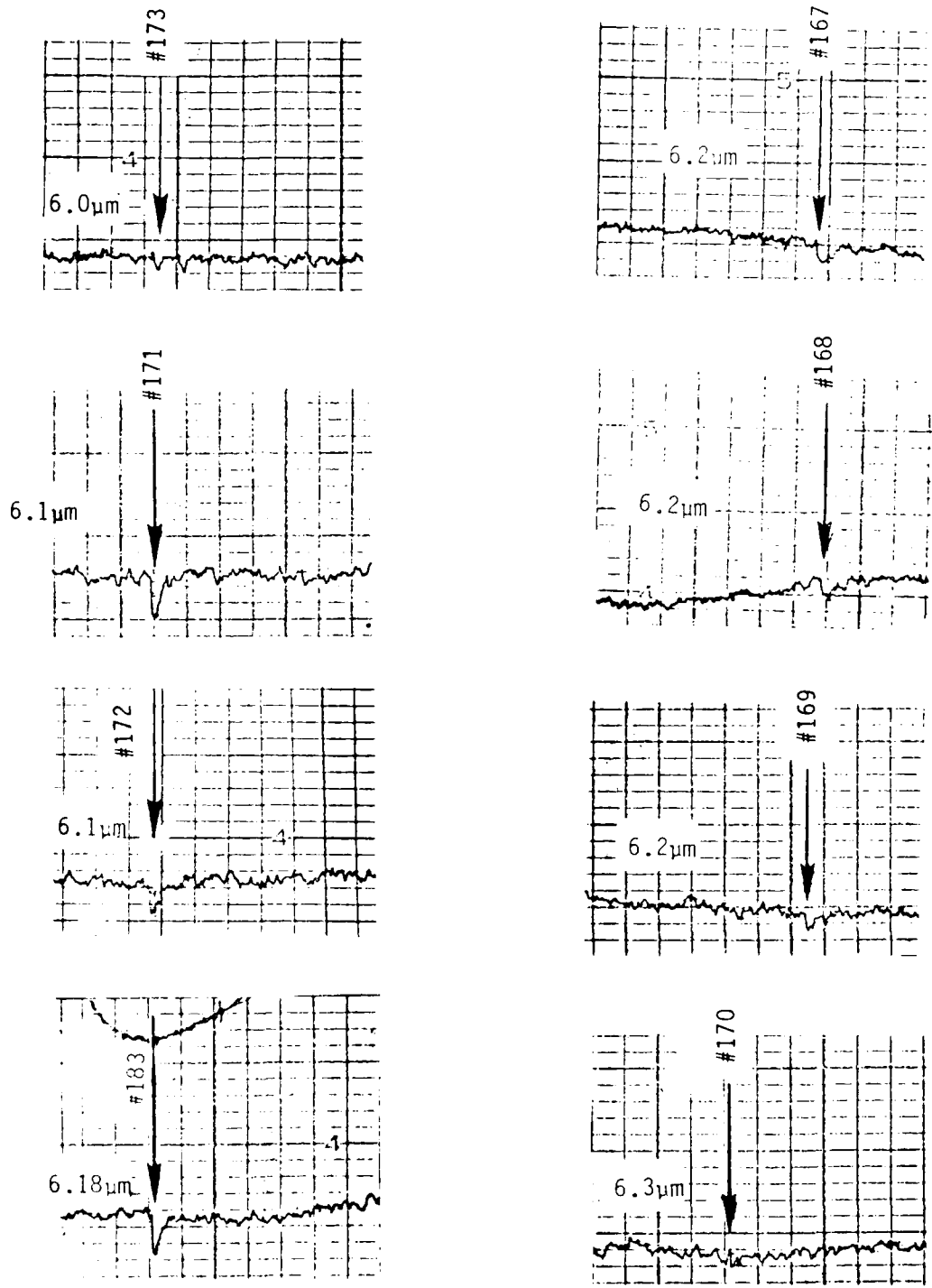


Figure 25. Transient absorption near 6.2 μm .

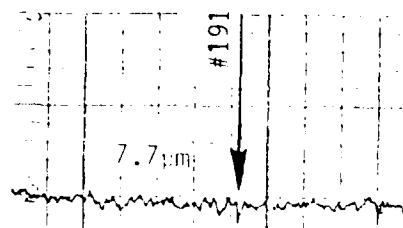
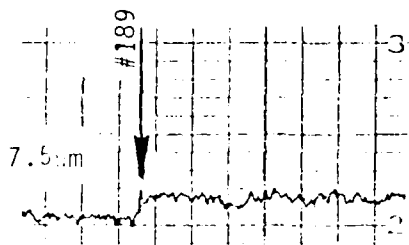
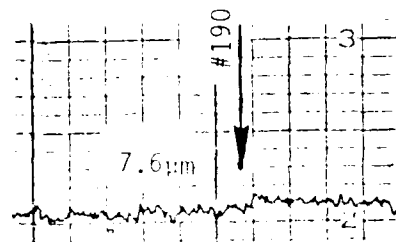
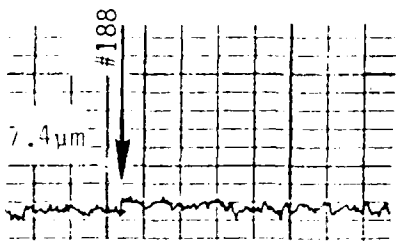
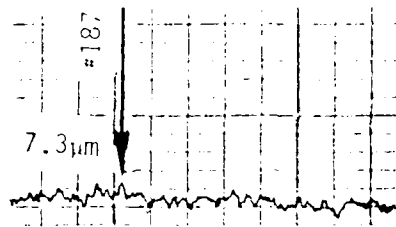


Figure 26. Transient fluorescence near 7.5 μm.

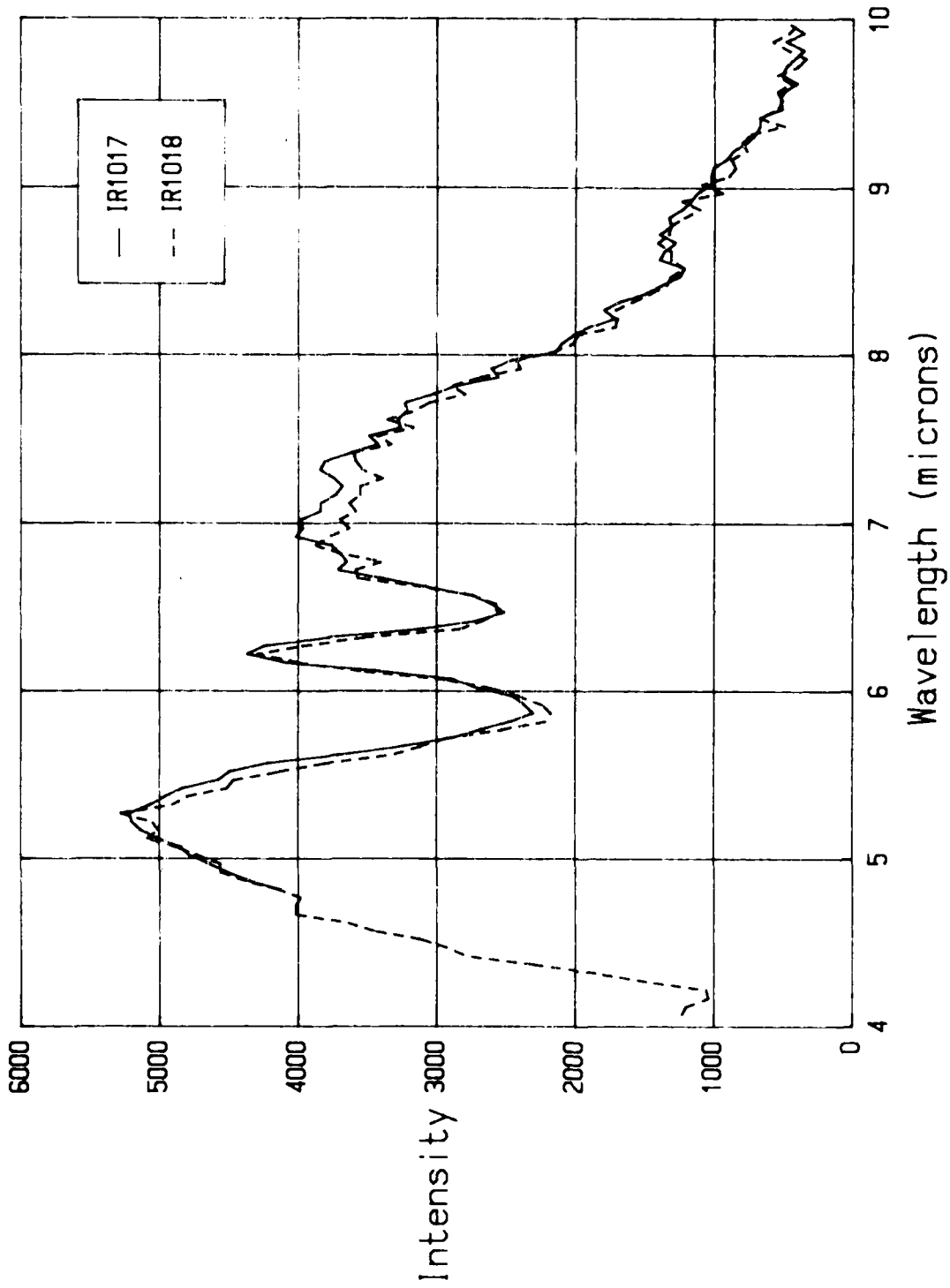


Figure 27. Effect of irradiation on wet air.

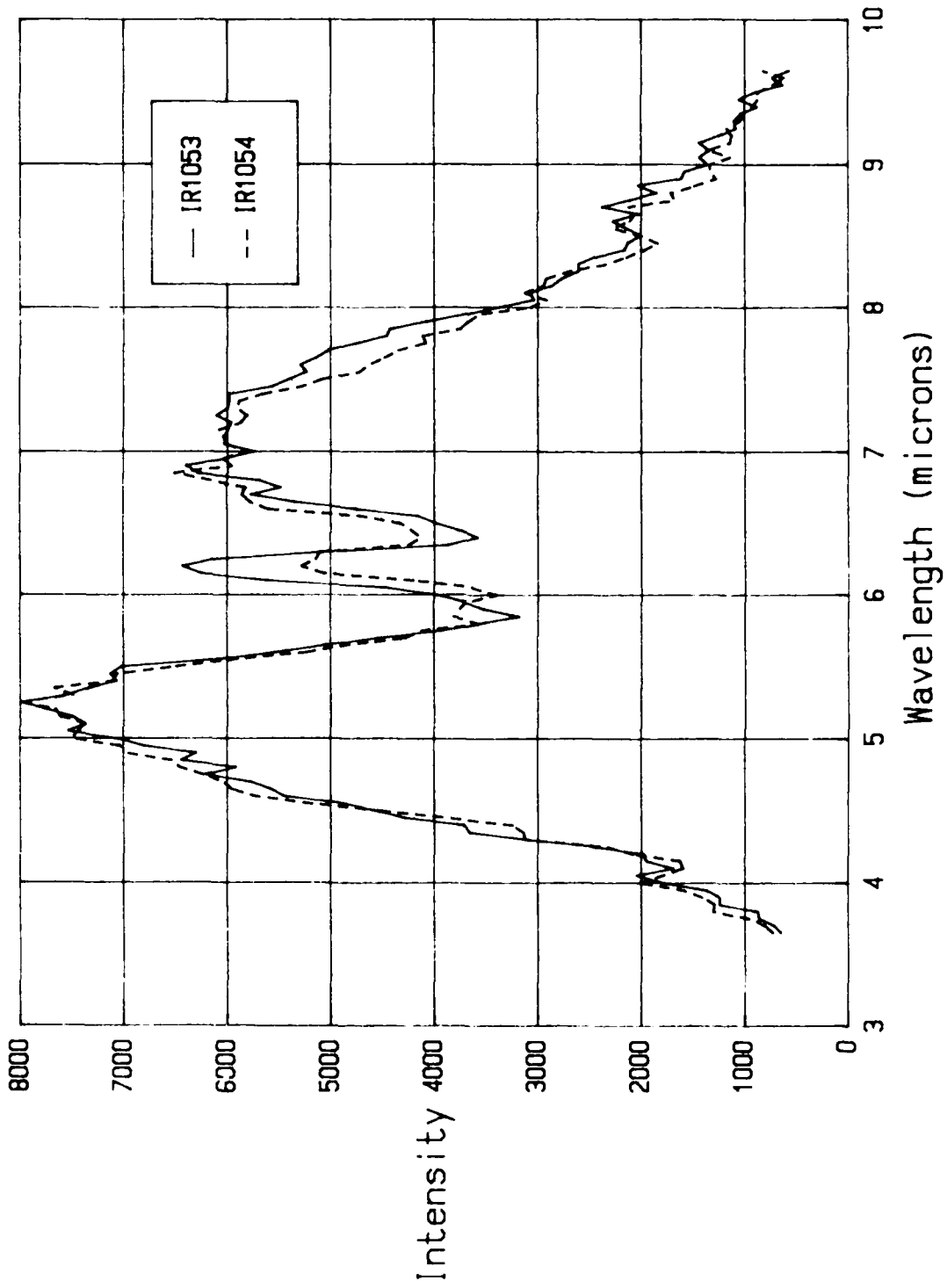


Figure 28. Effect of rapid irradiation on wet air.

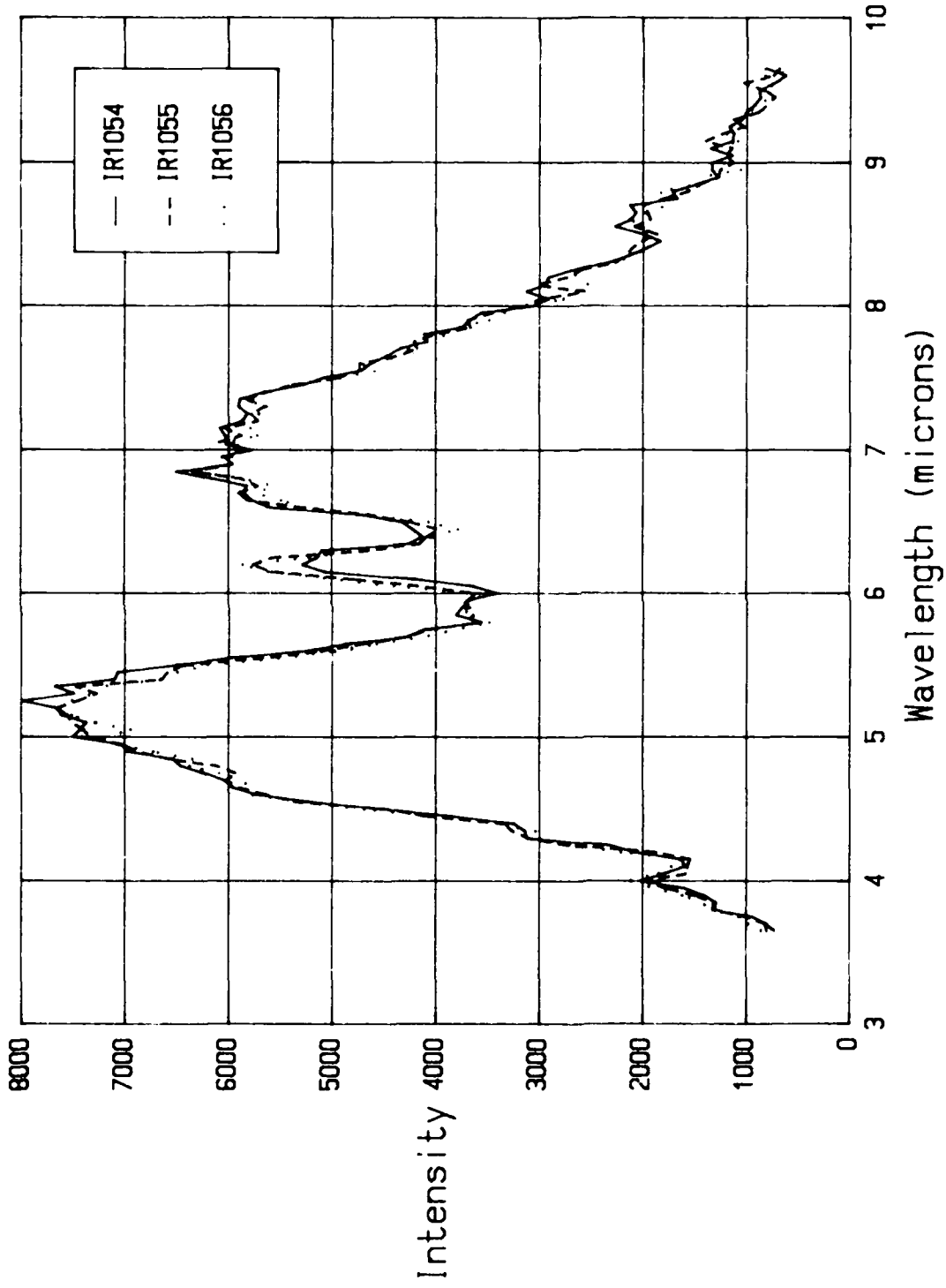


Figure 29. Recovery of absorption in wet air.

another one taken 27 minutes after the end of the irradiation-(IR1056). The recovery of the absorption at the water window at $6.2 \mu\text{m}$ is obvious. Comparing the IR1056 with IR1054 in Figure 28 shows that the recovery is not quite complete.

The results of a rapid exposure of a 2.2% H_2O sample is illustrated in Figure 30. Prior to spectrum IR1046 the sample had been exposed slowly to an accumulated dose of ≈ 3 Mrad. It was then exposed to ≈ 5 Mrad during 7 minutes, followed immediately by spectrum IR1047. The spectrometer passed the $6.2 \mu\text{m}$ wavelength approximately 6 minutes after the end of the irradiation. A second pass through the spectrum is shown in IR1048. It passed the $6.2 \mu\text{m}$ wavelength approximately 18 minutes after the end of the irradiation. Although the effects are smaller than for the larger exposure illustrated in Figures 28 and 29, they are similar. A clear increase in absorption is seen at $6.2 \mu\text{m}$, and a possible decrease in absorption is seen at the water minima. A possible increase in absorption between $7.6 \mu\text{m}$ and $7.9 \mu\text{m}$ is also barely observable. Some recovery is seen at $6.2 \mu\text{m}$ in the latest spectrum.

Measurements taken on wet air by the second method are illustrated in Figure 31. These data indicate an absorption near $6.2 \mu\text{m}$ that appears to have both a short term (≈ 0.2 minute) and a long-term (>1 minute) component. A longer time measurement at $6.15 \mu\text{m}$ is shown in Figure 32, indicating a decay time of approximately 8 minutes. There also appears to be a small transient absorption around $5.7 \mu\text{m}$, as illustrated in Figure 33, and near $7.5 \mu\text{m}$. A series of rapid electron pulses, illustrating absorption at $6.05 \mu\text{m}$, is shown in Figure 34. The decay time of the absorption is approximately 0.4 min.

Measurements were also taken by the third method: sampling a few wavelengths before and after a single electron irradiation pulse. In most cases the change in absorption was too small for a single pulse to provide useful measurements by this method. Figure 35 illustrates these results.

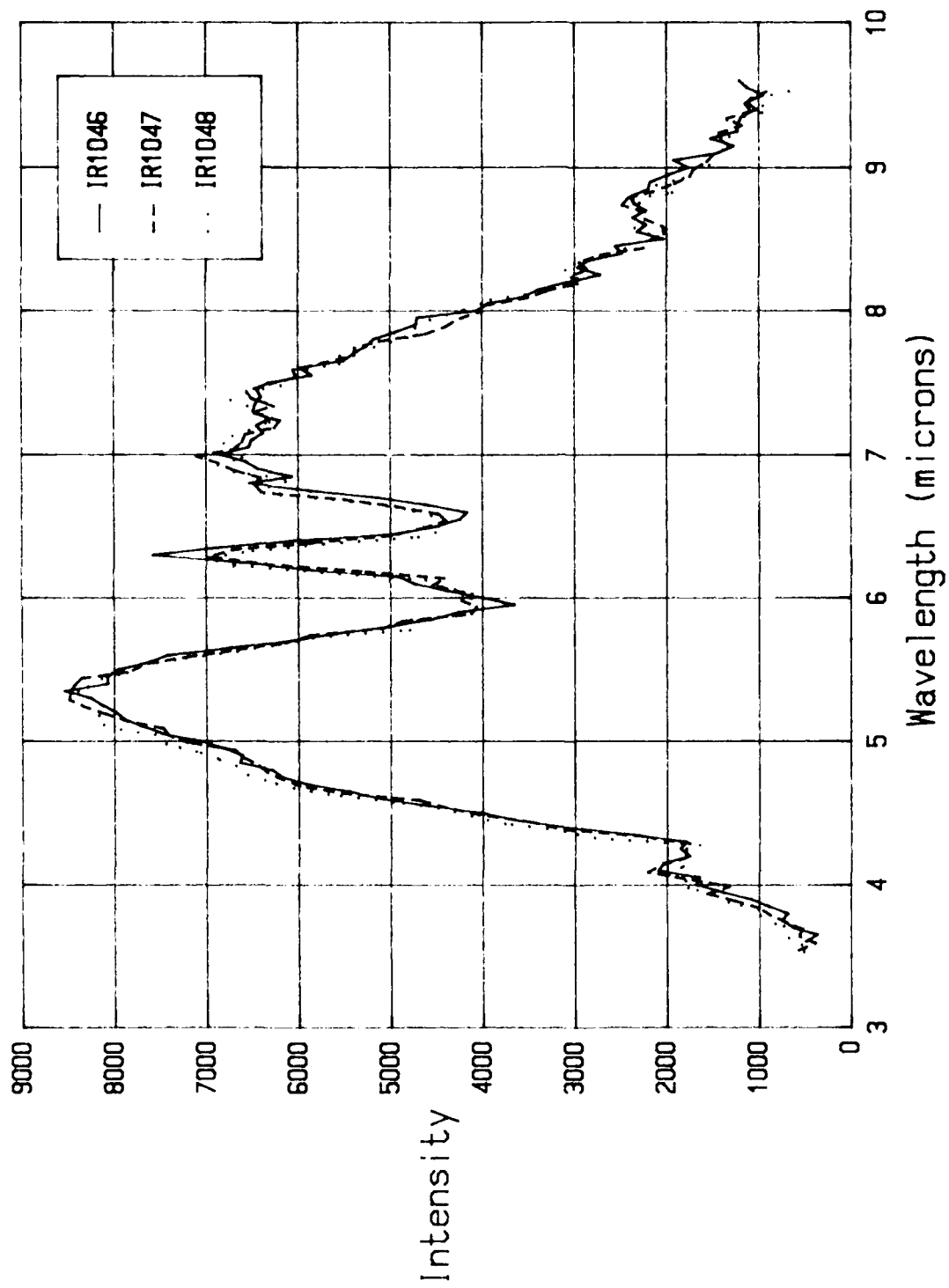


Figure 30. Effects of rapid irradiation on irradiated wet air.

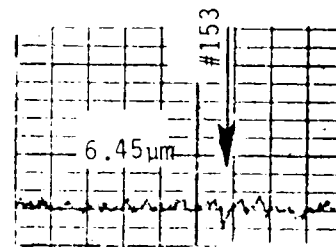
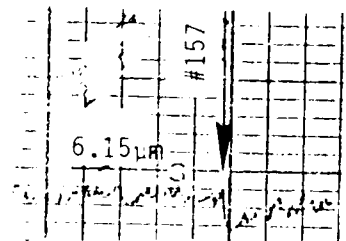
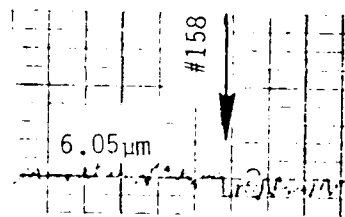
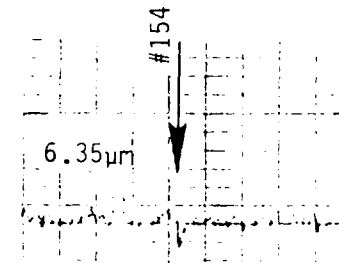
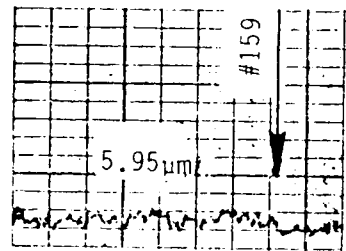
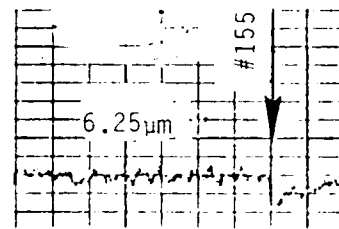
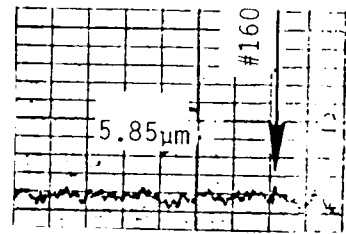


Figure 31. Transient absorption near 6.2 μm.

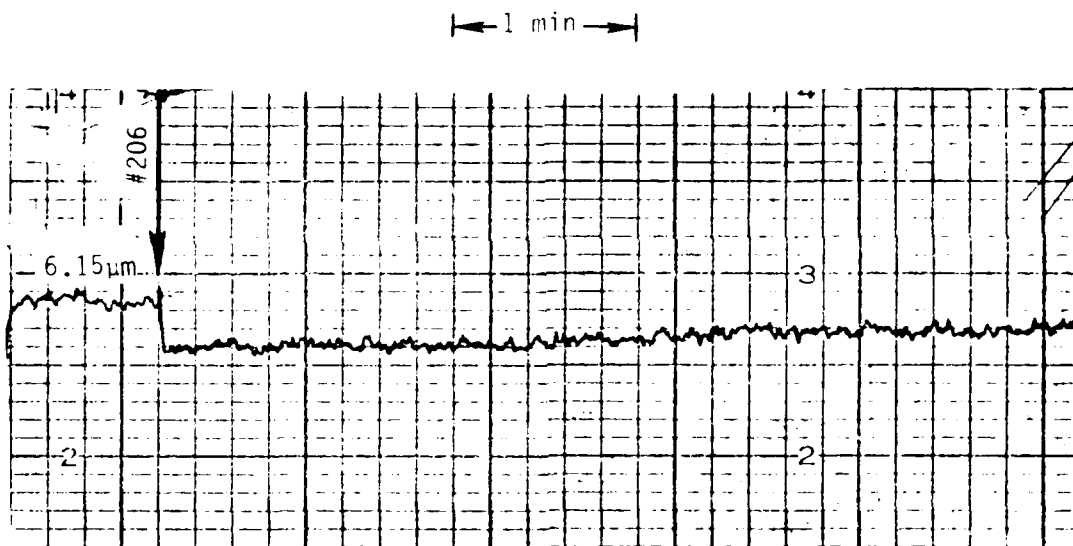


Figure 32. Recovery at 6.15 μm.

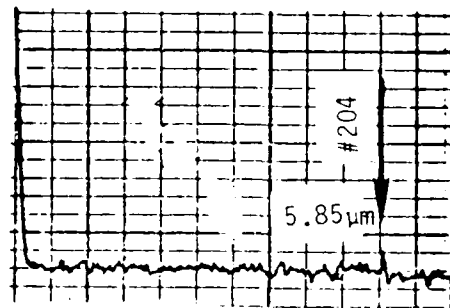
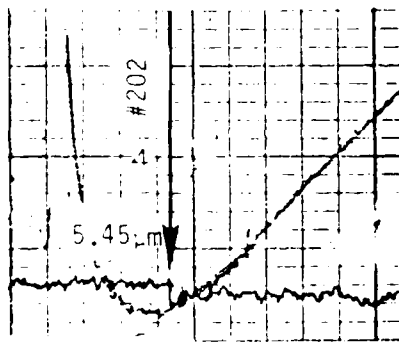
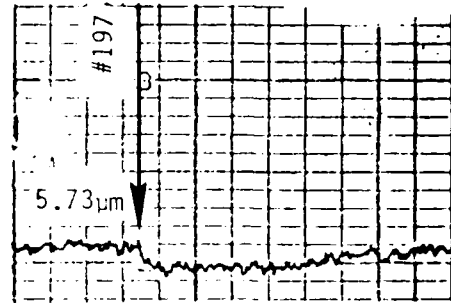
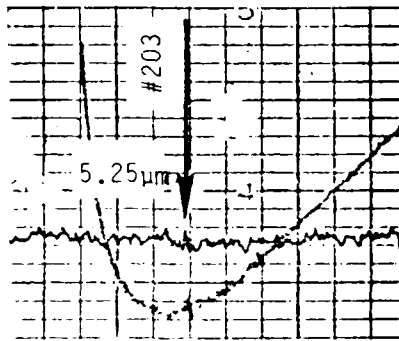


Figure 33. Transient absorption near 5.7 μm.

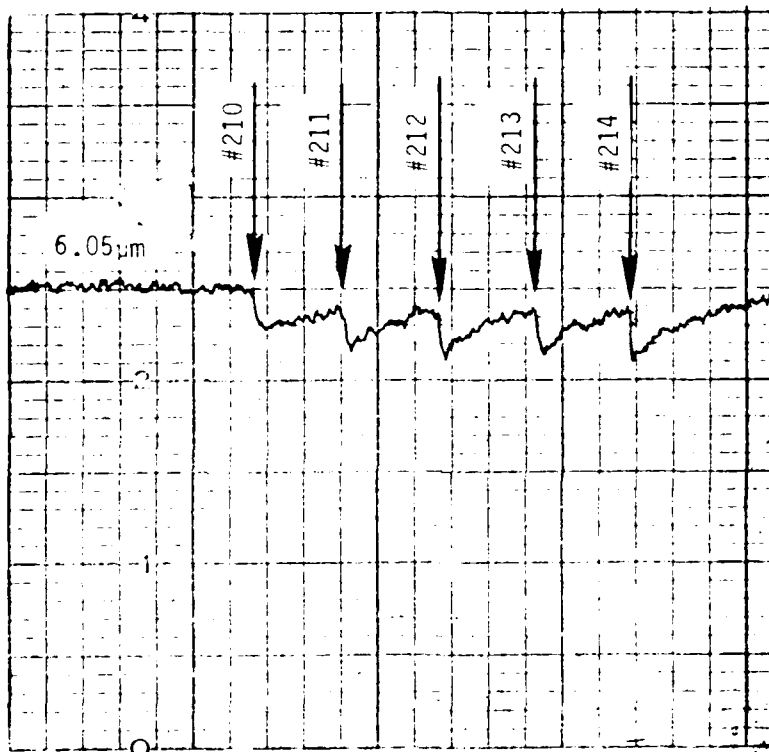


Figure 34. Relaxation at 6.15 m.

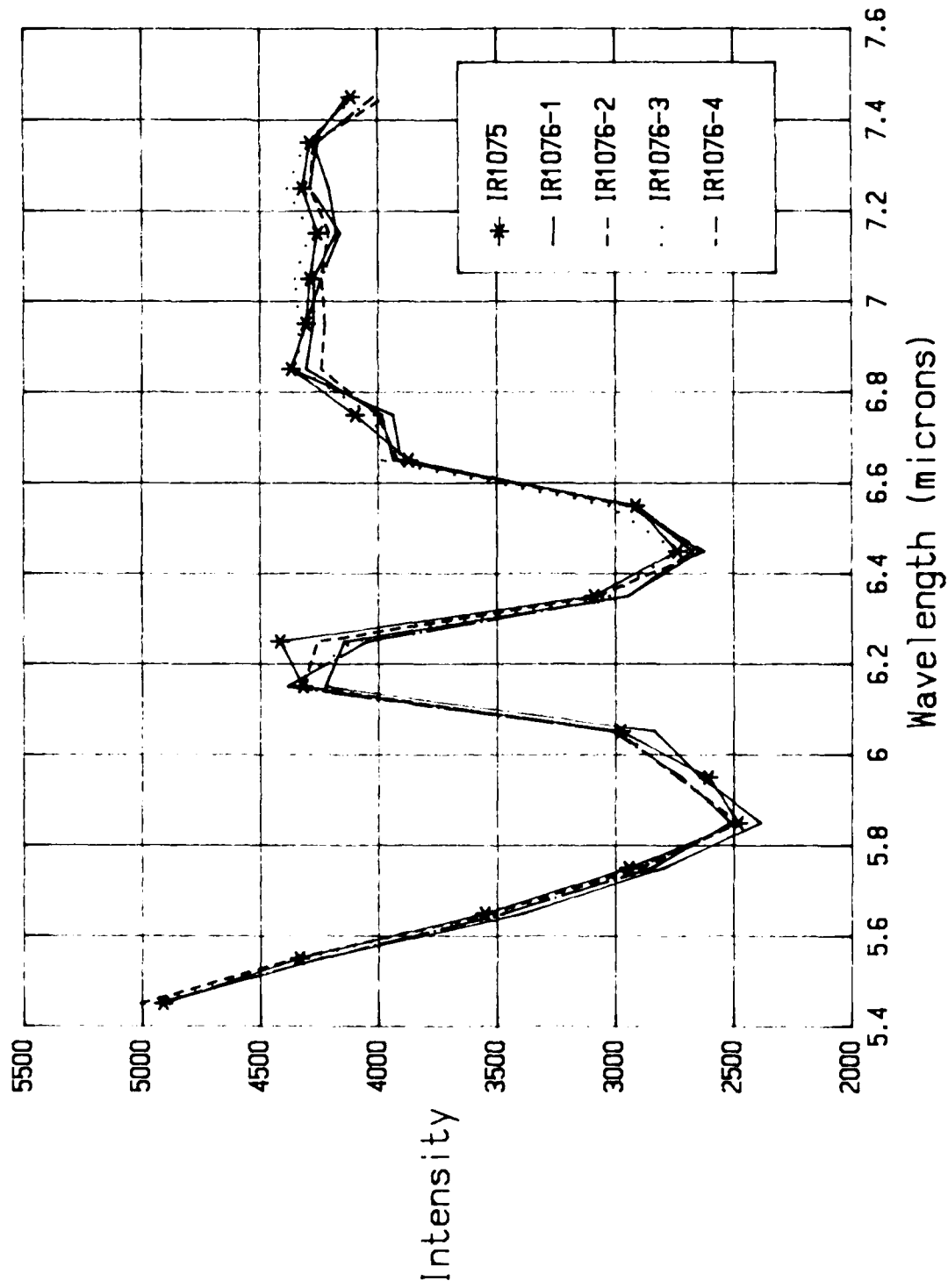


Figure 35. Transient absorption and recovery near 6.2 μm .

Spectrum IR1075 was taken before the ionization pulse. Successive cycles of spectrum IR1076 were taken starting immediately after a 0.5 Mrad pulse. Only near the 6.2 μm water window is the transient absorption detectable.

It was expected that nitric acid would be formed in wet air by ionizing radiation. Strong absorption bands in nitric acid are reported around 5.85 μm and 7.5 μm . However, these were not observed in our measurements with nitric acid deliberately added to the air sample. There are the possibilities that the lines were absent because the nitric acid absorbed on the walls of the sample chamber, or because extra hydration of the molecules changed their characteristic absorption frequencies.

The IR absorption measurements on irradiated wet air clearly showed a long-term buildup of absorption in the 6.7 μm to 7.4 μm range and a shorter-lived (8 minute decay) absorption near 6.2 μm , and a shorter-lived absorption near 5.7 μm . None of these wavelengths correlate well with the expected nitric-acid absorption bands.

The appearance of the 6.2 μm absorption at the window in the water absorption bands, and the suggestion that the water absorption peaks become less attenuating while the 6.2 μm absorption increases, suggests that this transient might be due not to a new absorption species, but due to some modification in the water absorption. The most obvious perturbation would be the effect of radiation-induced temperature rises on the water absorption (e.g., by Doppler broadening of the water absorption lines). However, it is unlikely that this explanation is credible. The gas sample chamber was constructed of aluminum and it was bolted onto the massive structure of the Excitron electron source. Clearly, this structure cannot have its temperature changed significantly by the beam and the effective relaxation time within the aluminum structure is very short compared to the observed lifetimes of the transient IR absorption. There remains the possibility that

the gas inside the chamber required some time to equilibrate in temperature with the aluminum wall. The lower limit to the relaxation time can be estimated by using the thermal diffusivity of air, which is approximately $0.19 \text{ cm}^2/\text{s}$ at room temperature. Thermal diffusion from the center of the chamber to the walls, a distance of 3.5 cm, will take place by conduction within approximately 50 s. Actually, it will take place much faster by convection. Therefore, while it is possible that the very short-lived transients seen in dry air could be influenced by thermal effects, the longer lived effects in wet air - especially the changes in the vicinity of $6.2 \mu\text{m}$ - cannot be explained by thermal effects. If the water absorption is affected by the irradiation, it must be a chemical or physical effect; not a thermal one.

Whatever changes are imposed on the gas sample by the irradiation, it is possible that absorption of the new species on the sample chamber walls will remove them. The time scale for this to occur can be estimated from the diffusion coefficient for gases in air: 0.1 to $0.2 \text{ cm}^2/\text{s}$ for typical gases (e.g., water vapor, carbon dioxide). This process also results in an effective relaxation time of ≈ 1 minute, divided by an effective sticking coefficient. The observed relaxation times can be consistent with reasonable values of sticking coefficients.

As in the dry-air experiments, the wet-air data clearly exhibit transient IR absorption lines. The fact that the absorption is measurable even with a single ionization pulse depositing only 0.5 Mrad of ionization energy implies that the effective absorption coefficient must be large; i.e., comparable to the stronger absorption bands in NO_2 and HNO_3 .

While these data cannot unambiguously identify the processes that occur in air in the aftermath of intense ionization events, they demonstrate that:

1. There are processes occurring on time scales from seconds to many minutes resulting in new chemical species.
2. IR absorption measurements can be used to follow these reactions.
3. Additional work is required to identify the chemical species responsible for the observed IR absorption bands.

SECTION 8
 μ/α DATA

In Section 3 of this report it was shown that the ratio of the electron mobility (μ) to the attachment rate (α) is proportional to the ion chamber current density, J_e and inversely proportional to the electric field, E and the dose rate \dot{D} . That is,

$$\frac{\mu}{\alpha} \propto \frac{J_e}{E \dot{D}}$$

Further, the grid voltage, V_g is directly proportional to the electric field, E (neglecting the ion boundary layer). The true grid voltage is obtained from the measured grid voltage, V_0 by taking into account the 10 K Ω limiting resistors between grid and scope. Figure 36 illustrates the effect of the 10 K Ω resistor and the scope 50 Ω to ground. The true grid voltage is then given by:

$$V_g = 200 V_0 \tag{26}$$

The electric field is then $E = V_g/d$ where d is the grid-to-ground spacing (0.5 cm).

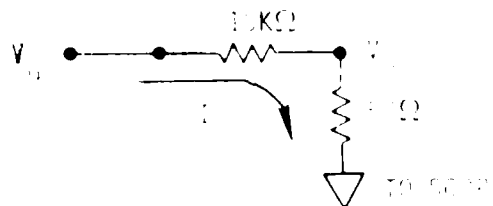


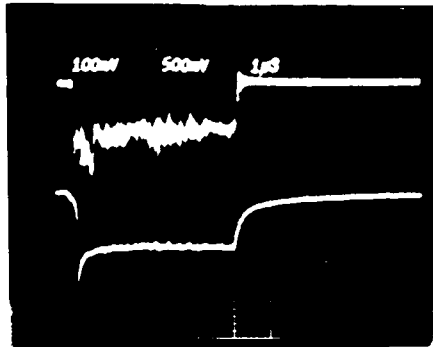
Figure 36. Effect of 10 K Ω resistor on grid.

In Section 5, it was shown that the dose rate, \dot{D} , is proportional to the Faraday cup current, I_{FR} , where $I_{FR} = V_{FR}/R_F$. Since the ion chamber current density is proportional to the ion chamber current it follows that

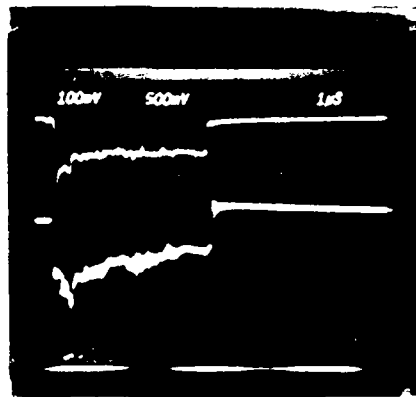
$$\frac{\mu}{\alpha} \propto \frac{I_I}{V_G V_{FR}}$$

Since the geometry of the collimator, ion chamber and Faraday cup and large amount of electron beam scattering made it difficult to measure accurately the dose rate and area of the electron beam, the ion chamber was calibrated by assuming the μ/α value for moist lightly irradiated air from other experimental data. Figures 37, 38 and 39 present samples of the oscilloscope photos for the moist air shots. Table 1 summarizes the measurements from a number of shots throughout the experiment series. Some data are shown both early and late in the 4 μ s irradiation pulse. The average and standard deviation of the measurements early in the pulse is 0.95 ± 0.12 relative units, whereas in the same units the measurements toward the end of the pulses yield 1.01 ± 0.16 . The spread is slightly larger in the late measurements, because the dose rate decreases during the pulse, as shown in Figure 38. These two values are indistinguishable from each other and are the same within an uncertainty of 15%. These measurements were all taken with a grid voltage between 145 and 160 V, i.e. with an applied field between 290 and 320 V/cm. For this range of fields and for 2.2% water vapor, the previously measured ratio μ/α equals 1.6×10^{-5} cm²/V (Ref.13). Therefore, we have used the ratio between this experimental value and our relative units to normalize all the other data.

The results of measurements in heavily irradiated moist air are summarized in Table 2. An example of these data, this one with an unusually long Excitron pulse, is shown in Figure 40. Within the uncertainty of the measurements there is no indication of a change in μ/α as a function of accumulated dose up to 33 Mrad.

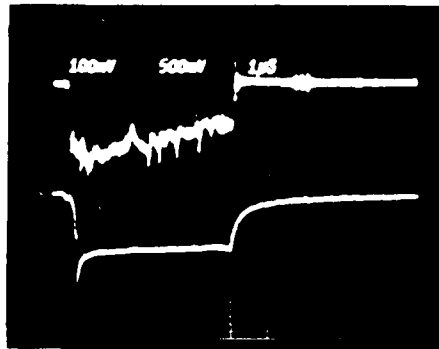


Upper: 0.1 V/div. Rear Faraday cup voltage.
 Lower: 100 V/div. Grid voltage.

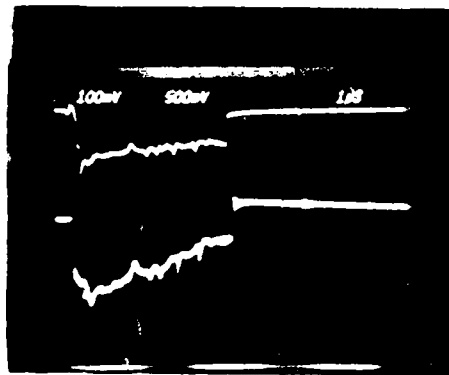


Upper: 20 mA/div. Ion chamber current.
 Lower: 0.5 V/div. Front Faraday cup voltage.

Figure 37. Grid voltage, Faraday cup voltage and ion chamber current for shot #210.

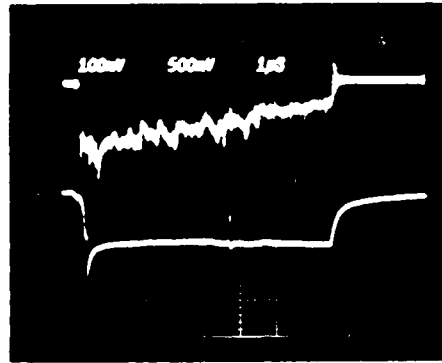


Upper: 0.1 V/div. Rear Faraday cup voltage.
 Lower: 100 V/div. Grid voltage.

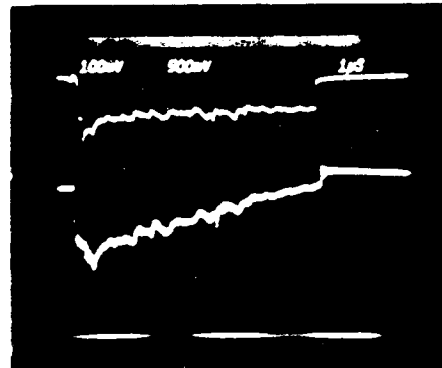


Upper: 10 mA/div. Ion chamber current.
 Lower: 0.5 V/div. Front Faraday cup voltage.

Figure 38. Grid voltage, Faraday cup voltage and ion chamber current for shot #214.



Upper: 0.1 V/div. Rear Faraday cup voltage.
 Lower: 0.5 V/div. Grid voltage.



Upper: 20 mA/div. Ion chamber current.
 Lower: 0.5 V/div. Front Faraday cup voltage.

Figure 4. Grid voltage, Faraday cup voltage and ion chamber current (Exhibit #199).

Table 1. Conductivity in unirradiated wet air ($\approx 2.2\% \text{ H}_2\text{O}$).

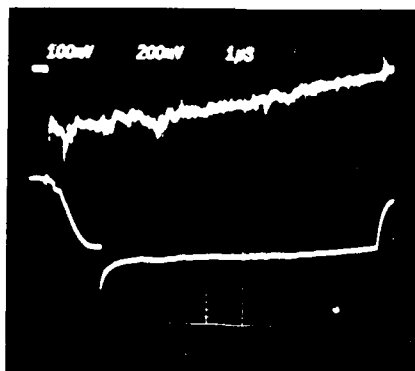
<u>Shot #</u>		<u>V_g</u>	<u>V_{FR}</u>	<u>I</u>	<u>(μ/α) Relative</u>
84	late	160	0.12	0.018	0.94
149	late	160	0.20	0.031	0.97
199	early	145	0.16	0.024	1.03
	late	145	0.07	0.013	1.28
210	early	160	0.15	0.024	1.00
	late	150	0.13	0.017	0.87
214	early	160	0.20	0.026	0.81
	late	150	0.11	0.016	0.97

Average Early: 0.95 ± 0.12

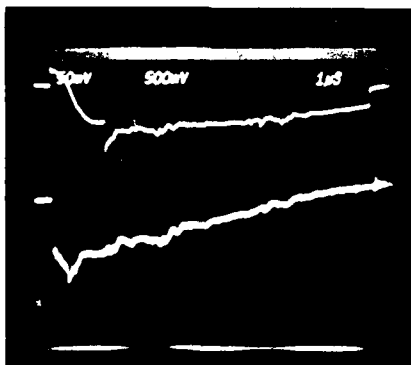
Average Late. 1.01 ± 1.6

Table 2. μ/α in irradiated wet air ($\approx 2.2\% \text{ H}_2\text{O}$).

<u>Shot #</u>	<u>Dose (Mrad)</u>	<u>V_g</u>	<u>V_{FR}</u>	<u>I</u>	<u>(μ/α) ($10^{-5} \text{ cm}^2/\text{V}$)</u>
108	16	160	0.14	0.021	1.57
135	33	150	0.12	0.017	1.57
160	7	160	0.30	0.040	1.39
205	6	140	0.15	0.022	1.75
207	7	90	0.13	0.0125	1.79
208	7	230	0.16	0.042	1.90
209	8	250	0.16	0.046	1.92



Upper: 0.1 V/div. Rear Faraday cup voltage.
 Lower: 0.5 V/div. Grid voltage.



Upper: 10 mA/div. Ion chamber current.
 Lower: 0.5 V/div. Front Faraday cup voltage.

Figure 40. Grid voltage, Faraday cup voltage and ion chamber current for shot #207.

Measurements of μ/α in dry air are summarized in Table 3. Examples of the oscilloscope data are presented in Figures 41 and 42. The data early in the pulse average to $2.62 \pm 0.26 \text{ cm}^2/\text{V}$; the data from the ends of the pulses average $2.82 \pm 0.12 \text{ cm}^2/\text{V}$. These values are not significantly different. The effect of irradiation up to 9 Mrad is also not detectable within the estimated accuracy of 15%.

Measurements of the effect on μ/α of the deliberate addition of contaminants are summarized in Table 4. Sample oscilloscope photos are presented in Figures 43-51. The data in Table 4 clearly show a decrease in μ/α due to the addition of NO_2 to dry air, with a stronger effect at lower electric fields (e.g. 120-140 V/cm). There is no appreciable effect of adding NO_2 to moist air. It must be remembered that the effect of NO_2 on the dry air IR absorption was also observed, but no effect was seen in moist air. One possible explanation is that the water induced the NO_2 to be adsorbed on the walls of the sample chamber, in which case it could not have affected μ/α either.

While the effect of adding nitric acid to air was not observed by IR absorption, there is a marked effect on μ/α as shown in Table 4. The estimate of 1500 ppm concentration is based strictly on the amount added to the air sample. The actual concentration could have been much less due to adsorption on the sample chamber walls.

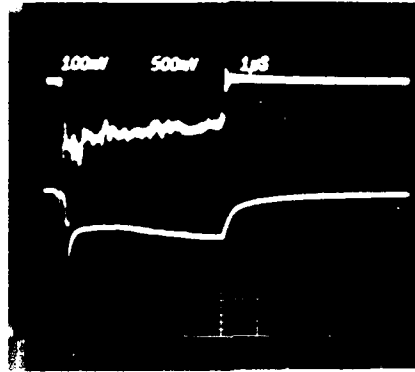
It was concluded from the data in Table 2 that doses up to 30 Mrad decreased μ/α by less than 15%. The addition of no more than 1500 ppm HNO_3 to moist air decreased μ/α by approximately 20% at corresponding values of the electric field. Therefore, we can conclude marginally that the amount of HNO_3 formed in these exposures and not adsorbed on the walls was less than 0.5 molecule per ion.

Table 3. μ/α in dry air.

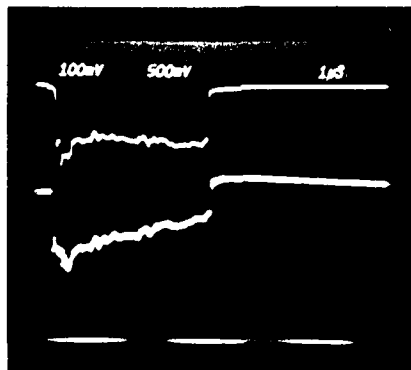
<u>Shot #</u>		<u>Dose</u>	<u>V_g</u>	<u>V_{FR}</u>	<u>I</u>	<u>(μ/α) (10^{-5} cm²/V)</u>
215	early	0.05	110	0.17	0.028	2.49
	late	0.5	125	0.13	0.027	2.79
219	early	2.0	110	0.19	0.034	2.72
	late	2.5	135	0.12	0.028	2.89
168	early	1.0	125	0.165	0.030	2.42
	late	1.5	125	0.10	0.020	2.67
182	early	8.0	125	0.165	0.030	2.42
183	early	8.5	125	0.15	0.034	3.03
	late	9.0	135	0.105	0.025	2.94

Average Early: 2.62 ± 0.26

Average Late: 2.82 ± 0.12

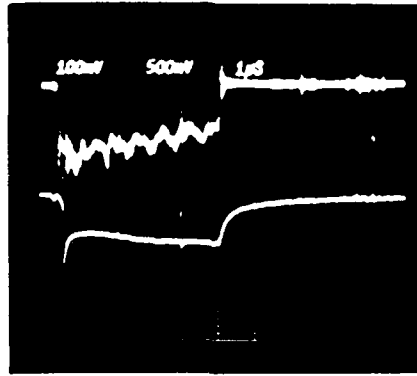


Upper: 0.1 V/div. Rear Faraday cup voltage.
 Lower: 100 V/div. Grid voltage.

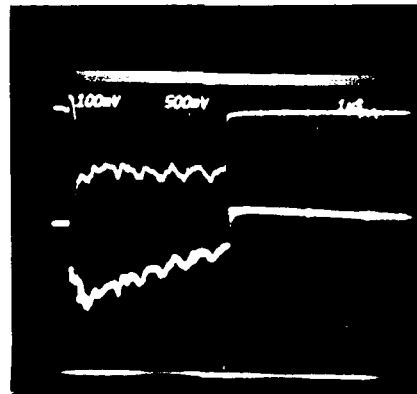


Upper: 20 mA/div. Ion chamber current.
 Lower: 0.5 V/div. Front Faraday cup voltage.

Figure 41. Grid voltage, Faraday cup voltage and ion chamber current for shot #215.



Upper: 0.1 V/div. Rear Faraday cup voltage.
 Lower: 100 V/div. Grid voltage.

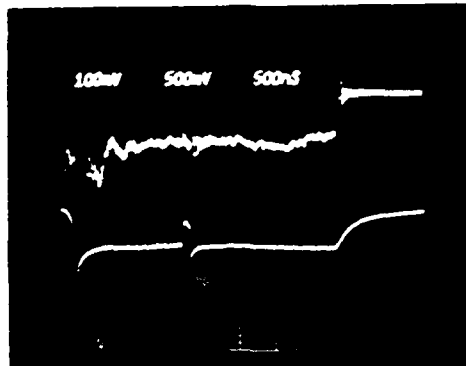


Upper: 20 mA/div. Ion chamber current.
 Lower: 0.5 V/div. Front Faraday cup voltage.

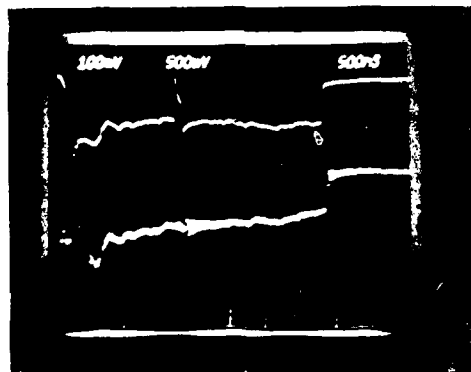
Figure 42. Grid voltage, Faraday cup voltage and ion chamber current for shot #219.

Table 4. Effect of contaminants on μ/α .

Shot #		V_g	V_{FR}	I	μ/α (10^{-5} cm ² /V)	
					Meas.	W/O Contamination
<u>440 ppm NO₂ in dry air:</u>						
223	early	70	0.135	0.015	2.66	4.0
	late	60	0.13	0.014	2.99	
221	early	115	0.13	0.024	2.67	3.6
	late	120	0.11	0.020	2.54	
222	early	210	0.135	0.048	2.82	3.4
	late	240	0.115	0.043	2.61	
<u>400 ppm NO₂ in wet air:</u>						
225	early	155	0.135	0.020	1.60	1.62
	late	145	0.11	0.013	1.37	
227	early	225	0.16	0.032	1.48	1.50
	late	255	0.13	0.032	1.60	
228	early	220	0.18	0.030	1.26	1.50
	late	250	0.125	0.030	1.60	
<u>"1500 ppm" HNO₃ in wet air:</u>						
232	early	120	0.14	0.011	1.10	1.70
	late	92	0.12	0.007	1.07	
230	early	160	0.14	0.020	1.49	1.57
	late	145	0.13	0.014	1.24	
229	early	225	0.175	0.030	1.27	1.50
	late	240	0.13	0.025	1.34	

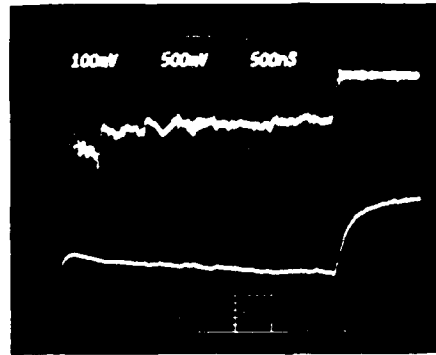


Upper: 0.1 V/div. Rear Faraday cup voltage.
 Lower: 0.5 V/div. Grid voltage.

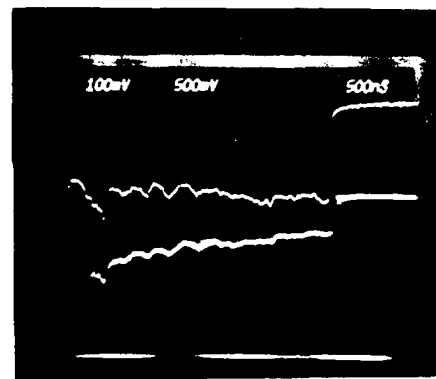


Upper: 20 mA/div. Ion chamber current.
 Lower: 0.5 V/div. Front Faraday cup voltage.

Figure 43. Grid voltage, Faraday cup voltage and ion chamber current for shot #221.

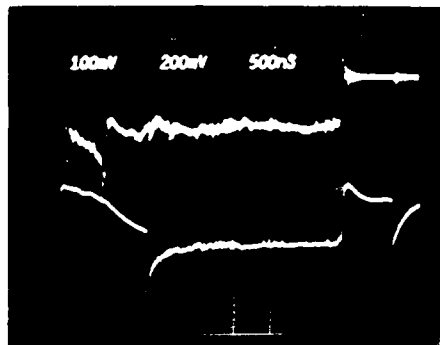


Upper: 0.1 V/div. Rear Faraday cup voltage.
 Lower: 0.5 V/div. Grid voltage.



Upper: 20 mA/div. Ion chamber current.
 Lower: 0.5 V/div. Front Faraday cup voltage.

Figure 44. Grid voltage, Faraday cup voltage and ion chamber current for shot #222.

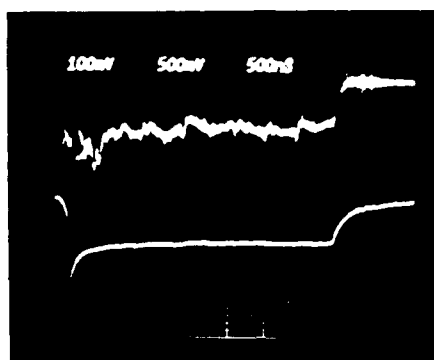


Upper: 0.1 V/div. Rear Faraday cup voltage.
 Lower: 0.2 V/div. Grid voltage.

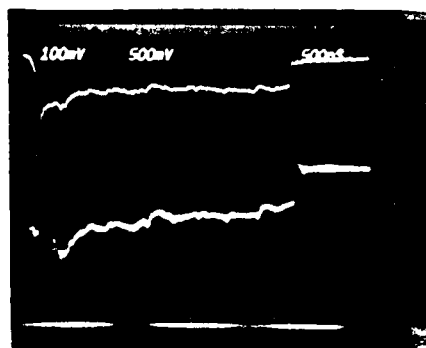


Upper: 10 mA/div. Ion chamber current.
 Lower: 0.5 V/div. Front Faraday cup voltage.

Figure 45. Grid voltage, Faraday cup voltage and ion chamber current for shot #223.

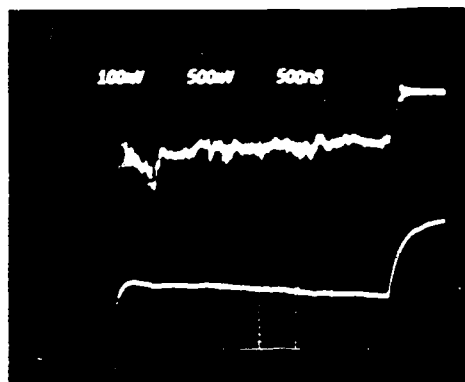


Upper: 0.1 V/div. Rear Faraday cup voltage.
 Lower: 0.5 V/div. Grid voltage.

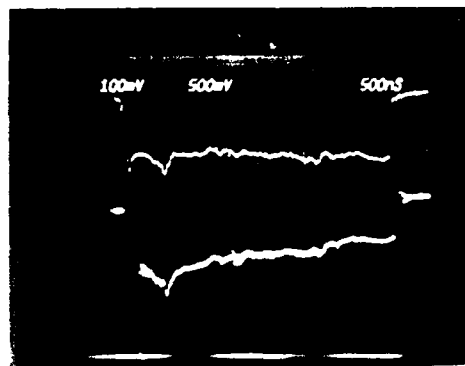


Upper: 20 mA/div. Ion chamber current.
 Lower: 0.5 V/div. Front Faraday cup voltage.

Figure 46. Grid voltage, Faraday cup voltage and ion chamber current for shot #225.



Upper: 0.1 V/div. Rear Faraday cup voltage.
 Lower: 0.5 V/div. Grid voltage.

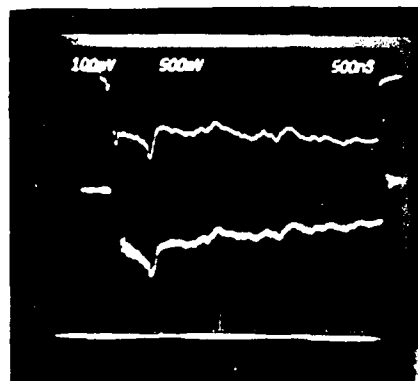


Upper: 20 mA/div. Ion chamber current.
 Lower: 0.5 V/div. Front Faraday cup voltage.

Figure 47. Grid voltage, Faraday cup voltage and ion chamber current for shot #227.

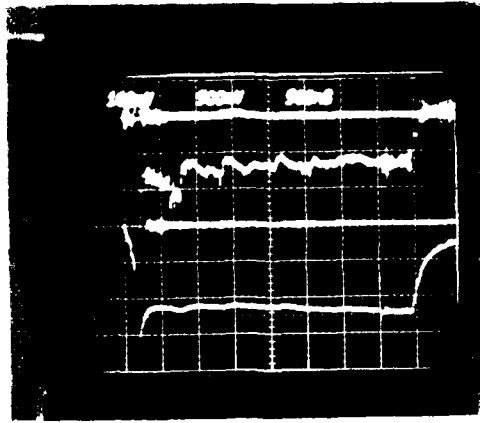


Upper: 0.1 V/div. Rear Faraday cup voltage.
 Lower: 0.5 V/div. Grid voltage.

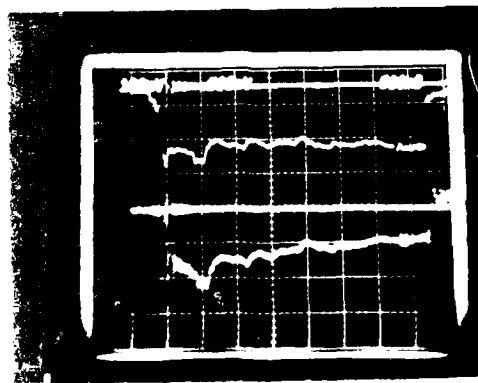


Upper: 20 mA/div. Ion chamber current.
 Lower: 0.5 V/div. Front Faraday cup voltage.

Figure 48. Grid voltage, Faraday cup voltage and ion chamber current for shot #228.



Upper: 0.1 V/div. Rear Faraday cup voltage.
 Lower: 0.5 V/div. Grid voltage.



Upper: 0.1 V/div. Rear Faraday cup voltage.
 Lower: 0.5 V/div. Grid voltage.

Figure 4.1. Grid voltage and
 Rear Faraday cup voltage.

NO-A190 045

EFFECTS OF IONIZATION-INDUCED SMOG ON AIR CHEMISTRY(U)
MISSION RESEARCH CORP SAN DIEGO CA V A VAN LINT ET AL
30 JAN 87 MRC/SD-R-183 DMR-TR-87-27 DMR001-81-C-0151

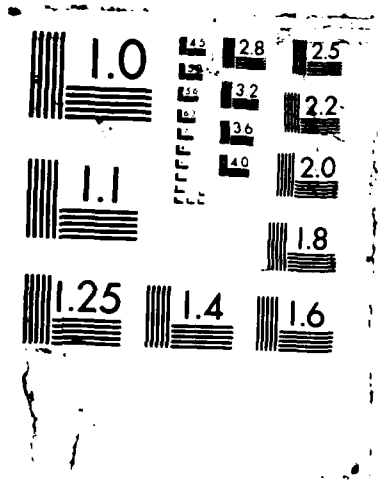
2/2

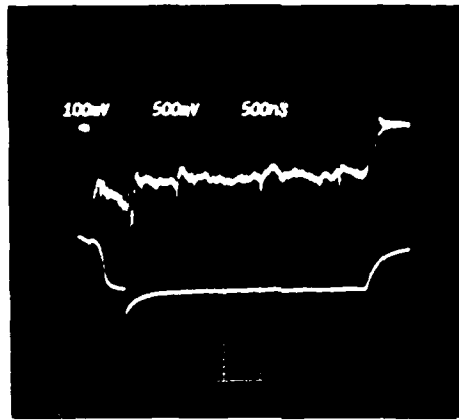
UNCLASSIFIED

F/G 4/1

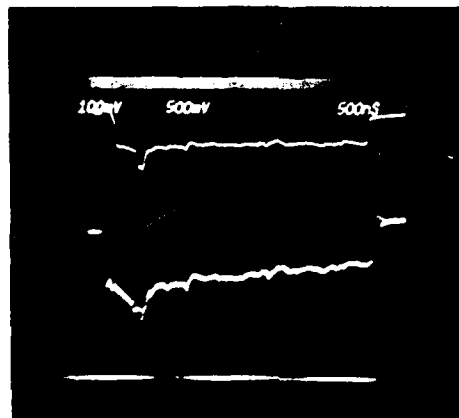
NL





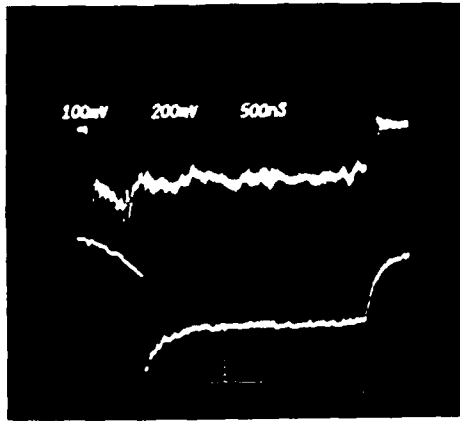


Upper: 0.1 V/div. Rear Faraday cup voltage.
 Lower: 0.5 V/div. Grid voltage.

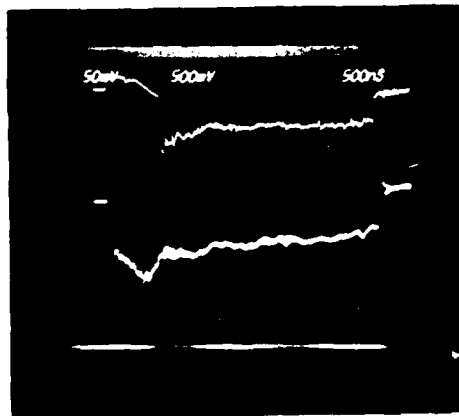


Upper: 20 mA/div. Ion chamber current.
 Lower: 0.5 V/div. Front Faraday cup voltage.

Figure 50. Grid voltage, Faraday cup voltage and ion chamber current for shot #230.



Upper: 0.1 V/div. Rear Faraday cup voltage.
 Lower: 0.2 V/div. Grid voltage.



Upper: 10 mA/div. Ion chamber current.
 Lower: 0.5 V/div. Front Faraday cup voltage.

Figure 51. Grid voltage, Faraday cup voltage and ion chamber current for shot #232.

SECTION 9 CONCLUSIONS

This experiment to measure the effects of ionization-induced smog was beset with difficulties, particularly in finding a suitable source of ionizing radiation. The source that could produce a sufficient dose in a single pulse (i.e. AURORA) had too short a pulse. Other sources that might produce the required dose in a single 100 μ s pulse were considered too risky. The measurements were finally performed by using multiple pulses at the Maxwell Laboratories Excitron electron source. Since the source was not able to operate reliably at its maximum energy and pulse length, the dose per pulse was lower than planned by a factor of 2 to 3.

Nevertheless, effects of even a single Excitron pulse on the infra-red absorption spectra of dry and moist air were observed. These effects are apparently not due to the expected smog species, especially nitric acid, because the absorption lines are not at the wavelengths identified for nitric acid and the apparent absorption cross sections are larger by approximately a factor of ten. These are likely to be indicators of other metastable species in irradiated air.

Within an accuracy of 15% no effect of irradiation on μ/α was detected in either dry or moist air at doses up to 33 Mrad in moist air, and 9 Mrad in dry air. The addition of 1500 ppm HNO_3 to moist air produced a decrease in μ/α of approximately 20% at an electric field of 300 V/cm. Comparing this measurement with the lack of effect by irradiation, we conclude that less than 0.5 molecule of HNO_3 was left in the gas per ion formed.

SECTION 10
LIST OF REFERENCES

1. Scheibe, M., "The Increased Attachment Due to Ionization-Induced Smog in EMP Environments," Defense Nuclear Agency, DNA5077F (October 1979).
2. Chervenak, J.C. and V.A.J. van Lint "Measurement of the Electrical Properties of Highly Dosed Air in the Millisecond Regime," Defense Nuclear Agency, DNA 5492T, October 1980.
3. Frese, M.H., J.L. Gilbert, and C.L. Longmire, "Nuclear Lightning, I. Currents Carried by the Discharge," AMRC-R-239, Mission Research Corporation, Albuquerque, NM, September 1980.
4. Gardner, R., C.L. Longmire, J.L. Gilbert, and M.H. Frese, "Nuclear Lightning, VII. Growth Rate of Discharge," AFWL-TR-81-192 (V2), Air Force Weapons Laboratory, February 1982.
5. Scheibe, M., private communication.
6. Chervenak, J.C. and V.A.J. van Lint, "Ion-Ion Recombination Rate in Air," Defense Nuclear Agency, DNA-TR-81-83, February 1982.
7. van Lint, V.A.J. and J.G. Chervenak, "Electron-Ion Recombination in Air at EMP Fields," Defense Nuclear Agency, DNA-TR-85-202, June 1985.
8. van Lint, V.A.J. and J.W. Erler, "Nuclear Induced Lightning Excitron Experiment," unpublished.
9. Sadtler Research Laboratories, 1979.
10. Park, J.H., et. al, "Atlas of Absorption Lines from 0 to 17900 cm^{-1} ," NASA Reference Publication 1084, December 1981.
11. Rathman, L.S., et. al., "AFGL Trace Gas Compilation: 1982 Version," Applied Optics, Vol. 22, June 1983.
12. Murcray, David G., and Goldman, Aaron, CRC Handbook of High Resolution Infrared Laboratory Spectra of Atmospheric Interest, CRC Press, Boca Raton, Florida, 1981.
13. van Lint, V.A.J., "Electron Mobility and Attachment in Dry and Moist Air," Defense Nuclear Agency, DNA 6109T, April 1982.

APPENDIX
CORRECTIONS FOR SCATTERING AND ELECTRON BEAM DIVERGENCE

The angle of divergence of a collimated beam of electrons due to multiple collisions is given by

$$\langle \theta^2 \rangle = 4\pi N z(z+1)e_0^4 \frac{d}{(pv)^2} \ln \left[4\pi Z^4 \frac{3}{\alpha} Nd \left(\frac{t}{m_0 v} \right)^2 \right] \quad (\text{Ref. 1})$$

where e_0 , m_0 , p , v , is the charge, mass momentum and velocity of the electrons respectively

Z is the atomic number of the target

N is the atomic density of the target

d is the thickness of the scatterer (in gm/cm²)

and α is the fine structure constant (=1/137)

The anode of the Excitron is a 3 mil aluminum foil, with mass density of 0.02 gm/cm². The energy loss of 250 keV electrons is approximately 2.8 MeV·cm²/gm. Inserting these values into the above equation yields a bulk scattering angle of $\theta_{rms} = 0.85$ rad.

In effect, the electrons are heavily scattered by the foil and the 0.01 gm/cm² of air, so that the beam size at the back wall of the main sample chamber is expected to be larger by approximately twice the chamber thickness compared with the incident beams.

Measurements of the effect of air pressure on the Faraday cup reading are illustrated in Figure 52. Decreasing the pressure to 12% of an atmosphere increases the electron beam current by a factor of 1.5. Since



Pressure 760T

Pressure 212T

Pressure 88T

Figure 52. Effect of pressure (lower trace = Faraday cup).

the scattering angle in the air is estimated to be approximately half as great as in the Al foil, it is reasonable to estimate the dose at the entrance foil to be greater than in the Faraday cup by a factor of $(1.5)^3 = 3.4$. For a typical shot, the Faraday cup read 0.7 V, corresponding to a current density of 0.3 A/cm^2 . The estimated incident current density is then 1 A/cm^2 , in good agreement with measurements made by Maxwell Labs personnel at the exit foil in the absence of our sample chamber.

REFERENCE

1. Segre, E. Experimental Nuclear Physics, Vol. 1, p. 285, Wiley (1953).

DISTRIBUTION LIST

DEPARTMENT OF DEFENSE

ARMED FORCES STAFF COLLEGE
ATTN: LIBRARY

ASSISTANT SECRETARY OF DEFENSE
CMD. CONTROL, COMMUNICATIONS & INTEL
ATTN: DASD(C3)
ATTN: DASD(I)
ATTN: DASD(I)
ATTN: DASD(P&R)

ASSISTANT TO THE SECRETARY OF DEFENSE
ATTN: C31
ATTN: EXECUTIVE ASSISTANT

DEFENSE COMMUNICATIONS AGENCY
ATTN: COMMANDER

DEFENSE COMMUNICATIONS ENGINEER CENTER
ATTN: CODE R123 (TECH LIB)
ATTN: CODE R400

DEFENSE INTELLIGENCE AGENCY
ATTN: DT(SCI-TECH INTELL)
ATTN: RTS-2A (TECH LIB)
ATTN: RTS-2B

DEFENSE NUCLEAR AGENCY
ATTN: DFRA
ATTN: OPNA
ATTN: OPNS
ATTN: RAAE
ATTN: RAAE
ATTN: RAEV
4 CYS ATTN: TITL

DEFENSE TECHNICAL INFORMATION CENTER
12 CYS ATTN: DD

DIRECTOR
ATTN: DOCUMENT CONTROL

DNA PACOM LIAISON OFFICE
ATTN: DNALO

JOINT CHIEFS OF STAFF
ATTN: INFORMATION SYSTEMS DIVISION
ATTN: NUCLEAR CONTINGENCY BRANCH
ATTN: STRATEGIC OPERATIONS DIVISION
ATTN: NUCLEAR & CHEMICAL DIV
ATTN: JAD

JOINT STRAT TGT PLANNING STAFF

ATTN: JK (ATTN: DNA REP)
ATTN: JKCS
ATTN: JLWT (THREAT ANALYSIS)
ATTN: JPEP
ATTN: JPPFA
ATTN: JPPFD
ATTN: JPSS
ATTN: JPTM

JOINT TACTICAL C3 AGENCY

ATTN: C3A-ARJS
ATTN: C3A-SES

LAWRENCE LIVERMORE NATIONAL LABORATORY

ATTN: DNA-LL

NATIONAL COMMUNICATIONS SYSTEM

ATTN: NCS-TS

NATIONAL DEFENSE UNIVERSITY

ATTN: NWCO

NATIONAL SECURITY AGENCY

ATTN: CHIEF A GROUP
ATTN: Y253 (HILTON)

U S EUROPEAN COMMAND/ECC3S-CC

ATTN: ECC3S-CC

U S FORCES KOREA

ATTN: EACJ-PON-NO

U S NATIONAL MILITARY REPRESENTATIVE

ATTN: U S DOCUMENTS OFFICER

UNDER SECRETARY OF DEFENSE

ATTN: DEP UND SEC TAC WARFARE PROGS
ATTN: DEP UND SEC COM SYS
ATTN: DEP UND SEC C3I-STRAT/C2 SYS
ATTN: STRAT & SPACE SYS(OS)
ATTN: STRAT/THEAT NUC FOR F VAJDA

UNITED STATES SPACE COMMAND

ATTN: J5YX

DEPARTMENT OF THE ARMY

DEFENSE COMMUNICATIONS SYSTEMS
ATTN: DRCPM COM W D

DEPT CH OF STAFF FOR OPS & PLANS

ATTN: DAMO ODW

DNA-TR-87-27 (DL CONTINUED)

DEPT CH OF STAFF FOR RSCH DEV & ACQ
ATTN: DAMA-CSM-N

DEPARTMENT OF THE ARMY
ATTN: DAMO-TCV-A

HARRY DIAMOND LABORATORIES
ATTN: CHIEF DIV 10000

ATTN: SCHLD-NW-P
ATTN: SLCHD-NE-EB
ATTN: SLCHD-NW

2 CYS
ATTN: SLCHD-NW-E
ATTN: SLCHD-NW-EA
ATTN: SLCHD-NW-ED
ATTN: SLCHD-NW-EE
ATTN: SLCHD-NW-R
ATTN: SLCHD-NW-RA
ATTN: SLCHD-NW-RC
ATTN: G MERKEL
ATTN: R GILBERT
ATTN: G HUTTLIN
ATTN: SLCIS-IM-TL (TECH LIB)

RESEARCH & DEV CENTER
ATTN: DRCPM-ATC
ATTN: DRCPM-TDS-SD

U S ARMY ATMOSPHERIC SCIENCES LAB
ATTN: SLCAS-AS

U S ARMY BALLISTIC RESEARCH LAB
ATTN: SLCBR-SS-T (TECH LIB)
ATTN: SLCBR-VL

U S ARMY BELVOIR RD & E CTR
ATTN: STRBE-BT (TECH LIB) (VAULT)

U S ARMY COMB ARMS COMBAT DEV ACTY
ATTN: ATZL-CAC-A
ATTN: ATZL-CAN-I
ATTN: ATZL-CAP

U S ARMY COMD & GENERAL STAFF COLLEGE
ATTN: LIBRARY

U S ARMY ENGINEER DIV HUNTSVILLE
ATTN: HNDED-SY

U S ARMY INFORMATION SYS MNGT AGENCY
ATTN: CCM-AD-LB (LIBRARY)

U S ARMY MATERIEL SYS ANALYSIS ACTVY
ATTN: AMXSY-CR

U S ARMY MISSILE COMMAND
ATTN: AMSMI-SF

U S ARMY MISSILE COMMAND
ATTN: AMSMI-RD-GC-P

U S ARMY MISSILE COMMAND/AMSMI-RD-CS-R
ATTN: AMSMI-RD-CS-R (DOCS)

U S ARMY NUCLEAR & CHEMICAL AGENCY
ATTN: LIBRARY

U S ARMY STRATEGIC DEFENSE CMD
ATTN: J KAHLAS

U S ARMY STRATEGIC DEFENSE CMD
ATTN: DASD-H-SAV

U S ARMY STRATEGIC DEFENSE COMMAND
ATTN: ATC-R
ATTN: DASD-H-L

U S ARMY TEST AND EVALUATION COMD
ATTN: TECHNICAL LIBRARY SI-F

U S ARMY TRADOC SYS ANALYSIS ACTVY
ATTN: ATRC-TD

U S ARMY WAR COLLEGE
ATTN: LIBRARY

DEPARTMENT OF THE NAVY

NAVAL AIR SYSTEMS COMMAND
ATTN: AIR 350F
ATTN: AIR 5161

NAVAL OCEAN SYSTEMS CENTER
ATTN: CODE 9642 (TECH LIB)

NAVAL POSTGRADUATE SCHOOL
ATTN: CODE 1424 LIBRARY

NAVAL RESEARCH LABORATORY
ATTN: CODE 2627 (TECH LIB)

NAVAL SURFACE WEAPONS CENTER
ATTN: CODE R40
ATTN: CODE R43
ATTN: CODE 425

NAVAL SURFACE WEAPONS CENTER
ATTN: CODE H-21

NAVAL WEAPONS CENTER
ATTN: CODE 343 (FKA6A2) (TECH SVCS)

OFC OF THE DEPUTY CHIEF OF NAVAL OPS
ATTN: NOP 098(OFC RES-DEV-TEST/EVAL)
ATTN: NOP 506
ATTN: NOP 551
ATTN: NOP 94
ATTN: NOP 981N1
ATTN: OP 654(STRAT EVAL & ANAL BR)
ATTN: OP 981

DNA-TR-87-27 (DL CONTINUED)

SPACE & NAVAL WARFARE SYSTEMS CMD
ATTN: PME 117-21
ATTN: TECHNICAL LIBRARY

STRATEGIC SYSTEMS PROGRAM OFFICE (PM-1)
ATTN: NSP-L63 (TECH LIB)

THEATER NUCLEAR WARFARE PROGRAM OFC
ATTN: PMS 423

U S NAVAL FORCES, EUROPE
ATTN: N54

DEPARTMENT OF THE AIR FORCE

AERONAUTICAL SYSTEMS DIVISION
ATTN: ASD/ENACE
ATTN: ASD/ENES(P MARTH)

AF/INE
ATTN: INA

AIR FORCE COMMUNICATIONS COMMAND
ATTN: C JAROCKI

AIR FORCE CTR FOR STUDIES & ANALYSIS
ATTN: AFCSA/SAMI (R GRIFFIN)

AIR FORCE INSTITUTE OF TECHNOLOGY/EN
ATTN: LIBRARY/AFIT/LDEE

AIR FORCE SPACE COMMAND
ATTN: LKA

AIR FORCE WEAPONS LABORATORY
ATTN: NT
ATTN: NTAA
ATTN: NTYC
ATTN: SUL

AIR UNIVERSITY LIBRARY
ATTN: AUL-LSE

BALLISTIC MISSILE OFFICE
ATTN: ENSN

DEPUTY CHIEF OF STAFF
ATTN: LEEEU

DEPUTY CHIEF OF STAFF/AF RDQM
ATTN: AF/RDQI

DEPUTY CHIEF OF STAFF/XOX
ATTN: AFXOXFM(PLNS FRC DEV MUN PLNS)

ELECTRONIC SYSTEMS DIVISION/SC
ATTN: SCS 1E

HEADQUARTERS U S AIR FORCES IN EUROPE/LG
ATTN: XPXF

ROME AIR DEVELOPMENT CENTER, AFSC
ATTN: TECHNICAL LIBRARY (DOVL)

SPACE COMMAND/DE
ATTN: DEE

SPACE DIVISION/IN
ATTN: IND

SPACE DIVISION/YA
ATTN: YAR

STRATEGIC AIR COMMAND/DEPR
ATTN: DEPR

STRATEGIC AIR COMMAND/INA
ATTN: INA

STRATEGIC AIR COMMAND/NRI-STINFO
ATTN: NRI-STINFO

STRATEGIC AIR COMMAND/SIP
ATTN: SAC/SCPT

STRATEGIC AIR COMMAND/XPFC
ATTN: XPFS

STRATEGIC AIR COMMAND/XPQ
ATTN: XPQ

TACTICAL AIR COMMAND/XPJ
ATTN: TAC/XPJ

U S RESEARCH & DEVELOPMENT COORD
ATTN: USRADCO

DEPARTMENT OF ENERGY

EMERGENCY ELECTRIC POWER ADM
ATTN: LIBRARY

LAWRENCE LIVERMORE NATIONAL LAB
ATTN: TECH INFO DEPT LIBRARY

LOS ALAMOS NATIONAL LABORATORY
ATTN: REPORT LIBRARY

SANDIA NATIONAL LABORATORIES
ATTN: TECH LIB 3141 (RPTS REC CLRK)

OTHER GOVERNMENT

CENTRAL INTELLIGENCE AGENCY
ATTN: OSR/SE/C
ATTN: OSR/SE/F
ATTN: OSWR/NED
ATTN: OSWR/STD/MTB

FEDERAL EMERGENCY MANAGEMENT AGENCY
ATTN: SL-EM

DNA-TR-87-27 (DL CONTINUED)

NATIONAL BUREAU OF STANDARDS
ATTN: 723.03

DEPARTMENT OF DEFENSE CONTRACTORS

AGBABIAN ASSOCIATES
ATTN: LIBRARY

ALLIED CORP
ATTN: DOCUMENT CONTROL

AT&T TECHNOLOGIES, INC
ATTN: W EDWARDS

BDM CORP
ATTN: CORPORATE LIB(UNCLAS ONLY)

BDM CORP
ATTN: LIBRARY

BOEING CO
ATTN: D EGELKROUT
ATTN: H WICKLEIN
ATTN: R SCHEPPE

BOEING MILITARY AIRPLANE CO
ATTN: C SUTTER

BOOZ ALLEN & HAMILTON, INC
ATTN: TECHNICAL LIBRARY

BOOZ ALLEN & HAMILTON, INC
ATTN: L ALBRIGHT

BOOZ ALLEN & HAMILTON, INC
ATTN: D DURGIN

CALSPAN CORP
ATTN: LIBRARY

COMPUTER SCIENCES CORP
ATTN: A SCHIFF

E SYSTEMS, INC
ATTN: MAIL STOP 3

E SYSTEMS, INC
ATTN: J MOORE

EG&G WASH ANALYTICAL SVCS CTR, INC
ATTN: A BONHAM
ATTN: J GILES

ELECTRO-MAGNETIC APPLICATIONS, INC
ATTN: D MEREWETHER

GENERAL ELECTRIC CO
ATTN: C HEWISON

GRUMMAN AEROSPACE CORP
ATTN: H SMITH TECH INFO CNTR

GTE GOVERNMENT SYSTEMS CORPORATION
ATTN: TECH LIBRARY

HARRIS CORP
ATTN: T W TOMBLER

HERCULES DEFENSE ELECTRONICS SYSTEMS, INC
ATTN: R LAZARCHIK

HERCULES, INC
ATTN: W WOODRUFF

HONEYWELL, INC
ATTN: LIBRARY

HONEYWELL, INC
ATTN: SR&C LIBRARY/T CLARKIN

IIT RESEARCH INSTITUTE
ATTN: I MINDEL

INSTITUTE FOR DEFENSE ANALYSES
ATTN: CLASSIFIED LIBRARY
ATTN: TECH INFO SERVICES

IRT CORP
ATTN: B WILLIAMS
ATTN: R W STEWART

ITT TELECOMMUNICATIONS CORP
ATTN: R SCHWALLIE

JAYCOR
ATTN: E WENAAS

JAYCOR
ATTN: LIBRARY

JOHNS HOPKINS UNIVERSITY
ATTN: P PARTRIDGE

KAMAN SCIENCES CORP
ATTN: K LEE

KAMAN SCIENCES CORP
ATTN: LIBRARY/B KINSLOW

KAMAN SCIENCES CORP
ATTN: E CONRAD

KAMAN SCIENCES CORPORATION
ATTN: TECHNICAL LIBRARY

KAMAN SCIENCES CORPORATION
ATTN: DASIAC

KAMAN TEMPO
ATTN: DASIAC
ATTN: R RUTHERFORD

LITTON SYSTEMS, INC
ATTN: E EUSTIS

DNA-TR-87-27 (DL CONTINUED)

LITTON SYSTEMS, INC
ATTN: J SKAGGS

LOCKHEED MISSILES & SPACE CO, INC
ATTN: J PEREZ

LOCKHEED MISSILES & SPACE CO, INC
ATTN: TECH INFO CTR D/COLL

LTV AEROSPACE & DEFENSE COMPANY
ATTN: LIBRARY

LUTECH, INC
ATTN: F TESCHE

MCDONNELL DOUGLAS CORP
ATTN: TECHNICAL LIBRARY

METATECH CORPORATION
ATTN: W RADASKY

MISSION RESEARCH CORP
ATTN: EMP GROUP

MISSION RESEARCH CORP
ATTN: J LUBELL
ATTN: J R CURRY

MISSION RESEARCH CORP, SAN DIEGO
2 CYS ATTN: J LAWRENCE
2 CYS ATTN: V VAN LINT

MITRE CORPORATION
ATTN: M FITZGERALD

PACIFIC-SIERRA RESEARCH CORP
ATTN: H BRODE, CHAIRMAN SAGE

PHOTOMETRICS, INC
ATTN: I L KOFSKY

PHYSICS INTERNATIONAL CO
ATTN: DOCUMENT CONTROL

R & D ASSOCIATES
ATTN: DOCUMENT CONTROL
ATTN: W KARZAS

R & D ASSOCIATES
ATTN: LIBRARY

R & D ASSOCIATES
ATTN: J P CASTILLO

RAYTHEON CO
ATTN: H FLESCHER

RCA CORPORATION
ATTN: G BRUCKER

RESEARCH TRIANGLE INSTITUTE
ATTN: M SIMONS

ROCKWELL INTERNATIONAL CORP
ATTN: B-1 DIV TIC (BAOB)

ROCKWELL INTERNATIONAL CORP
ATTN: G MORGAN

S-CUBED
ATTN: A WILSON

SCIENCE & ENGRG ASSOCIATES
ATTN: B GAGE
ATTN: B ZETLEN
ATTN: M BORDEN

SCIENCE & ENGRG ASSOCIATES, INC
ATTN: V JONES

SCIENCE APPLICATIONS INTL CORP
ATTN: W CHADSEY

SCIENCE APPLICATIONS, INC
ATTN: E O'DONNELL
ATTN: P J DOWLING

SINGER CO
ATTN: TECHNICAL INFORMATION CENTER

SPERRY CORP
ATTN: J INDA

SPERRY CORP
ATTN: TECHNICAL LIBRARY

SRI INTERNATIONAL
ATTN: D ARNS

TELEDYNE BROWN ENGINEERING
ATTN: F LEOPARD

TEXAS INSTRUMENTS, INC
ATTN: TECHNICAL LIBRARY

TRW INC
ATTN: LIBRARIAN

TRW INC
ATTN: A R CARLSON
ATTN: J PENAR

FOREIGN

FOA 121
ATTN: B SJOHOLM

FOA 389
ATTN: T KARLSSON

END
DATE
FILMED

4-88

DTIC